The generation of reactive species downstream of an atmospheric pressure plasma jet

Frederik Riedel

Doctor of Philosophy

University of York

Physics

November 2019

Abstract

Atmospheric pressure plasma jets have gained interest in the past decades, due to their efficiency in producing reactive oxygen and nitrogen species (RONS) at low gas temperatures. This makes them especially interesting for biomedical applications because some of the produced species play crucial roles for sudden and programmed cell death. Many plasma sources have been developed for this purpose. However, one of the challenges in the field is to compare the results from different laboratories and plasma sources. To bring the field of plasmas with biomedical applications forward, it would be beneficial to have a standard similar to the gaseous electronic conference (GEC) cell. Such a jet, called the 'COST Reference Microplasma Jet', was proposed as part of the 'Biomedical Applications of Atmospheric Pressure Plasmas' EU COST Action MP1101. However, the reproducibility of this jet, or any other jet has not yet been demonstrated. This was done in is this work by comparing four of these devices for plasma power, temperature of the effluent, ozone and atomic oxygen densities and bacteria inactivation. Having established the reproducibility, more measurements were undertaken for a helium/water/oxygen plasma to measure absolute densities of atomic oxygen, hydroxyl and hydrogen peroxide with laser induced fluorescence techniques, absorption spectroscopy and Fourier-transform infrared spectroscopy in the gas phase in the effluent. It was found that with oxygen admixture added to the water containing plasma, the hydrogen peroxide, ozone and atomic oxygen production can be tailored. Atomic oxygen densities were measured for different water admixtures and gas curtains on a plasma jet. This is more oriented for clinical application, such as through use with the kINPen. It was also found that the atomic oxygen production changes directly above a wet and a dry surface and, thus, possibly alters the amount of reactive species delivered to the same surface when using the kINPen.

Contents

List of Tables

List of Figures

Acknowledgments

I would like to thank my supervisors Deborah O'Connell and James Dedrick. More thanks going out to Olivier Guaitella and the LPP for allowing me to use their facilities. The same goes to Terry Dillon and WACL for allowing me to use their facilities. I would really like to thank Annette Chalker. She really helped me in the last breaths of my thesis. Furthermore, I would like to thank my parents for their love and support. I would not have made it without their help.

Declaration

I declare that this thesis is a presentation of original work and I am the sole author. This work has not previously been presented for an award at this, or any other, University. All sources are acknowledged as References.

In Chapter 3 biological experiments were conducted by Helen Davies. She also did the analysis and wrote the text for biological protocol, biological analysis, and biological conclusion. Everything else has been done by myself.

Chapter 1

Introduction

The motivation behind the project was to investigate plasmas with biomedical applications beyond the well understood water and oxygen chemistry in [1] in the COST jet and its variants (discussed further in section 2.1). For this, the question of reproducibility of results obtained across different COST jets arose which was tested first. The addition of oxygen to a water containing helium plasma produced results that led to the question how the reactive species production can be tailored. This was further investigated by using Fourier transformation infrared spectroscopy (FTIR), two photon absorption laser induced fluorescence (TALIF), photo dissociation laser induced fluorescence (PDLIF) and ultraviolet light absorption spectroscopy of the plasma and the effluent. TALIF measurements were also conducted on a more application driven plasma source that uses argon and water admixtures, the kINPen. To help place this study into context, a brief overview of atmospheric pressure plasmas and its applications, especially biomedical applications, and fundamentals of plasmas is given in the next sections.

1.1 Non-thermal Plasmas

Non-thermal plasmas are widely used in industry and research as a tool to modify surfaces and manufacture nano-scale structures at low pressures. These plasmas are mainly used to harden or etch surfaces for tool reinforcement, computer chip or solar panel manufacturing. But in the past decades non-thermal plasmas at atmospheric pressure have been investigated and opened new fields such as plasma medicine, decontamination, rudimentary surface modification, treatment of textiles, cleaning of daguerreotypes or food processing to prolong the shelf-life [2–16].

There are multiple reasons why non-thermal atmospheric plasmas are preferred in these fields. They do not need vacuum equipment, they are easier to handle than aggressive chemicals and produce less waste. Furthermore, plasmas can be scaled and setup to treat large areas cost effectively. They also can be tailored over a wide range that serves the applications.

The standout advantage of non-thermal atmospheric pressure plasmas for temperature sensitive materials is operation near room temperature and atmospheric pressure. This allows the treatment of thermal sensitive materials like biological tissue outside of vacuum equipment. They also allow efficient dissociation of molecular precursors by hot electrons [17] which can open chemical reaction pathways that are not accessible by conventional chemistry [11].

The most common atmospheric plasma reactor types are atmospheric pressure non-thermal micro plasmas (µAPPJs) which are scaled, at least in one dimension, from 10 µm to 1000 µm. They are often flow through reactors. Concrete examples for the use of µAPPJs can be found in [2, 18–23] for biomedical applications, decontamination [4, 6–8, 24], surface modification [12, 25] or material synthesis [10, 11]. Furthermore, they are used in CO/CO2 conversion [26, 27], and coating of surfaces [12]. Especially biomedical applications benefit from the highly localised delivery of reactive species.

The reason for them to have small electrode gaps is the Paschen's law. This law describes the breakdown voltage as a function of pressure times electrode distance. This function has a minimum at a specific pressure times voltage point which is specific for different gases. The pressure is fixed to one atmosphere. Thus, to achieve a low breakdown voltage, the distance between electrodes has to be short. This explains why the electrode gap of atmospheric plasmas is in the range of millimetres.

With the dimensions dictate by physics comes a high surface to volume ratio which has an effect on gas temperature. According to Mariotti et al. [11] one can derive a simple proportionality for the dimensions of a plasma and cooling by walls and other factors:

$$\frac{P_{cool}}{V} \propto n_g \frac{T_g^{3/2}}{pD^2} \tag{1.1}$$

with P_{cool} the cooling power, V the volume, n_g the gas density, T_g the gas temperature, D the size of the plasma and p the pressure. In micro plasmas the cooling effect through walls due to the surface to volume ratio is usually high. This resolves in a lower gas temperature that is beneficial for applications previously mentioned.

There are various ways to generate a plasma at atmospheric pressure. All of them are based on a configuration with two electrodes [28]. Various discharge configurations were proposed such as planar and coaxial micro plasma jets, micro hollow cathode arrangements or dielectric barrier configurations. These configurations can be operated with direct current (DC) or alternating current (AC) and are often designed as flow through reactors.

However, they all have advantages and disadvantages. And no standard design many researchers agreed on to do fundamental research like with the GEC cell has been established.

As said before, many plasma jet variations exist, however, all do have advantages and disadvantages. In the following, the major discharge variations are discussed.

DC plasmas are realised in their simplest form with two bare metal electrodes between which the plasma is formed due to sufficient enough voltage (see Pachen's law) and direct current.

A downside of these plasmas is, that they heat up the gas well above room temperature. This can be solved by pulsing the plasma.

Pulsed plasma jets achieve higher power densities during the pulse and are pulsed in the kHz or MHz regime [29]. Different electrode geometries exist which are: two bare metal electrodes, semi dielectric and dielectric electrodes. These plasmas are often generated by voltages in the kV regime. An example for a dielectric plasma jet consisting of two ring electrodes around a glass tube can be found in [5, 30] and a semi dielectric configuration consisting of a metal pin in the middle of a tube and a grounded ring electrode around the tube or a grounded mesh or plane can be found here [31]. These plasmas are very susceptible to geometric changes [32] as well as changes of capacitance close to the plasma jet which can change the contact time of reactive species with the target dramatically [33]. The plasma is also very often in direct contact with the target surface thus the generation of reactive species highly depends on the surface [34]. Even the polarity of the electrodes can alter the flow of the effluent [35].

Radio frequency plasmas can be built in a way that they are not as susceptible to the surroundings as DC pulsed plasmas.

A common discharge geometry for atmospheric RF plasmas are two bare metal electrodes with glass on the sides to restrict the flow. This concept has been developed into the 'COST Reference Microplasma Jet' (referred as COST jet further on) and was proposed in Judith et al. [36]. The jet is driven by continuous radio frequency (13.56 MHz) and helium with small molecular gas admixtures. With this design, it is easy to access the plasma via spectroscopic and laser methods [37–41] and model the plasma [42–44]. A standard reference jet, that delivers reproducible results would be beneficial for the field and accelerate research forward much like the GEC cell did. However, it has to be tested how reproducible results from different COST jets are.

1.2 Plasmas for biomedical applications

The emphasis of this study will focus on plasmas with biomedical applications. The reasons regarding the beneficial use of APPs for biomedical applications will be briefly described in this section.

Atmospheric pressure plasmas are a source of reactive species, such as atomic oxygen, hydroxyl, hydrogen peroxide and nitric oxide, also known as reactive oxygen nitrogen species (RONS), which render plasma jets an important tool in medicine [45–47]. RONS are already used in radiotherapy by producing them in the body with ionising radiation. Thus, it would be interesting to have sources of highly reactive species without ionising radiation. These species are produced in the plasma through processes such as electron dissociation and recombination. After the plasma, chemical reactions, such as recombination, dominate the

generation and destruction of reactive species.

RONS generated by the plasma can diffuse into water and/or react with water or solved chemicals to generate other reactive species [48]. For example, tt was previously observed that atomic oxygen from the gas phase reacts with chloride ions in a water and salt solution [49], creating bleach-like reactants.

In several studies, plasma was directly applied to biological material. For example, on skin tissue and bacteria in numerous media such as agar or water [2, 30]. These studies found, for the most part, a positive effect for cancer treatment and bacterial inactivation. This might be a solution for one of the major threats in modern medicine: antibiotic resistant bacteria [50–52]. However, previous studies have observed that bacteria resistance against antibiotics can be inactivated by APPJs [3, 53].

But to date, the temperature of the samples during the plasma treatment was of a lesser priority and the argument of evaporative cooling was held against simple temperature measurements. However, to study the effects of the plasma decoupled from temperature effects, the sample temperature has to be kept below 37 °C in order not to destroy the samples [54]. Temperature for agar surfaces have been recorded as can be seen in the appendix in Figure A.2, that show this argument has to be revised for longer treatments or curtain high power conditions. In addition, it was investigated to what degree the observed biological effects were caused by either UV radiation or reactive particles. [19, 55] found reactive species to cause a stronger effect on *Escherichia coli* than UV radiation. However, the most effective treatment in these studies turned out to be a combined treatment of reactive species and UV photons as they derive from the plasma jet naturally.

The above mentioned effects make atmospheric pressure plasmas a potent tool in medicine. However, many biological effects of reactive species from plasmas are not well understood and precaution has to be taken. Moreover, it would be important to tailor the reactive species in a way that is favourable for biomedical applications.

As this work will be focusing on the COST jet, some important results will be discussed in the following.

Previous studies on the COST jet, and its predecessors, showed that the plasma effluent can extend up to 5 cm after the nozzle [56] without being disturbed by buoyancy or thermal air movement (slow air movement) at 1 slm helium as feed gas. [57] reported that the atomic oxygen production is most efficient with an admixture of 0.5 % to 0.6 % molecular oxygen. [58] reported an atomic oxygen density of $8 \times 10^{20}\, m^{-3}$ and an ozone density of $2 \times 10^{20}\, m^{-3}$, depending on operation conditions. Measurable quantities of atomic oxygen extend up to 30 mm from the nozzle. Using water admixtures, added to the discharge, hydroxyl and hydrogen peroxide can be produced. While the OH density reported by [1] is around $5 \times 10^{20}\, m^{-3}$ inside the plasma it declines to $2 \times 10^{20}\, m^{-3}$ and is lower outside the plasma but is still measurable by CRDS and MBMS in up to 20 mm distance to the active plasma in

a helium atmosphere [59]. All of the above mentioned studies show that the RONS output can be influenced by plasma power and admixture of molecular gases. Other studies that investigate pulsing the plasma [60] or applying higher frequencies [61] exist but these studies do not explore the mixing of several gases. It would be interesting to have more than one molecular gas admixed and explore the possibility to influence the plasma chemistry this way.

The studies above used the predecessors of the COST jet, meaning the same electrode geometry. At present, it is not clear in what degree these results can be compared regarding the reproducibility of the plasma jet and most of these studies were conducted under helium atmosphere. This means that it is unclear how comparable these measurements are when the plasmas are applied under normal atmosphere.

Biomedical applications especially need small deviations in gas temperature of the sources as an effluent temperature higher than 37 °C can destroy biological material [54]. This needs to be evaluated for the COST jet, too.

Another atmospheric plasma jet for biomedical applications is the kINPen, which was developed in Greifswald and is commercially available and medically licensed in Germany. It is operated with argon and small admixtures of molecular gases. An extensive overview regarding the kINPen can be found in [31]. Furthermore, some measurements on this device were conducted in this work that have not been conducted before. These include the plasma interaction with wet and dry targets and the resulting atomic oxygen densities. Furthermore, the effect of different gases in the so-called gas curtains that shield the plasma from surrounding uncontrolled air on the atomic oxygen production will be discussed.

1.3 Methodology

The emphasis in this work lies on plasmas with biomedical applications. For this, plasmas have to be characterized to high standards in order to obtain meaningful data from biological experiments or treating patients.

Atmospheric pressure plasmas pose challenges to the techniques used to detect reactive species. Such challenges include high quenching rates and short absorption lengths under atmospheric conditions.

To understand how the chemistry in atmospheric plasmas and their effluent works, various optical and non optical diagnostics can be used.

In this study, the emphasis is mainly on optical diagnostic methods. But other methods such as mass spectrometry have been used in the past and developed further [62, 63]. Mass spectrometry is a challenging method because the pressure difference from atmospheric pressure to nearly vacuum has to be overcome.

Therefore, the most common diagnostics are optical diagnostics such as optical emission

spectroscopy, absorption spectroscopy and laser induced fluorescence. This also indicates the amount of review papers on optical diagnostics [64, 65].

However, electrical diagnostics such as power measurements are also used to determine the power that is absorbed by the plasma to link it to other parameters obtained from optical measurements or as input parameter for simulations. Electrical diagnostics, such as the Langmuir probe, are not well suited for atmospheric micro plasmas because they disturb the plasma too much.

With the advent of powerful computers, simulations became more prevalent in this field, too. These can be global models that have extensive chemistry reaction sets but do not offer spatial resolution. Others offer spatial resolution and try to model the effluent reacting with water or other media.

In the past, numerous spectroscopic methods have been used to detect and quantify reactive species in the plasma and it's effluent, for example, optical emission spectroscopy [66], Fourier transformation infrared spectroscopy [67, 68], laser induced fluorescence for atomic and radical species [69], diode laser absorption spectroscopy for metastable states of helium [70, 71] and mass spectroscopy, for neutral and ionic species [58, 72, 73]. However, these studies have been conducted on a variety of different jets [28] which makes it difficult to compare the results and synthesis knowledge from different publications. One point that the COST jet tries to overcome.

Absorption Absorption spectroscopy is an active optical technique that allows line of sight measurements. It is possible to detect several species in absorption at once, but their cross sections might overlap and the signal has to be de-convoluted. It was used in the past with broadband UV LEDs and tunable lasers to detect ozone, hydroxyl or nitric oxide and metastables. In APPJs it was used to measure helium metastable [71], hydroxyl [1, 59], ozone [37] or nitric oxide [74]. It is suitable for atmospheric pressure because it is not affected by quenching and only relies on the resonant transition of the atom or molecule. However, the ease of use comes with the limitation that the densities have to be high enough, as well as, the absorption path long enough. If the absorption path is not long enough, it can be improved by using cavity ringdown spectroscopy as was done in [59]. Another limitation in the atmosphere are the wavelengths that can be used. For atomic species the wavelength lie in the vacuum UV. This means that the APPJ has to be kept in vacuum as well as the light source. This was done in Dedrick et al. [60].

FTIR An expansion of the absorption method in the infrared region is Fourier transform infrared spectroscopy. It has been used to detect hydrogen peroxide [67] on the kINPen effluent. This study also shows that a long path absorption cell is needed to detect the small quantities of reactive and infrared active species. Therefore, it is challenging to directly measure in the plasma or its effluent. Other species that can be detected by FTIR include

nitric oxide, ozone or carbon monoxide as well as others.

LIF/TALIF A common technique to measure reactive species densities in the effluent or in the plasma is laser induced fluorescence (LIF). This technique works by exciting an atom or molecule into a higher state and recording the fluorescence signal from this excited state. This method can offer a good resolution depending on the beam size and recording equipment. The main disadvantage is the temporal resolution that is needed at high pressures because the de excitation is highly affected to quenching. The accuracy of this measurement also relies on the accuracy of the LIF cross sections from the literature. In the past, mainly hydroxyl and nitric oxide have been measured by LIF in plasma effluents on various jets [34,69,75–83].

Another similar technique is two photon absorption LIF (TALIF). In this, the atoms, or molecules, absorb two photons instead of one. This has the advantage that fluorescence signal is quadratic proportional to the laser energy, it uses non resonant states and it removes the need to use vacuum ultraviolet lasers. The latter advantage is very important for measurements in the atmosphere. TALIF is well known [84–91] and has been widely used by different fields, such as in combustion chemistry. TALIF schemes for many species have been developed [39, 92–99]. However, in the field of atmospheric pressure plasmas mostly atomic oxygen and atomic hydrogen have been measured. One of the first TALIF measurements of atomic oxygen on an μAPPJ operated with helium was published by [93].

The greatest challenge, as stated above, is the temporal resolution. At atmospheric pressure, the quenching rates are very high. To address this, short laser pulses in the pico- or femtosecond are necessary. Otherwise the quenching rates have to be calculated. This is only accurate if the gas mixture is well known. Another challenge is the calibration of the signal. For TALIF, noble gases can be used to callibrate the signals for atomic species. However, calibration for hydrogen LIF poses a problem because a source with a known hydroxyl concentration is necessary.

Some species, such as hydrogen peroxide, cannot be detected directly. However, it can be dissociated by a laser first and the hydroxyl molecules can be detected subsequently. This technique has been previously utilised in combustion chemistry [100, 101], but has not been used with APPJs. Thus, it is not well understood how hydrogen peroxide behaves in the effluent of a plasma in gas phase.

1.4 Scope

In the previous sections, several challenges for plasmas with biomedical applications and possibly beyond can be identified. A plethora of measurement methods exists that can be chosen to measure important species and determine physical and chemicals pathways that alter the plasma. In this study, the proposed solutions are as following:

1. It has not yet been established how reproducible the results of the COST jet are. For this, four devices of the COST jet, which was introduced as a reference jet, will be compared. The aim is to determine the reproducibility and variance across a set of parameters. The parameters are delivered electrical plasma power, gas temperatures of the effluent, optical emission spectra of the core plasma, absolute ozone densities and atomic oxygen densities. Additionally, the inactivation of bacteria was tested.

2. Techniques that are novel to use with atmospheric plasmas, or were improved, are used to determine absolute species densities that have not been measured in the gas phase on the COST jet before. Absolute hydrogen peroxide densities are quantified using Fourier transform infrared spectroscopy and photo dissociation laser induced fluorescence. Absolute hydroxyl densities were measured by absorption spectroscopy and laser induced fluorescence. The hydroxyl laser induced fluorescence setup was calibrated against *tert*-butyl hydroperoxide. This type of calibration has not been done before. Absolute atomic oxygen densities were determined by two photon absorption laser induced florescence using a pico second laser system to eliminate the need to calculate the quenching rate and make reliable measurements in air.

3. How can the plasma chemistry be altered to tailor the production of ,for example , hydrogen peroxide or ozone without using multiple frequencies or pulsing the plasma with high power? For this, oxygen will be mixed to the water containing plasma and the effect will be systematically investigated by optical measurement techniques. This has not been done before on the COST jet and its predecessors.

4. Finally, atomic oxygen will be measured on the kINPen for a water variation with different gas curtains. Additionally, the atomic oxygen production directly above a dry and a wet surface with water containing plasma was measured. This task imposed many challenges and has not been done before and will be discussed later.

Chapter 2

Plasma diagnostics and sources

In this chapter, the plasma sources used in this work are described with one exemption: the kINPen. This plasma source is more clinically oriented and only used in chapter 5. Therefore it will be described within that chapter.

After this, the diagnostics used in this work are explained starting with non optical diagnostics: power measurements and temperature measurements followed by optical diagnostics: absorption and optical emission spectroscopy, FTIR and LIF techniques.

2.1 Plasma sources

For the purpose of this work, two plasma sources were used that allow to study the plasma with different measuring methods. One source was the COST micro reference jet and the other a modified sealed version of the COST jet with a wider plasma channel. In the following the two plasma sources will be explained in more detail.

2.1.1 COST jet

The COST jet is a product of the collaboration COST MP1011 on 'Biomedical Applications of Atmospheric Pressure Plasma Technology' [102] and was proposed in its final form in [36]. Previous versions included the same electrode geometry and have been extensively used to investigate the plasma and effluent to understand the physics and chemistry. The jet consists of a 30 mm x 1 mm x 1 mm (length x wide x height) plasma channel and incorporates voltage and current probes in a housing to determine the power dissipated by the plasma.

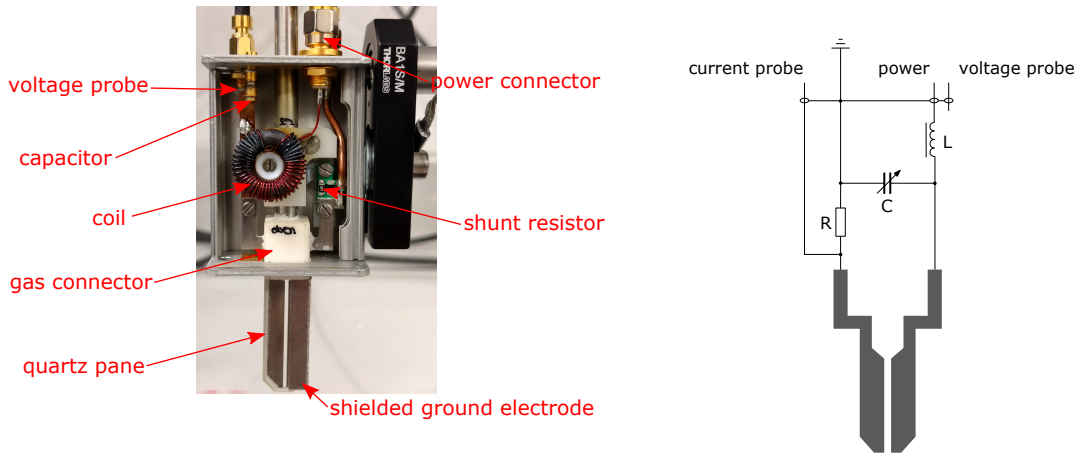

a) b)

Figure 2.1: a) Complete COST jet with open housing showing the electrode assembly, voltage and current probes, power and probe connectors and the gas tubing. b) Schematic of the electrode assembly showing the two stainless steel electrodes and the quartz panes covering them. The electrodes and the gas tubing are sealed by TorrSeal®.

Figure 2.1 depicts a photo of the open jet and the electrode assembly. One of the electrodes is powered with 13.56 MHz alternating current and the voltage is measured with a capacitively coupled voltage probe. The other electrode is grounded and the current is measured with a shunt resistor. To prevent any stray electric fields altering the current measurements, the grounded electrode is additionally shielded with an aluminium shield around the ground electrode.

The plasma channel is confined by 1.5 mm quartz glass (Corning 7980) on both sides of the electrodes and sealed with TorrSeal®. At the end of the electrodes, the quartz glass extends 1 mm to form a safety zone preventing to touch any of the electrodes with bare fingers. The gas is supplied through a stainless steel tube into the ceramic gas connector to feed the electrodes. The ceramic also serves the purpose of insulating the electrodes and gas supply electrically. Additionally, the aluminium housing, as seen in figure 2.1a, includes a resonance coupling network to match the plasma and power supply impedances. This coupler is based on Marinov and Braithwaite [103] and, within limits, eliminates the need for an external matching box. At the bottom of the housing is a M5 thread to install the device on optical posts. In operation, the housing is closed to prevent radio frequency radiation from leaking in or out of the housing. For optical emission spectroscopy, a cover for the electrodes and a spacer for optical fibres are available to keep metallic fibre connectors 3 mm away from the electrodes in order to not disturb the plasma.

The power for the plasma jet is provided by a power supply (Coaxial power RFG50-13) which is attached to the jet via a matchbox with a coaxial cable (1 m, 50 Ω) and an adaptor from BNC to SMC. Using the official COST jet power supply or other power supplies with at least 5 W power output does not yield in different power characteristics.

For the gas supply, short Perfluoroalkoxy alkanes (Swagelok PFA-T4-047-100) tubes are used. These provide flexibility to mount the jet on an x-y-z stages. The jet is connected with a Swagelok to O-ring fitting connector (SS-4-UT-6-400) to the gas tube on the jet. A valve was placed before the plasma jet in order to prevent moisture from diffusing into the gas tube while the jet is not in use.

2.1.2 Modified COST jet

For some diagnostics, such as UV absorption spectroscopy or FTIR, the plasma jet channel must be wider in order to achieve a sufficient absorption length or the amount of species produced has to be higher to be detectable. Furthermore, the ability to connect the plasma jet directly to a multipath absorption cell makes it easier to study the plasma chemistry without introducing ambient air into the plasma effluent and, thus other uncontrolled impurities.

For this, another jet is used, called the modified COST jet. The modified COST jet has a plasma channel eleven times wider than the COST jet, but otherwise, the same dimensions. The plasma channel dimensions are 30 mm x 11 mm x 1 mm (length x wide x height). This leads to a plasma volume to surface ratio of 0.45 instead of 0.25 as in the case of the COST jet. This can make a difference for highly diffusive species, such as hydrogen, or species that react heavily with the wall materials [104].

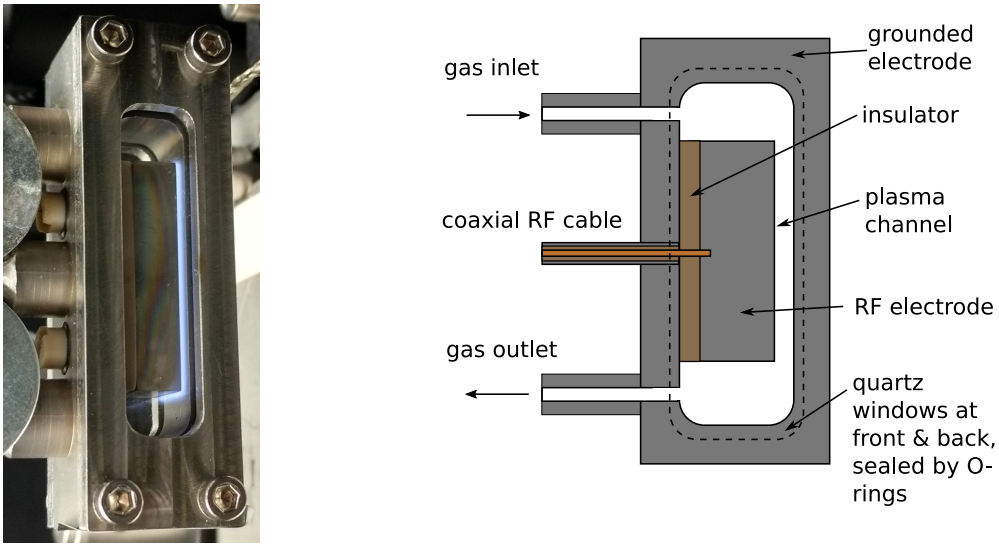

a) b)

Figure 2.2: a) Photo of the modified COST jet. The blue light is the plasma. b) Schematic of the modified COST jet with the grounded stainless steel housing, powered electrode and power feed through as well as the gas supply. More information on this source can be found in Niemi et al. [105]

Figure 2.2 shows the schematic of the jet and a photo with the plasma switched on. The housing of the jet is grounded and acts as the grounded electrode. The powered electrode is insulated by a plastic piece with a feed through for the power connector. The sides of the plasma channel are covered with quartz glass and are sealed with O-rings.

One limitation is, that it is not possible to run the COST jet and the modified jet at the same power density for many gas admixtures but helium only. The plasma ignition voltage of the COST jet becomes higher with increasing water admixture than the arcing voltage of the modified COST jet. This leads to non overlapping power densities with increasing water admixtures. This might be a cause of the different volume to surface ratios of the jets. This makes it difficult, but not impossible, to compare results from the COST jet.

Other than the COST jet, it has no built-in voltage or current probe and thus requires external probes to measure the power dissipated by the plasma. For this, an external probe (Solyel) is used which will be explained later in 2.2.

2.2 Power Measurements

The power that is dissipated into the plasma determines the electron density and electron temperature. Thus, the power has great influence on the plasma chemistry. Several concepts to measure the plasma power in µ-AAPJs exist [36, 106, 107]. Measuring the plasma power accurately is important for comparing different plasma sources and as an input factor for

global kinetics simulations. Despite its important role in plasma physics and chemistry, the power, or power density, is often not reported in publications [28]. This is due to small powers at high frequencies are difficult to measure because of small error margins in the phase measurements. In order to characterise atmospheric pressure plasma jets, such as the COST jet correctly, the power has to be measured accurately.

In the following, the fundamentals and challenges of measuring power on the devices used in this work will be explained further.

Theory In electrical circuits, the power (P) is measured by multiplying the voltage V and the current I. In the case of alternating current (AC), one usually takes the integral over one period T of the signal:

$$P = \frac{1}{T}\int_0^T V(t)I(t)dt \tag{2.1}$$

In this work, only sinusoidal voltages and currents are used. Hence, $V(t)$ and $I(t)$ can be written as $V(t) = V\cos(\omega t)$ and $I(t) = I\cos(\omega t + \theta)$ with θ the phase shift between voltage and current and $\omega = 2\pi f$ with f as frequency. Figure 2.3 shows the relations of voltage and current traces in graphical form. Substituting these into equation 2.1, the equation becomes:

$$P = \frac{VI}{2T}\int_0^T \cos(2\omega t + \theta) + \cos(\theta)dt. \tag{2.2}$$

As the integral is over one period $T = {}^{2\pi}/_{\omega}$ the integral 2.2 becomes:

$$\overline{P} = \frac{VI}{2}\cos(\theta) \tag{2.3}$$

with $\overline{P}$ as root mean square (RMS) value of the power.

In order for $P = 0$, θ has to be ${}^{\pi}/_{2}$. This is an important relation because it can be used to calibrate the instrumental factor θ_{ref} introduced by cables, connectors and the oscilloscope itself. In the case of the COST jet, it can be reasonably assumed that electrodes act as a perfect capacitor because of their simple geometry and that similar electrical permittivity. This makes equation 2.3 looks like this:

$$\overline{P_{plasma}} = \frac{VI}{2}\cos(\theta - \theta_{ref}). \tag{2.4}$$

In this work, voltage and current values are presented as root mean square values (RMS). RMS is the effective direct current equivalent of electrical power dissipated in a resistive load [108].

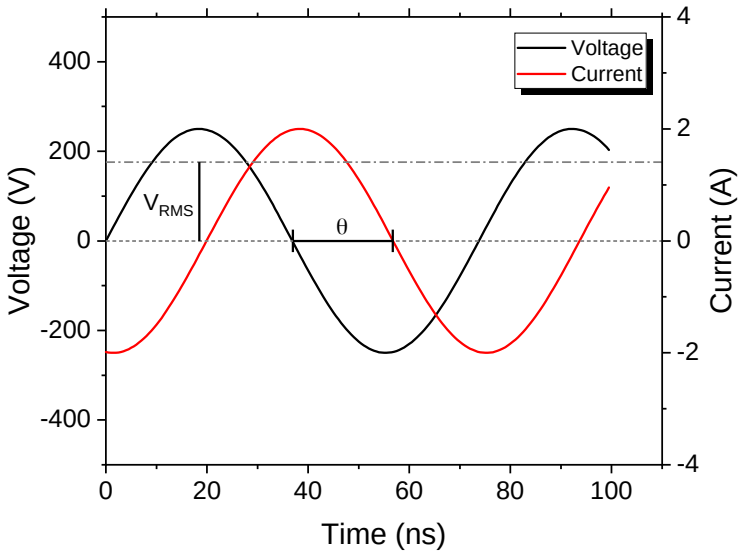

Figure 2.3: Voltage and current traces versus time to show the phase difference and root mean square value.

2.2.0.1 Measuring power

The jets used have been discussed in section 2.1. The COST jet uses probes placed close to the plasma to avoid any influences of ohmic heating in cables, capacitively losses due to bend cables or influences of different power cable connectors. Therefore it was not necessary to correct the power with I^2R measurements as was done in [109, 110] Figure 2.5 depicts the setup to measure the power on the COST jet and the modified COST jet. As discussed in 2.1 with the equivalent circuit from figure 2.1, the voltage probe is a capacitively coupled probe. It consists of a metal pin parallel to the powered supply rail in the jets' housing. This has the advantage that no high voltages, which can easily reach 700 V_{PP} and higher, are accessible to users outside the plasma jet. Furthermore, the voltage probe does not influence the electrical circuit as much as other conventional voltage probes, such as clamp on high voltage probes, can do. But without direct connection to the plasma, the voltage probe has to be calibrated against a conventional voltage probe. This was addressed by clamping on a voltage probe through a special designed housing cover (see figure 2.4) to the driven electrode, minimising external influences.

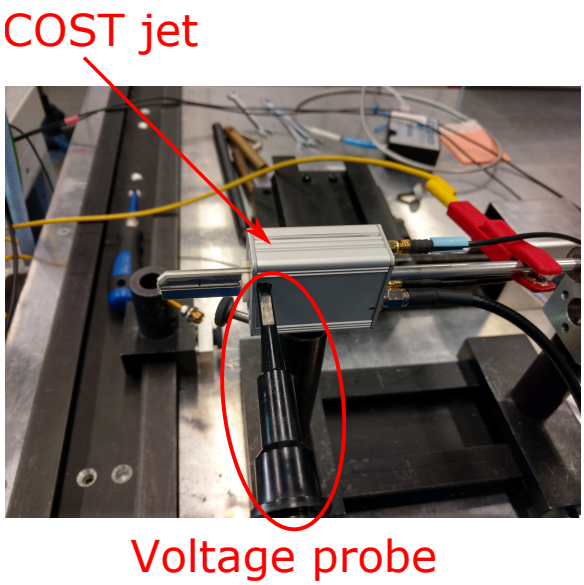

Figure 2.4: Voltage calibration of the COST jet. One side of the cover was replaced by a cover with a hole to allow the voltage probe to connect to the powered electrode and minimise electrical influences.

The current was measured with a 4 Ω shunt resistor and the voltage measured across it is directly related to the current by (equivalent circuit as seen in 2.1 b)):

$$I = U_\mathrm{s} \frac{R_\mathrm{s} + R_\mathrm{t}}{R_\mathrm{s} R_\mathrm{t}} \tag{2.5}$$

with I the current, U_s the voltage measured, R_s the shunt resistance and R_t termination resistance on the oscilloscope.

In order to measure the power correctly, the instrumental phase shift has to be determined. This was done by measuring the phase shift with no gas flow in order to prevent plasma formation. This was done because the probes are very close to the electrodes, which act as a capacitor with very low equivalent series resistance or inductance.

The current and voltage probes from the COST jet were connected via Thorlabs CA2612 cables and 50 Ω resistors to the oscilloscope (Agilent Technologies Infinivision DSO-X 2004A (2 GSps 70 MHz)) which recorded the voltage and current traces and sent them via USB to a computer where they were analysed.

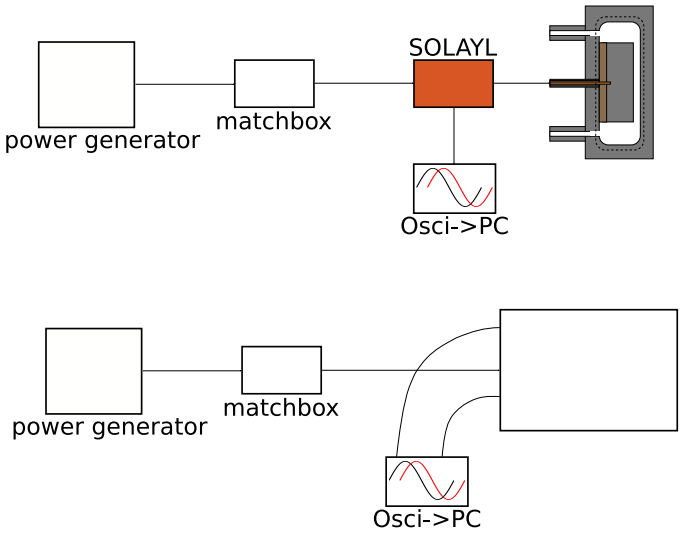

Figure 2.5: Voltage and current measurements on COST jet and modified COST jet.

In the case of the modified COST jet, the power was measured with a commercial probe (Solayl), as depicted in figure 2.5. This device includes voltage and current probes which were already calibrated by the manufacturer. The only element requiring calibration was the instrumental phase shift. After comparing the phase shift from a capacitor to the phase shift of the jet without plasma ,similar to the COST jet, it was concluded that the reference phase shift could be measured in the same way as the aforementioned COST jet. Because the cable length from the probes to the jet was approximately 1 m long, the ohmic heating of the cable had to be taken into account.

The voltage and current traces were sent from the oscilloscope to a computer with a python script that calculated the plasma power in real time by fitting a sinus to the oscilloscope traces from voltage and current probe. The software is available from GitHub [111].

2.3 Temperature

The gas temperature is a crucial parameter for biomedical applications and heat sensitive surfaces. It is largely controlled by the electrical power applied to the plasma due to ohmic heating.

Various methods to measure the temperature of gases, plasmas and surfaces exist. The methods used in this work are thermocouple, thermographic camera and vibrational-rotational spectroscopy. In the following, these three methods and experimental setups will be presented.

Thermocouple

Thermocouples utilise the Seebeck effect to measure the temperature. Two wires of different metals are joined together on one end and connected to a voltmeter on the other. A temperature difference on one side of the metals creates a thermoelectric current. This results in a voltage which can be measured with the voltmeter. The voltages are usually in the micro volt range and thus special measurement equipment, such as thermocouple amplifier, has to be used.

Thermocouples are a tool for measuring temperatures of fluids or rigid objects. In this case, it was used to measure the temperature of the COST jet effluent.

For this, a K-type thermocouple was placed 3 mm in front of the electrodes, which was connected to an analogue to digital USB converter (TI USB-TC01). K-type thermocouples are well suited to work in oxidizing atmospheres such as the plasma effluent. 3 mm was the closest distance conductive materials can be placed close to the plasma jet electrodes without disturbing the plasma. The distance was determined with plasma on by reducing the distance between the thermocouple and electrodes until the plasma power started to change.

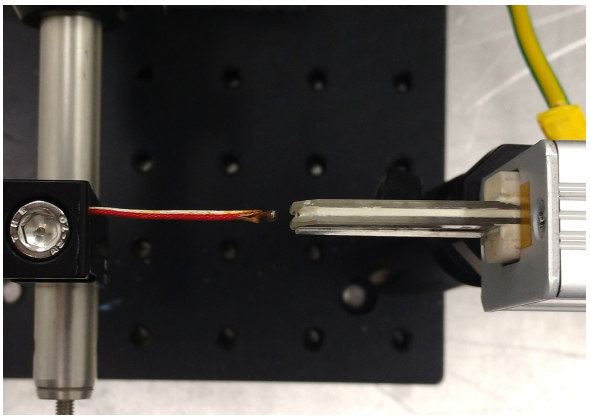

Figure 2.6: Setup to measure the temperature of the plasma effluent with a K-type thermocouple. The closest distance without disturbing the electric fields of the electrodes was 3 mm (shown in this picture).

Figure 2.6 displays the setup used to measure the effluent temperature with a thermocouple. The jet was placed horizontally on an optical post. The thermocouple was placed on a linear actuator in front of the jet and can be adjusted to find the maximum temperature in front of the jet at 3 mm distance in the middle of the effluent.

In order to rule out influences from the radio frequency (RF) jet on the measured temperature, a test with RF on and off was conducted. This showed no influence from the RF.

Surface temperature

Measuring surface temperatures is critical in order to assess the feasibility of atmospheric microplasmas for thermal sensitive samples, such as certain plastics or growth media. Moreover, flow profiles can be observed and, as in this work, compared to check different builds of the COST jets.

For this task, a thermographic camera was used. The sensor consists of a matrix of heat detectors that can sense far infrared radiation in the wavelength range of 7 µm to 14 µm.

In order to determine if the flow profiles of the plasma jets are the same and to check the temperature in a simulated use case scenario, a substrate (microscope slide) was placed at various distances in front of the plasma jet. Figure 2.7 displays the setup to measure the surface temperature with a thermographic camera. It consisted of the thermographic camera (Agilent U5855A), the jet mount, a microscope slide with a frosted surface and the COST jet. The microscope slide glass surface was sanded to reduce reflections of other heat sources. The thermal emission coefficient ε of the matte glass surface was measured using an infrared sticker with a known emission coefficient of $\varepsilon = 0.95$. The emission coefficient was found by comparing the temperatures of the glass and sticker. This was important because different materials and surface properties have different emission coefficients. The microscope slide was not lying directly on the optical breadboard, but was elevated about 3 mm with two 2 mm broad black silicon rubber pieces.

The thermographic camera was pointed at an angle of approximately 28 °onto the glass surface and was placed approximately 20 cm from the surface. This was the minimum focal point for this camera and resulted in a resolution of 0.27 mm/pixel. The jet was mounted vertically on a linear actuator, which can move the jet from 0 mm to 30 mm measured from the surface. The minimum distance from the cost jet to the surface in order to record thermographic images to measure the flow profile was 4 mm. The setup was surrounded by black metal sheets. This ensures that the surroundings radiate heat homogeneously and any faint reflections from the setup are homogeneous.

The images are exported with the "TrueIR Analysis and Reporting Tool v 2.0" software from Agilent. The exported data was then processed by a Matlab script [112] to extract the surface heat profiles.

Rotational and vibrational spectra of diatomic molecules

Rovibrational spectra can be used to measure the gas temperature. Most often diatomic molecules are being used for this purpose. Diatomic molecules have the advantage that it was relatively easy to calculate their spectra because only two atoms are involved. Typically nitrogen or hydroxyl are used for this task. In principle, every diatomic molecule can be used.

For the purpose of this work, hydroxyl was used to measure the gas temperature in the

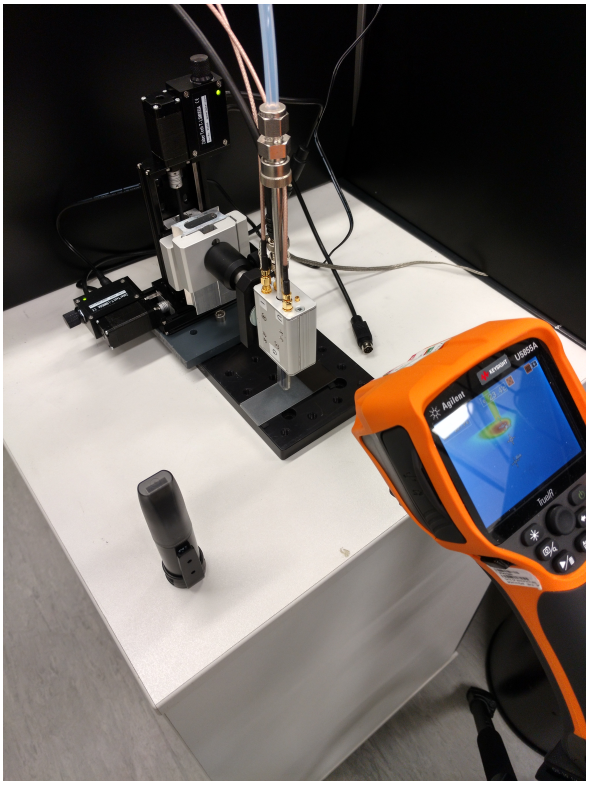

Figure 2.7: Setup to measure surface temperature with a thermal camera. The jet was pointed at a sandblasted microscope slide. The slide was not lying directly on the optical breadboard but was elevated about 3 mm with two 2 mm broad black silicon rubber pieces.

plasma by means of absorption spectroscopy. For this, it can be reasonably assumed [113] that the rotational temperature was equal to the gas temperature because at atmospheric pressure the collision rate with other atoms and molecules is high enough to equilibrate the energy between all the molecular levels. With these assumptions, this is a good measurement of the gas temperature.

2.4 Absorption spectroscopy

Absorption spectroscopy is an active, non intrusive technique to determine the density of a certain species in the plasma or effluent. For this, a light source with emission in the range of the absorption of the species is shone through the plasma or the effluent. To determine the density, only the absorption cross section of the species and the absorption length must be known. This is described by the Beer-Lamberts law:

$$I(x) = I_0 exp(-\sigma N L) \tag{2.6}$$

With I the intensity with medium, x the absorption length, I_0 the intensity without medium, σ absorption cross section and N density of the species. Equation (2.6) dictates that a

background measurement, with a light source only, and a measurement with a medium have to be taken.

Because of its simplicity for certain species, it is a commonly used technique to determine ozone, nitro-oxide species or hydroxyl densities [1, 37, 114]

Figure 2.8 shows a collection of cross-sections in the UV regime of species that were presumably produced in the plasma in this work. The blue species are O_xH_y, the red are O_x and the black are O_xN_y. It can be observed that most of the cross sections are overlapping. This makes independent measurements difficult in plasmas with numerous types of admixture. Otherwise, the absorption spectra have to be de convoluted. Therefore, plasmas with only oxygen, nitrogen or water admixtures are preferred in the literature. If only non spectrally resolved measurements are taken, it is impossible to determine the species concentration due to overlapping absorption cross sections.

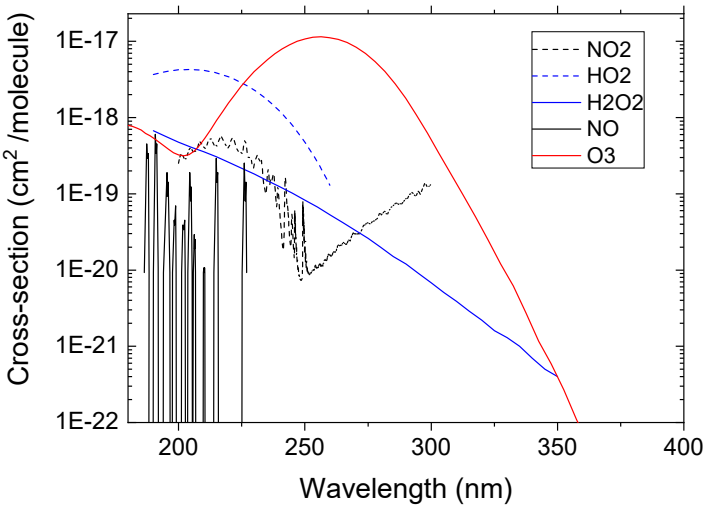

Figure 2.8: Compilation of cross-sections of species produced in the plasma. Sources: [115–118]

Hydroxyl absorption

For the density and temperature measurements the OH($X^2\Pi_J$, v' = 0) - OH($A^2\Sigma_J$, v" = 0) transition was used in this work. The transition lines can be found at 308 nm ± 2 nm. OH excitation in low temperature atmospheric pressure plasmas usually occurs due to electron impact excitation into the higher levels. This is counteracted by high quenching rates so we can assume that hydroxyl is in the ground state [119].

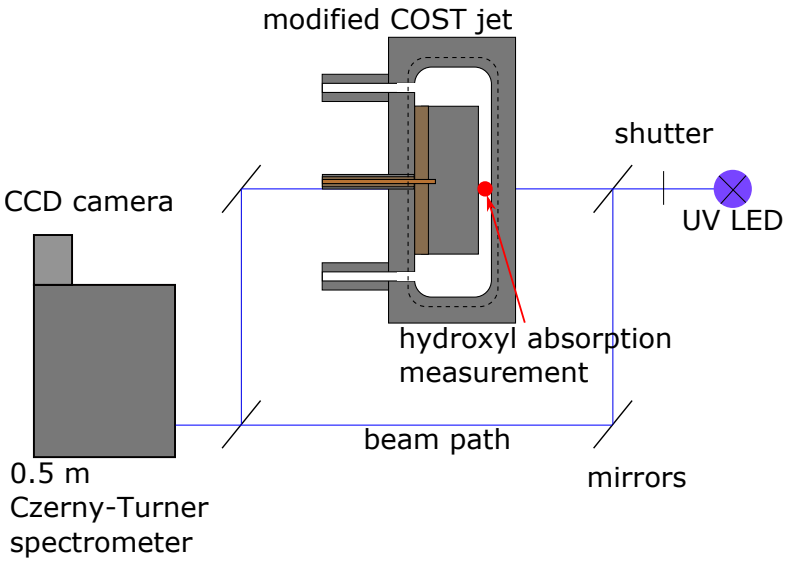

Figure 2.9: The optical absorption setup was realised as a Mach-Zender configuration. But instead, to interfere the two beams they were monitored separately for enhance the SNR.

The hydroxyl absorption setup was realised with a Mach-Zender setup (Figure 2.9). The same setup was used by Wijaikhum et. al. and Schroeter et. al. [1,37]. In the present work, the setup was utilised, the plasma jet was installed and small adjustments to optimise the signal-to-noise ratio were made. The LED on the right (UVTOP, 255-TO18-FW) emits light with a wavelength of 308.5 nm and a FWHM of 11 nm. It was mounted into a LED mount, which was temperature controlled, and connected to a stabilised power supply (Thorlabs, LTC100). The light was then split into two beams: the probe beam (top) and the reference beam (bottom). Both beams were imaged spaced apart onto the entrance slit of the spectrograph. This allows to counteract fluctuation of the LED.

The spectrograph (on the left) was a 0.5 m Czerny-Turner imaging spectrograph (Andor, SR-500i) and was equipped with a non-intensified CCD camera (Andor, Newton DU940P-BU2, 2048 × 512 pixels of 13.5 µm x 13.5 µm size) with a sensor that was cooled to -80 °C.

In order to measure the absorption through the plasma, the plasma emission has to be subtracted as can be seen from following equation:

$$T(\lambda) = \frac{I_T(\lambda)}{I_0(\lambda)} = \frac{I_{\mathrm{PL}}(\lambda) - I_P(\lambda)}{I_L(\lambda) - I_{\mathrm{BG}}(\lambda)} = \exp(-\sigma(\lambda) \cdot L \cdot n) \tag{2.7}$$

with $T(\lambda)$ the transmission, $I_T(\lambda)$ the transmitted intensity, $I_0(\lambda)$ the intensity without plasma, I_{PL} the intensity with plasma and lamp on, I_{P} the plasma emission, I_{L} the intensity of the lamp and, I_{BG} the background intensity. This resolves into the above mentioned

Beer-Lambert equation (2.6). The measurement cycles through the following sequence:

1. plasma on ,LED on
2. plasma off, LED on
3. plasma on, LED off
4. plasma off, LED off

The four intensities were measured over the course of several cycles and the images from the camera were saved so they can be processed by an in-house Matlab script. The Matlab script extracts the spectra from the images and exported it so the they could be fitted by an in-house software. The spectra were fitted to a simulated OH spectrum, calculated by the in-house software, in order to determine the density and rotational temperature.

It simulates the $OH(X^2\Pi_J, v' = 0)$ - $OH(A^2\Sigma_J, v'' = 0)$ rotational spectrum for absorption for an isothermal state population distribution. The line shape was assumed to be Gaussian, which was correct for the slit function of the spectrograph.

Figure 2.10 depicts an example of an experimental spectrum (black) overlaid with a simulated spectrum (red). One can see that both spectra agree well. The FWHM was fitted with 0.04 nm and the temperature with (329 ± 3) K.

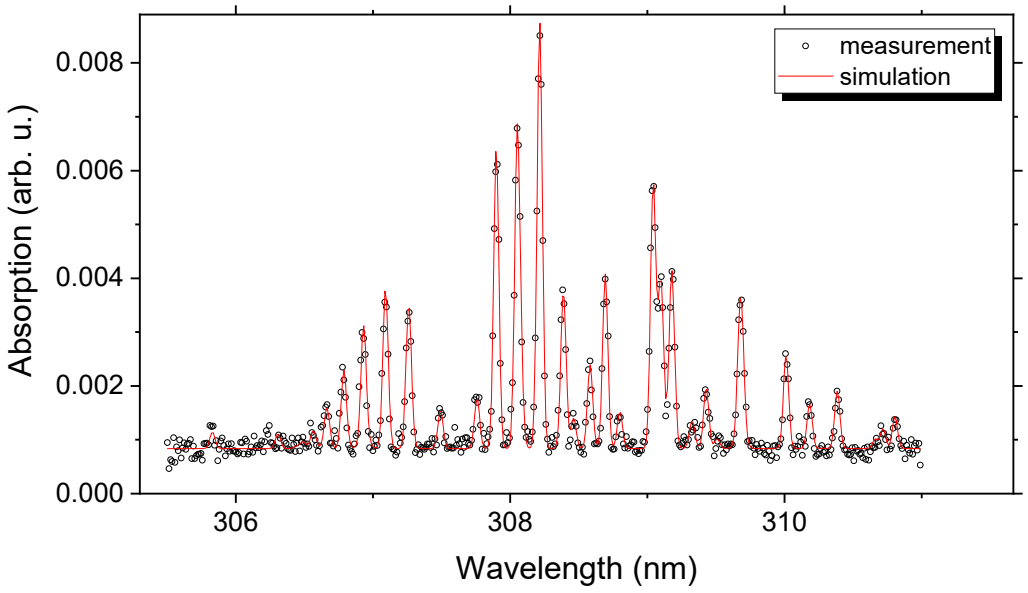

Figure 2.10: Measured OH spectrum (black) and simulated OH spectrum (red). The spectrum was measured in the middle of the modified COST jet. Conditions: 5 slm Helium, 4400 ppm water admixture, 500 V_{pp}

Ozone absorption

Ozone was measured using a commercial ozone meter (2Btech Model 106-L). This model uses a 254 nm LED to measure ozone absorption, has a precision of greater than 1.5 ppb (1 σ @ 10 s average), a minimum detection limit of 3.0 ppb and a linear response up to 100 ppm. The device sucks in air with approximately 1 slm through an absorption cell of 15 cm length. It uses two cycles to measure the absorption. In the first part of the cycle, the sample air was sucked in through an ozone scrubber to measure the background. In the second part the sample air was sucked in without the ozone scrubber to measure the ozone concentration. Before measurements, the ozone monitor was warmed up for 30 min and zeroed with an external ozone scrubber.

As shown in figure 2.8, species can have overlapping absorption cross sections. This can interfere with the measurement of ozone because the ozone and hydrogen peroxide cross sections overlap. To estimate the selectivity S for ozone, in this case, both cross sections in the region of 254 nm will be compared:

$$S = \frac{\sigma_{o_3}}{\sigma_{H_2O_2}} = \frac{1.15 \times 10^{-17} \mathrm{cm}^2\,\mathrm{molec}^{-1}}{6.88 \times 10^{-20} \mathrm{cm}^2\,\mathrm{molec}^{-1}} \tag{2.8}$$

with σ_{o_3} and $\sigma_{H_2O_2}$ the cross sections for ozone and hydrogen peroxide, respectively. $\sigma_{H_2O_2}$ was taken from [116]. S can be interpreted as the relative response of the ozone measurement to hydrogen peroxide. In this case $S = 167$ or $1/S = 0.006$. This means that one ppb of hydrogen peroxide would result in a wrong measurement of 0.006 ppb of ozone [120].

Ozone was measured in the effluent of the COST jet and the modified COST jet.

In case of the modified COST jet, the ozone monitor was connected 1 m after the plasma with a T-connector to the tube (Swagelok PFA-T4-047-100) (figure 2.11a). This was done because the H_2O_2 was measured at the same distance. The ozone meter sucked in the effluent with 1 slm and the rest was sent to the laboratory exhaust system.

In case of the COST jet, the ozone monitor could not be connected directly to the jet because the design was aimed to be used for direct treatments of surfaces. Figure 2.11b shows the solution to this problem. A glass funnel in front of the jet collects the effluent and transports it via a 1 m long tube (Swagelok PFA-T4-047-100) to the detector. Both, the glass and the tube do not effect the ozone density, thus the observed ozone densities are in the far effluent and comparable to measurements with the modified COST jet.

It was tested if the setup influences the ozone density by placing the jet in different positions and angles in the setup. It was found that the ozone density was not effected as long as the electrodes were placed a few centimetres within the collector setup and the jet is roughly (within $\pm 15°$) pointed at the tube inlet.

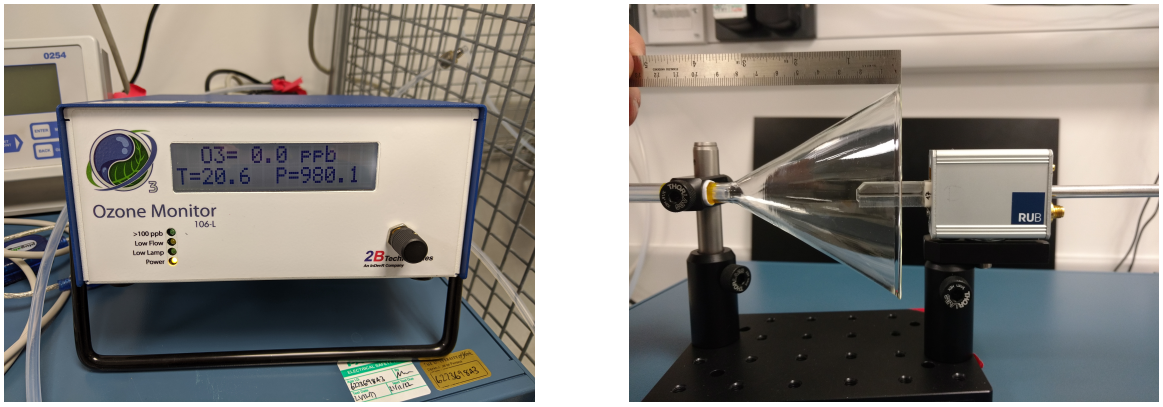

a) b)

Figure 2.11: a) Image of the 2Btech ozone monitor. b) Image of the effluent collector setup to measure the ozone produced by the COST jet.

2.5 Optical Emission Spectroscopy

Optical emission spectroscopy is a passive method to measure the electromagnetic emission of plasmas. It is non-intrusive and does not alter the plasma. Four ways exist to extract data from emission spectra: From the emission lines, it is possible to identify atomic or molecular species in the plasma but it is not possible to determine the densities without further calibration. With calibration, it is possible to determine the ground state density or temperatures with the aid of models. Common models are the collision radiative or corona model. By looking at relative line intensities temperatures can be determined. With assumptions about the energy distributions, such as Maxwell Boltzmann, it is possible to determine the electron temperature. From the line shape, such as Doppler- or pressure-broadening, the electron density or the ion temperature can be measured. All of these analyses utilise models that describe the plasma. In the following text, the basic physics behind optical spectroscopy will be elaborated further.

In order to observe optical emission an atom or molecule has to be excited to a higher state i. This occurs through electron collisions or other photons in the plasma.

The emission intensity from a higher state i to a lower state j I_{ij} is proportional to the photon energy $\mathrm{E_{photon}} = \mathrm{h}\nu$, the density of state i, and the Einstein coefficient A_{ij} . This can be also linked to the ground state density n_g by

$$I_{ij} \propto h\nu_{ij} n_i A_{ij} \propto n_e k\left(T_e\right) n_g A_{ij} \tag{2.9}$$

where n_e is the electron density and $k(T_e)$ is a factor depending on the electron temperature.

The inverse of the Einstein coefficent A_{ij} is the natural lifetime τ_{ij}. The lifetime of an excited state can be shortened by collisions with other particles through a process known as quenching. The rate depends on the partial pressure of the quenching partner:

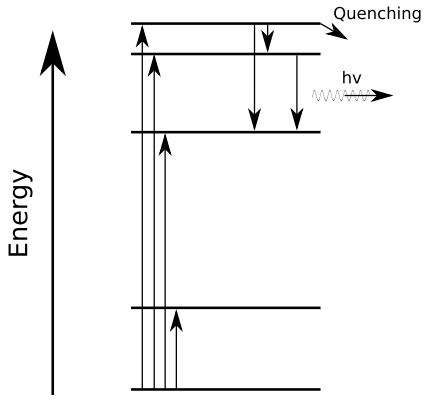

Figure 2.12: Excitation, de-excitation, cascading and quenching can occure in systems with mor than two levels.

$$\tau_{ij} = \frac{1}{A_{ij} + \sum Q_i} \tag{2.10}$$

The different states of an atom are not necessarily excited from the ground state. Stepwise de-excitation as well as radiation less de-excitaition can occur (see figure 2.12). This indicates that not all lines can be directly linked to the ground state which requires the knowledge of states feeding into specific excited states.

Instrumental broadening is caused by the entrance slit of the spectrometer and does not originate from physical forces or velocity distributions from the emitting atom or molecule. For most spectrometer the instrumental broadening shape is Gaussian and all lines observed are convoluted with this Gaussian shape.

Atoms and molecules are in motion which is governed by the temperature. This causes the emitted light to be Doppler shifted and broadening the FWHM, $\Delta\lambda_D$ of the specific line:

$$\Delta\lambda_D(\text{nm}) = 7.162 * 10^{-7}\lambda_0\sqrt{\frac{T_{gas}}{M}} \tag{2.11}$$

with λ_0 being the wavelength in nm, T_{gas} the gas temperature in K and M the atomic mass of the emitting species in atomic mass units [121].

An additional effect in atmospheric pressure plasmas is pressure broadening. The gas density in atmospheric pressure is high enough that Van der Waals forces become important due to the small space between the atoms and molecules. In atmospheric pressure the pressure broadening can be evaluated as follows:

$$\Delta\lambda_{vdW}(\text{nm}) = \frac{5.24}{T_g^{0.7}}. \tag{2.12}$$

Other broadening mechanisms, such as stark broadening exist, but are of no interest in this

work.

OES was measured on the COST jet. The measurement point was in the middle of the jet as can be seen in figure 2.13. A special designed cover to ensure that the same measurement point is used in different labs has been used and will be discussed in more detail in the section 3.

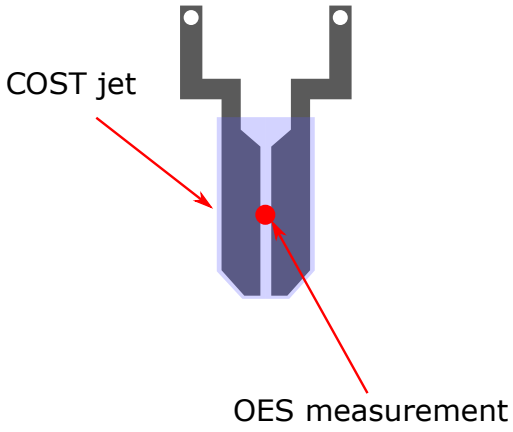

Figure 2.13: COST jet OES measurement point in the middle of the electrode assembly.

2.6 Fourier-transform infrared spectroscopy

Fourier-transform infrared spectroscopy (FTIR) is an optical absorption spectroscopy method used to measure vibrational and rotational spectra of molecules in the infrared. Shorter wavelength are also used, but require more elaborate equipment than tabletop devices [60]. FTIR has been widely used to detect species in the plasma and the effluent [67, 122–124].

Figure 2.14 shows the basic setup of a FTIR. This consists of a Michelson interferometer which includes an infrared broadband source, one moveable and one fixed arm and a detector. The sample is usually placed in the arm of the detector.

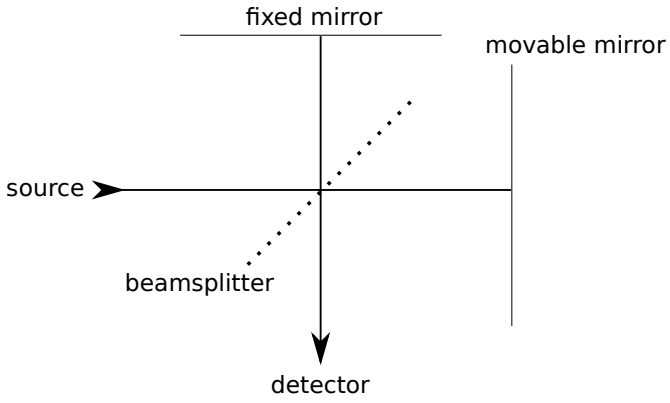

Figure 2.14: FTIR setup which mainly consists of a Michelson interferometer with an infrared broadband source, one fixed and one movable arm and an infrared detector.

FTIR has two main advantages over conventional absorption spectroscopy which are the Fellgett's (multiplex) and the Jacquinot's (throughput/Etendue) advantage. The Fellgett's advantage is the capability to measure several wavelengths simultaneously. This results in a better SNR of a spectrum measured with the same resolution and time per spectral element than with a conventional prism or grating based spectrometer. Jacquinot's advantage originates in the fact that the FTIR spectrometer does not use slits, like the grating based spectrometer, to achive optical resolution.

The resolution $\Delta\widetilde{v}$ of an FTIR is equal to the inverse optical path difference $\Delta_{\max}$ the moving mirror travels for one measurement:

$$(\Delta\widetilde{v}) = (\Delta_{\max})^{-1} \tag{2.13}$$

This indicates that the longer the mirror travels, the higher the resolution. The position of this mirror is measured by a helium-neon laser by counting the interference rings and is as accurate as the laser wavelength itself.

Transforming the raw data would be the equivalent of using a boxcar window which will result in peaks with many artificial side lobs. By applying an appropriate window, also known as apodization function, such as the Blackman-Harris 3-Term, one can resolve peaks without side lobs. More on apodization functions can be found in Harris et al. [125].

2.6.0.1 FTIR Setup

Figure 2.15 shows the FTIR setup used for this work. Figure 2.15a shows the schematic of the setup and figure 2.15b shows a photo of the setup. The gas is supplied on the left side by mass flow controllers to the plasma directly or through a bubbler in a temperature controlled bath, at 19 °C. The wet gas is then added to the dry gas stream before the plasma jet. In this experiment only helium is used as a carrier gas for water and oxygen admixture. The plasma source is the modified COST jet, which has the advantage of being a closed source with swagelok connectors that are connected by a 1 m long Perfluoroalkoxy alkanes tubes to a temperature controlled long path absorption cell with 5 m absorption path and approximately 250 ml volume. The temperature in the long path absorption cell is set to 29 °C. The long path ensures that the effluent is in equilibrium. The time the effluent takes to travel is approximately 150 ms which, according to global kinetics simulations, is enough time to equilibrate the chemistry as can be seen in. The tube is directly connected to the multipath absorption cell with a 5 m long absorption path. The cell is fitted into the FTIR (Bruker Vertex 70) and the whole setup is continuously purged with liquid nitrogen when not in use.

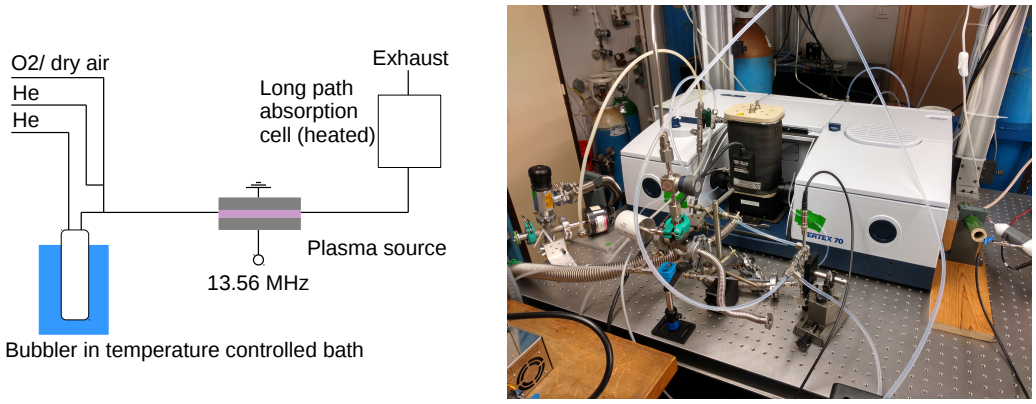

Figure 2.15: Schematic (a) and photo (b) of the FTIR setup to measure hydrogen peroxide.

Measurement and analysis

The spectrograph was refilled every day with liquid nitrogen to cool down the detector to keep it at a temperature that achieves the best possible signal to noise ratio. After this, several spectra were taken to see if the background changes. If this was not the case, the measurements were started.

The spectra were taken with a resolution of 0.2 cm^{-1} with an average of 30 scans. The aperture was set to 2.5 mm and the apodization function is a Blackman-Harris 3-Term function (see equation 2.14) which reduces the side lobes by -67 dB. The zerofilling factor for the FFT was 2. This leads to an interferogram size of 53318 points and, with zerofilling, to a FT size

of 128 K. The spectra were saved from 500 cm^{-1} to 4000 cm^{-1}.

$$0.42323 - 0.49755 \cdot \cos(\frac{\pi \cdot x}{g}) + 0.07922 \cdot \cos(\frac{2 \cdot \pi \cdot x}{g}) \quad \text{with} \quad g = 2 \tag{2.14}$$

Equilibration time between measurements was 10 min. This was the time after which no significant changes occur. The plasma on measurements were taken first. After which, the background without the plasma were taken.

The background and plasma spectra were subtracted and the baseline was corrected by a python script. This script utilises the HITRAN python API [126] to download the spectra and apply apodization functions to the hydrogen peroxide spectra. The API does not provide the Blackman-Harris 3-Term apodization function and is complemented by the function. The script also fits the theoretical spectra to the experimental spectra. All theoretical spectral data is taken from HITRAN and its underlying sources [127].

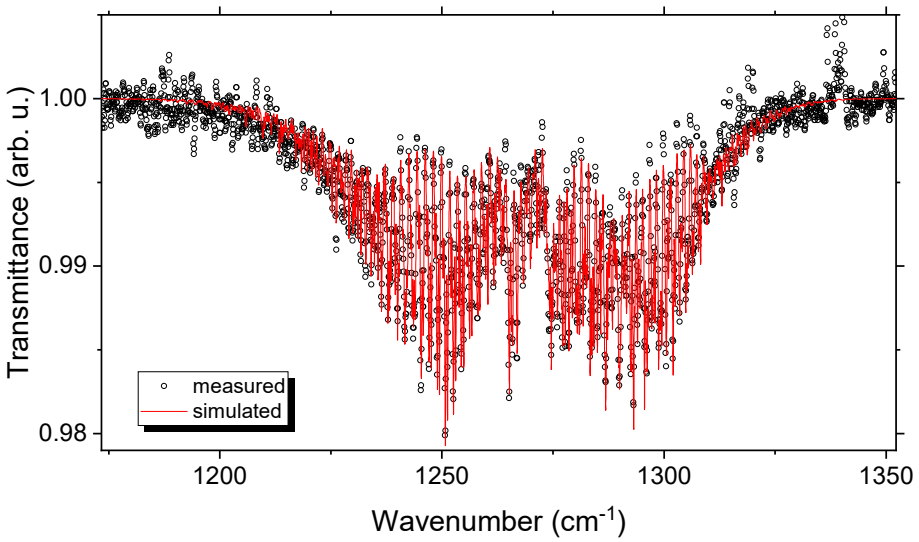

Figure 2.16: Comparison of measured (black circles) and simulated (red line) hydrogen peroxide spectrum. Conditions: 5 slm total helium flow, 4400 ppm water admixture, 178 V_{RMS}.

Figure 2.16 shows the measured hydrogen peroxide spectrum (black dots) overlayed with a calculated spectrum (red line). For this fit, the temperature was set to the temperature of the long path absorption cell. This leaves only the hydrogen peroxide density as a fitting parameter.

Chemical equlibrium

The tube between the modified COST jet and the long path absorption cell in this setup was approximately 1 m long and had an inner diameter of 4 mm. With a flow rate of 5 slm,

the gas velocity in the tube was 6.6 m/s. Therefore the chemistry in the effluent has 151 ms to equilibrate. This is depicted in figure 2.17.

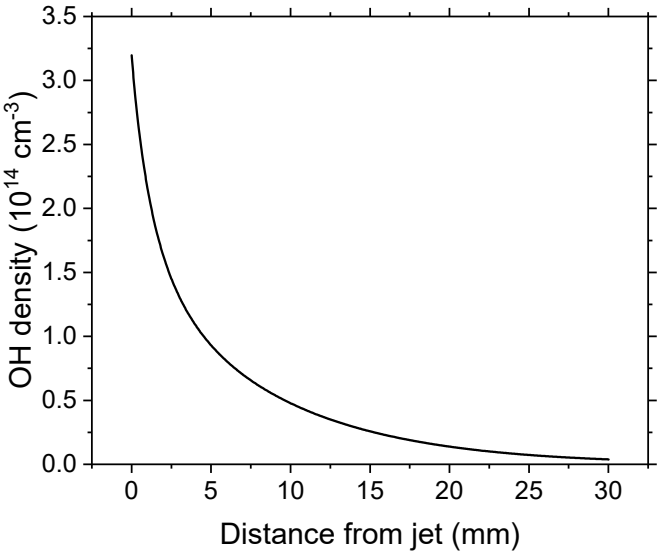

Figure 2.17: GlobalKin study of OH . The density rapidly decreases after the plasma. Conditions: 0.5 slm helium, 4400 ppm water admixture and 178 V_{RMS}.

The second important parameter, was the time between changing an input parameter and seeing a change in the hydrogen peroxide densities. This is shown in figure 2.18. The conditions were 5 slm total helium flow and 2464 ppm water admixture at a voltage of 178 V_{RMS}. The water was set to the desired admixture and the spectra were taken directly after that in 5 min intervals up to 25 min. The densities remained stable at $(8.00.8\pm) \cdot 10^{13} cm^{-3}$ over the whole period of time. This suggests, that the response to the changed water admixture is beyond the measuring time required for one spectra.

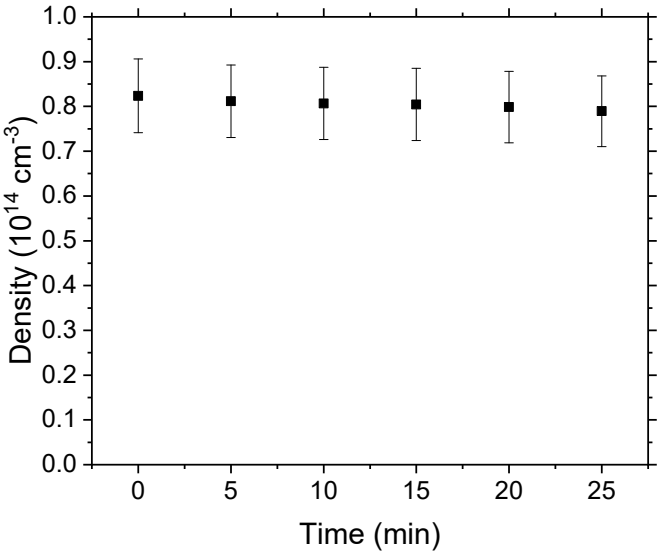

Figure 2.18: Hydrogen peroxide density over a timespan of 25 minutes. Conditions: 5 slm total helium flow, 2464 ppm water, 178 V_{RMS}.

2.7 Laser induced fluorescence

Laser induced fluorescence (LIF) spectroscopy is an active technique to detect species in the effluent or in the plasma. The sensitivity is better than in absorption spectroscopy and allows measurements with spatial resolution. This is because absorption measurements compare small differences in transmission rather than a fluorescence signal from a dark background. Additionally, it is easier to record the spatial resolution of a florescence signal with a camera accurately. On the other hand, it is not possible to measure the density of multiple species simultaneously.

LIF and two photon absorption LIF (TALIF) have been used extensively in the past for atmospheric and combustion research under similar challenging environments as atmospheric pressure plasma jets.

The main challenge in atmospheric plasma jets used for biomedical applications is the air admixture in the effluent of the plasma. This can quench the excited species and thus shorten the excitation lifetimes drastically from several tens of ns to single digit excitation times. If the laser pulse is in the order of magnitude to the excitation times it can be a problem to de-convolute laser pulse and excitation decay. This has been done successfully before (see [57, 128, 129]) but under controlled atmosphere, such as helium, in which the quenching partner were known or could have been estimated. This makes it necessary to use a sub-nanosecond pulsed laser for species such as atomic oxygen to measure absolute densities in air or plasmas with complex chemistry.

Despite the advantages of LIF techniques, some species, such as hydrogen peroxide, can not be measured directly. In this case hydrogen peroxide can be dissociated by UV-photons from a second laser to hydroxyl. This hydroxyl will then be detected by LIF.

In the following, first a simple introduction to LIF and TALIF techniques is presented before going into details about detection and quantification of atomic oxygen, hydroxyl and hydrogen peroxide produced by the plasma and measured in the effluent in the gas phase.

2.7.1 Prinicples of laser induced fluorescence

The principle of the LIF technique is to shoot a laser through the plasma or the effluent to excite a particle from lower state l to an upper state u. The excitation rate from l to state u is given by $B_{lu}I_L$, with B the Einstein coefficient and I_L the laser light intensity.

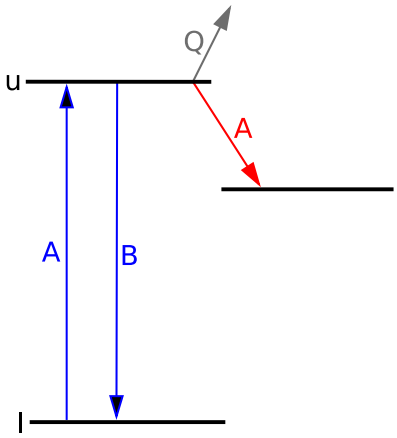

Figure 2.19: Simplified three level LIF scheme with lower state l, upper state u and an intermediate state state. Also depicted are the Einstein coefficients A and B and the the quenching coefficient Q.

As can be seen in figure 2.19, the particle is de-excited through three channels: spontaneous emission to various lower sates with spontaneous emission coefficient $A_u = \sum_i A_{ui}$, quenching Q (de-excitation through collisions) and stimulated emission with Einstein coefficient B_{ul}. The rate coefficient for the upper state is:

$$\frac{dn_u(t)}{dt} = B_{lu}I_L n_l(t) - (B_{ul}I_L(t) + A_u + Q)n_u(t) \tag{2.15}$$

It is desired to keep the stimulated emission rate as low as possible in order to make sure that the majority of fluorescence comes from natural de-excitation. Hence, the laser intensity should be kept low. Additionally it is assumed that $n_l \gg n_u$. Therefore, the ground state rate equation can be neglected and the formula becomes:

$$\frac{dn_u(t)}{dt} = B_{lu}I_L(t)n_l - (A_u + Q)n_u(t) \tag{2.16}$$

The solution to this equation is:

$$n_u = B_{lu} n_l \int_0^t I_L e^{-(A_u+Q)(t-t')} dt' \tag{2.17}$$

and becomes this after the laser pulse:

$$n_u(t) = n_u e^{-(A_u+Q)(t)} \tag{2.18}$$

As can be seen from equation 2.17, it is convenient to have a short laser pulse to keep the influence of the integral as small as possible. In this case, the influences of $A_u + Q$ were kept small during the laser pulse and it can be assumed that the entire population of the upper state u is populated by the laser pulse at once. If A_u is well known, even the quenching rate can be measured.

However, short laser pulses have a disadvantage. Generally, the shorter the pulse the broader the spectral FWHM of the laser pulse. Therefore, it might not be possible to excite specific states of a molecule or atom in isolation.

The measured signal is in intensity and one typically needs more setup specific information, such as quantum efficiency of the detector or transmission of the optics, to convert the intensity to absolute densities. But one can observe from above equations that the following proportionalities can be made:

$$I_{LIF} \propto n_l I_L. \tag{2.19}$$

and the TALIF signal is proportional to the square of the laser intensity because two photons were needed to excite the atom or molecule:

$$I_{TALIF} \propto n_l I_L^2 \tag{2.20}$$

As the atoms or molecules have to absorb the laser light, the same problems as observed in absorption spectroscopy regarding absorption cross sections apply. Additionally, photo fragmentation can play a role in lowering the output of the fluorescence [130]. Therefore, the linearity/quadratic characteristics of the LIF/TALIF signal must be verified. A problem with LIF techniques is that they do not give absolute densities. Therefore, a calibration is indispensable.

2.7.2 Atomic oxygen TALIF

In the following, the experimental procedures to obtain absolute densities of atomic oxygen are explained. The order of the sections is in the order of working through the experiment to obtain absolute atomic oxygen densities.

Calibration

TALIF does not produce absolute values of the studied species. However, a calibration with atomic oxygen would require a source with known characteristics. This is not possible given the technological state today. Atomic species, such as atomic oxygen, tend to be unstable and react quickly to oxygen or other more stable molecules. Instead, the fluorescence signal of atomic oxygen was compared to a noble gas with a similar atomic structure, for the purpose of this work, xenon, and known density n_{cal}. More details can be found in the literature [131, 132].

$$\frac{S_{\mathrm{F,x}}}{S_{\mathrm{F,cal}}} = \frac{\eta_{\mathrm{x}}\left(\lambda_{\mathrm{F,x}}\right)}{\eta_{\mathrm{cal}}\left(\lambda_{\mathrm{F,cal}}\right)} \frac{T_{\mathrm{x}}\left(\lambda_{\mathrm{F,x}}\right)}{T_{\mathrm{cal}}\left(\lambda_{\mathrm{F,cal}}\right)} \frac{a_{12,\mathrm{x}}}{a_{12,\mathrm{cal}}} \frac{\sigma_{\mathrm{x}}^{(2)}}{\sigma_{\mathrm{cal}}^{(2)}} \frac{n_{\mathrm{x}}}{n_{\mathrm{cal}}} \frac{I_{\mathrm{x}}}{I_{\mathrm{cal}}} \tag{2.21}$$

with I the flourescence signal, η_{x} and η_{cal} the quantum efficiency for the detector, T the temperature, a the branching ratio, T the transmission and $\sigma^{(2)}$ the two photon excitation cross section. If the laser characteristics, spatio- and temporal, were the same for measurement and calibration, I can be substituted for the laser pulse energy E as follows:

$$\frac{S_{\mathrm{F,x}}}{S_{\mathrm{F,cal}}} = \frac{\eta_{\mathrm{x}}\left(\lambda_{\mathrm{F,x}}\right)}{\eta_{\mathrm{cal}}\left(\lambda_{\mathrm{F,cal}}\right)} \frac{T_{\mathrm{x}}\left(\lambda_{\mathrm{F,x}}\right)}{T_{\mathrm{cal}}\left(\lambda_{\mathrm{F,cal}}\right)} \frac{a_{12,\mathrm{x}}}{a_{12,\mathrm{cal}}} \frac{\sigma_{\mathrm{x}}^{(2)}}{\sigma_{\mathrm{cal}}} \frac{n_{\mathrm{x}}}{n_{\mathrm{cal}}} \left(\frac{E_{\mathrm{x}}}{E_{\mathrm{cal}}} \frac{\lambda_{\mathrm{x}}}{\lambda_{\mathrm{cal}}}\right)^2 \tag{2.22}$$

Combining all constants that are unique to the setup in a calibration factor C gives

$$\frac{S_{\mathrm{F,x}}}{S_{\mathrm{F,cal}}} = C \frac{a_{12,\mathrm{x}}}{a_{12,\mathrm{cal}}} \frac{n_{\mathrm{x}}}{n_{\mathrm{cal}}} \tag{2.23}$$

This shows the six variables that have to be measured experimentally. These are two times the laser energies, two times the transmission of the optics, and two times the laser signal S.

Xenon

Figure 2.20 shows the TALIF schemes for atomic oxygen and the calibration atom xenon. One can see that both, ground ($\mathrm{O(2p^4\ ^3P_J)}$) and upper ($\mathrm{O(3p\ ^3P_J)}$), states of the oxygen are split into three fine structure sub-levels of J = 0,1,2. The ground state level are several hundred wave numbers apart but the upper state level lie within on wavenumber. This means that any excitation from the ground state with the picosecond laser will populate all three upper states.

Figure 2.20 shows why xenon was chosen as a calibration gas. Both, the excitation and the fluorescence, wavelengths are very close to atomic oxygen. The de-excitation scheme of xenon, however, differs slightly. There are two ways, apart from quenching, the de-excitation can happen. Therefore, the branching ratio for both states has to be taken into account. In this case it was purely optical and was $b = \frac{A_{12}}{A_1} = 0.733$ [93].

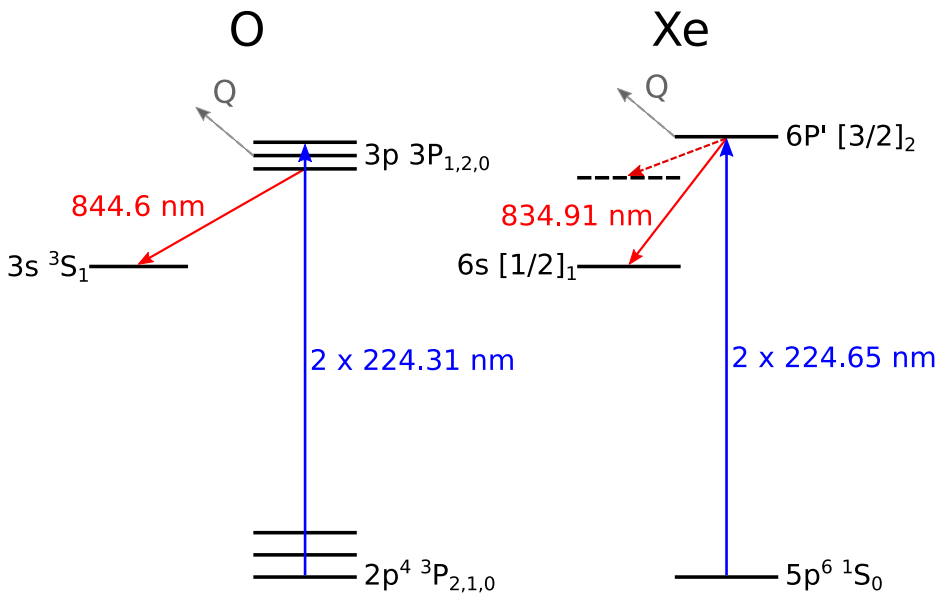

Figure 2.20: TLAIF schemes for atomic O and the calibration gas Xenon. Levels are assigned according to [93, 132, 133].

TALIF setup

In this work, two TALIF systems were used to measure the absolute atomic oxygen density. Both systems differ in the type of laser and camera used. One laser produces 30 ps long laser pulses and was tunable from 193 nm to 2300 nm with a linewidth of 4 cm^{-1}. This laser consisted of a Nd:YAG pump laser (EKSPLA PL2251, 10 Hz), a harmonic generator, and amplifier (EKSPLA H400 and APL 2100), and a solid state optical parametric generator (EKSPLA PG411).

The other laser (Continuum Electro-Optics, inc Model SL-EX, with a Horizon) produces 4 ns long pulses and was tunable from 192 nm to 2750 nm with a linewidth of 7 cm^{-1}.

The 30 ps laser was needed to resolve the radiative lifetime of the atomic species that was shortened to a ns scale by quenchers from the plasma and atmosphere.

In this work, the jets were setup in the TALIF systems and measuring parameters with the best signal-to-noise ratio were found.

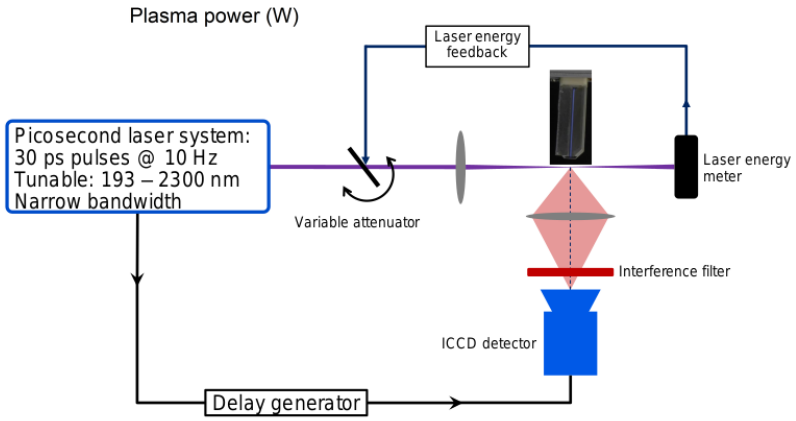

Figure 2.21: TALIF setup for the pico- and nano-second laser. Both setups were identical but for the laser.

Figure 2.21 shows the TALIF setup. It consisted of one of the lasers mentioned above. After the laser system, a variable attenuator was placed which consisted of a variable attenuator plate and a compensator plate (Layertec). These were mounted on a counter rotational stage (Zaber T-NM17A04). The attenuation was controlled by the incident angle of laser and plate. This can divert the laser beam and was compensated for with the compensator plate ensuring no beam diversion or offset. The laser energy was monitored by a laser energy meter (Gentec-EO, QW8SP-B-MT) which output was fed into a PID process. This controls the variable attenuator. This feedback loop kept the laser energy at the desired level, and compensated for long-term drifts which can occur over the duration of a day. The feedback loop was able to keep the laser energy standard deviation below 5 % and the fluorescence signal was accumulated over a duration of 128 to 256 shots, depending on the signal strength.

In case of the picosend laser, the flourescence was detected by a fast iCCD camera with the following specs: 4Picos dig Stanford Computer Optics, 1024×1024 pixels, $(8.3 \times 8.3)\,\mu m^2$ pixel size, S25IR photo cathode). The nanosecond laser setup used a similar camera with these specifications: Andor iStar DH344T-18U-73 , 780×580 pixels.

Both cameras were placed in a 90° angle to the laser beam. In both cases, the flourescence signal was imaged onto the iCCD with two achormatic lenses (Thorlabs AC050-010-B-ML). Both lenses had a focallength of 8 cm, which when combined, resulted in a focal length of approximatly 4 cm. This increased the detection angle and therefore the signal to noise ratio. The transmission coefficient, according to the manufacturer, was 99 % for all the wavelengths of interest. Possible stray light from the laser was filtered by 845 nm and 835 nm for atomic oxygen and xenon, respectively, interference filter with a spectral bandwidth of 10 nm. The filter was mounted onto the camera directly in front of the sensor.

The laser was focused into a spot of a few hundred micrometers allowing spatial resolution in the same order of magnitude.

The COST jet TALIF measurements were taken directly at the tip of the jet as can be seen

in figure 2.22

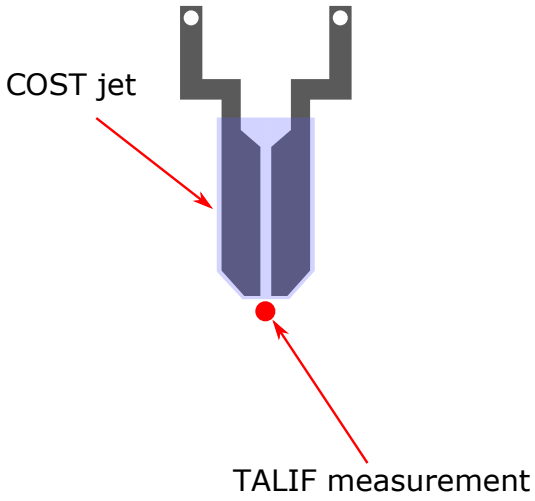

Figure 2.22: TALIF measurement point directly under the tip of the plasma jet.

Measurement

As previously discussed, several quantities have to be measured in order to obtain absolute numbers of atomic oxygen. These quantities were the time integrated fluorescence signal, the decay rate of the signal and the spectral integrated fluorescence signal.

Spatial integration was done by defining a region of interest (ROI) on the camera image and sum over all pixels in this region. This reduced the spatial resolution but greatly improves the signal to noise ratio.

The spectral integrated signal was recorded by integrating the intensity over the whole laser pulse in 0.01 nm steps over the atomic oxygen peak at 225.64 nm $\pm$ 0.01 nm (See figure 2.23c).

The decay rate of the signal was recorded by taking images with a gate width of 2 ns in 0.5 ps steps. The gate width does not influence the fluorescence lifetime. The recorded decay was then fitted with an exponential decay to obtain the lifetimes.

Energy saturation curve

With high laser energies, ionisation and photodissciation effects can dominate and the fluorescence signal was not proportional to the square root of the laser energy any more. To check this, the laser pulse energy was varied from zero to high powers and the time integrated TALIF signal measured.

Figure 2.23 shows the saturation curves for atomic oxygen and Xenon. Both show clear saturation effects at high laser intensities. The conditions for oxygen were 500 sccm helium

flow with 4400 ppm water admixture and 1 W plasma power and the measurement point was 1 mm in front of the jet. Xenon was measured with a pressure of 10 tor.

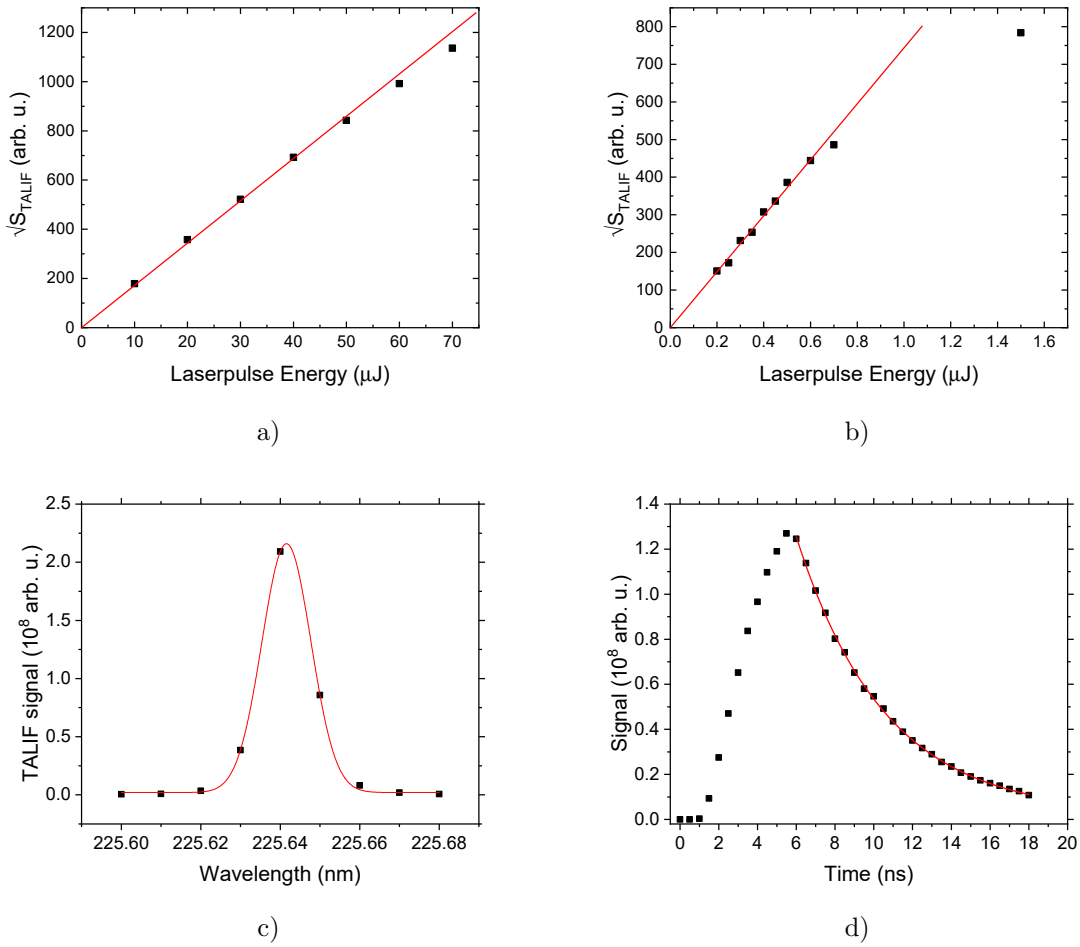

Figure 2.23: Energy saturation curves for atomic oxygen a) and xenon b). Atomic oxygen shows deviation from the square dependence at 45 µJ and xenon at 0.6 µJ. c) and d) exemplary raw data with fits from one measurement with the COST jet 1 mm from the electrodes with 500 sccm total helium flow, 300 ppm oxygen admixture and 178 V_{RMS}. c) depicts the wavelengthscan and the gaussian fit. d) depicts the time series measured at 225.64 nm. The red curve is the fitted exponential decay starting at 6 ns.

Figure 2.23c depicts the wavelengthscan (black) over the range from 225.60 nm to 225.68 nm in 0.01 nm steps. The red line is the Gaussian fitted to the data. The area under the fitted Gaussian was used to calculate the absolute densities. Figure 2.23d depicts the time series recorded at 225.64 nm. The time difference between each points was 0.5 ns, the shutter time was 2 ns

2.7.3 Hydroxyl LIF

Hydroxyl is one of the key radicals in plasmas for biomedical applications. It is not as reactive as atomic oxygen and, thus, can travel further in the plasma effluent. Over time, hydroxyl reacts to form hydrogen peroxide which is another key chemical for biomedical applications. Hydrogen peroxide can be directly detected by FTIR and UV absorption spectroscopy but both methods suffer from the low cross section in the UV and infrared regime. Therefore, it is difficult to get spatial resolution and calls for multipath absorption setups.

Another method is to indirectly detect hydrogen peroxide by photodissociation and detecting the hydroxyl that has been produced. This was part of this hydroxyl LIF experiment.

Hydroxyl LIF and photodissociation setup

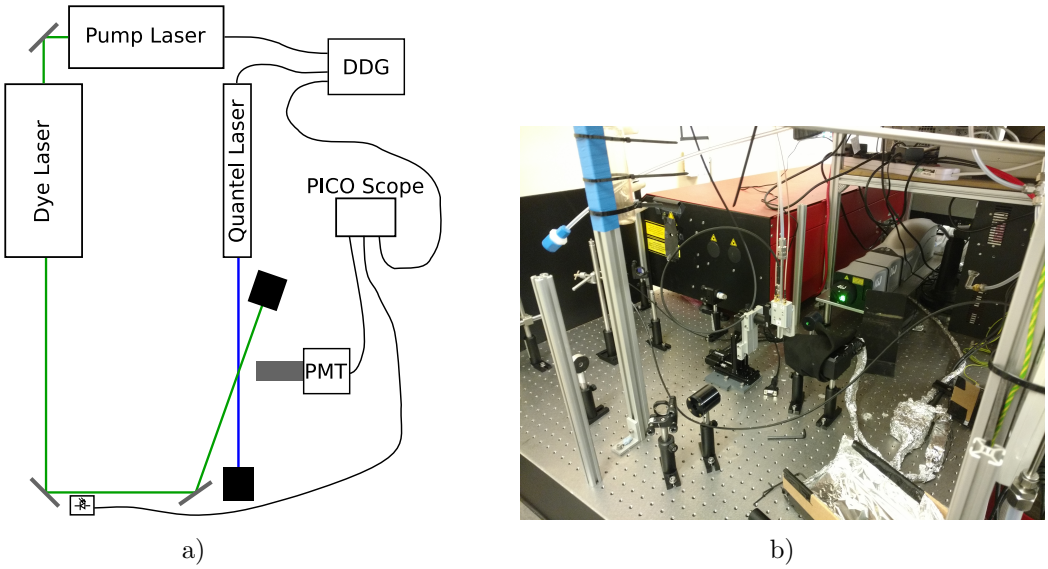

Figure 2.24: The hydroxyl LIF setup with the photodissociation laser.

The setup (as seen in figure 2.24) consisted of an hydroxyl probe laser and a photofragmentation laser. The optical path, with mirrors, and the plasma jets were set up. Additionally, the timings of the laser were optimised. Both lasers were controlled by a delay generator (BNC 575) used to control the delay between photodissociation and the hydroxyl probe laser and the delay between the flashlamp and the Q-switch of each individual laser. The hydroxyl probe laser was a Nd:YAG laser (Continuum Powerlite Precision) using the second harmonic (532 nm, 400 mJ per 6 ns pulse) to pump a Radiant Dye NarrowScan at 564 nm, in which the frequency was doubled (by potassium dihydrogen phosphate crystal) to detect hydroxyl via LIF at 282 nm. The delay between flashlamp and Q-switch was 350 µs. The laser energy was recorded with a photodiode for every shot. The photodiode was also calibrated with a laser energy meter to assign each voltage from the photodiode to a laser energy. The laser energy

typically used in these experiments was (15±3) µJ per pulse. The photofragmentation laser was a Nd:YAG laser (Quantel -Q-smart) using the fourth harmonic (266 nm, 100 mJ per 6 ns pulse) to photodissociate hydrogen peroxide or *tert*-Butyl hydroperoxid. The energy of each pulse could be controlled by the delay between the flashlamp and Q-switch. This was done because the photodissociation laser caused a saturating signal in the PMT. The delay was kept constant at 264.4 µs which led to a pulse energy of 64±3 mJ per pulse.

Figure 2.25 shows the optics setup of filters and lenses to image the flourescence signal onto the detector. The incoming light was filtered by a 309 nm interference filter (OptoSigma, VPF-25C-10-15-30710) and then focused by a Plano convex lense (OptoSigma, SLSQ-25.4-50p) and filtered by a 305 nm cut-off filter (Materion 8M848 - F-NB-0009650) before hitting the photomultiplier tube (PMT, Hamamatsu R11540). The signal from the PMT was collected by a PicoScope 5443B which also collects data from the laser photodiode to monitor the laser energy simultaneously for every shot.

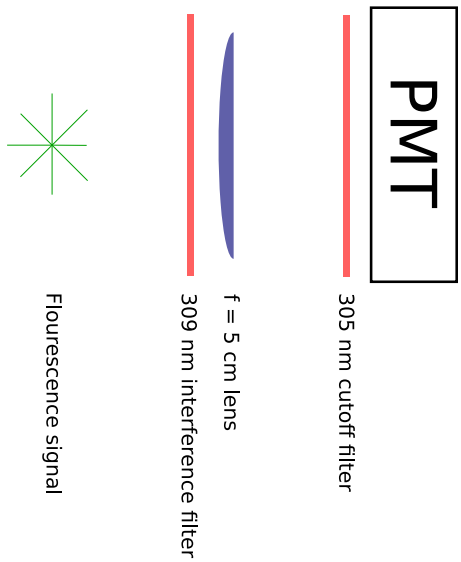

Figure 2.25: This is the optics setup showing the lens system and filters used to image the fluorescence signal onto the photomultiplier.

The measurement points were 9 mm up until 29 mm away from the tip of the jet as can be seen in figure 2.26. It could only be measured 9 mm from the jet because the photodissociation laser caused reflections that could be measured with the PMT.

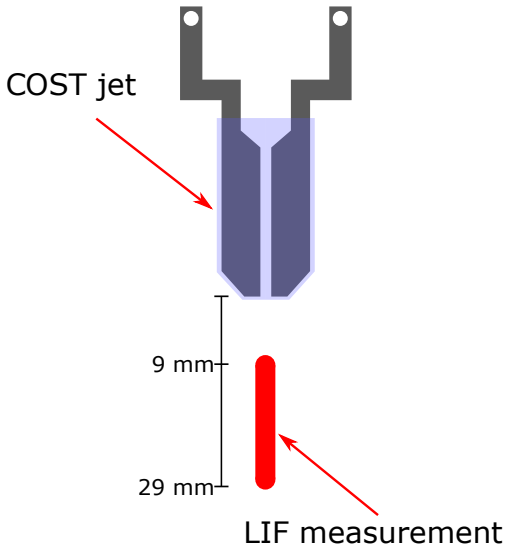

Figure 2.26: PDLIF measurement points 9 mm to 29 mm under the tip of the plasma jet.

The collected fluorescence signal was then stored for later processing with a Matlab script [134]. The Matlab script read out all oscilloscope waveforms, filtered out 13.56 MHz signal from the plasma jet, corrected the baseline and determined the area under the fluorescence pulse and fitted an exponential decay first order to determine the hydroxyl lifetime for every laser shot. Figure 2.27 shows an example of the signal acquired with and without the photolysis laser on.

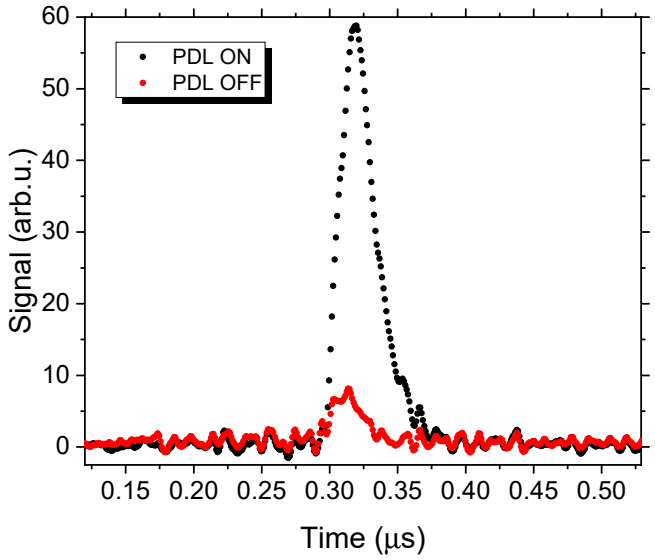

Figure 2.27: Typical LIF signal obtained from the setup. Conditions: 5 mm from the tube, 5 slm helium, 4400 ppm water, 178 V_{RMS}

Laser excitation Spectra of hydroxyl

In order to confirm that the measured laser excitation material originated from the intended hydroxyl line, an excitation spectra was recorded. Figure 2.28 shows the spectrum acquired with the hydroxyl probe laser over the wavelength range from 281.85 nm to 282.15 nm. This region should show five spectral lines if the resolution was high enough (dashed black line in figure 2.28, simulated with LIFbase). The red line represents the raw signal from the PMT normalized to the laser energy measured by the photo diode. The spectrum could not be recorded during one go because the frequency doubling crystal had to be retuned for maximum energy in order to scan over broad ranges of wavelengths. Additionally, both scanning and data acquisition had to be started simultaneously, which was done manually. Therefore, each spectrum could have a small wavelength offset. The two large peaks from the experiment overlapped with the double peaks from LIFbase. Meanwhile, the smallest peak on the right was in the same area as the R2(2) transition. This agreement of experimental and theoretical data shows that it was really the hydroxyl transitions that were measured.

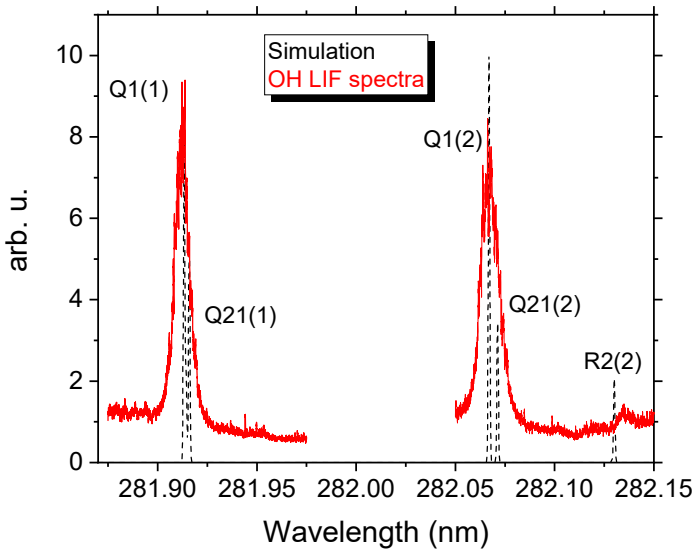

Figure 2.28: Hydroxyl LIF spectrum for OH(A,v'=0) $\longrightarrow$ OH(X,v"=0) overlayed with a spectrum from LIFbase

For the experiments, the Q1(1) transition was used to measure the hydroxyl densities. Figure 2.29 shows the transition excitation scheme for OH(A, v'=1) to OH(X,v"=0). The excitation scheme can best be described with a four level model.

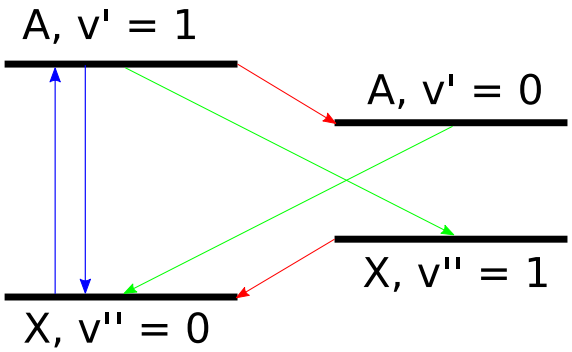

Figure 2.29: Four level model of the hydroxyl molecule.

The hydroxyl ground state was excited by 282 nm to OH(A,v'=1). The molecule then distributes the energy through vibrational energy transfer (VET) to OH(A,v'=0) and emits light with 308 nm wavelength by de excitation to OH(X,v"=0). Another de-excitation process occurred by de-excitation from OH(A,v'=1) to OH(X,v"=1) by emitting light with 316 nm. Quenching can occur from all excited states with different quenching coefficients for each level [135].

Hydroxyl calibration

In order to correlate the hydroxyl LIF signal from the photomultiplier with a known hydroxyl concentration the setup had to be calibrated. For this, a substance commonly used for hydroxyl generation, *tert*-Butyl hydroperoxid, was selected. The substance was introduced into the gas stream through a bubbler (see section 2.1) and then photodissociated by the photodissociation laser into hydroxyl and products:

$$(CH_3)_3COOH + h\nu(266\text{ nm}) \longrightarrow OH + \text{product}. \tag{2.24}$$

Because *tert*-Butyl hydroperoxid was in 70 % solution with water, it was difficult to calculate the exact amount of *tert*-Butyl hydroperoxid going into the gas stream. Furthermore the closest measurement point was 9 mm from the jet and it was unknown how much *tert*-Butyl hydroperoxid diffused out of the gas stream. A kinetics analysis was done to recalculate the concentration of *tert*-Butyl hydroperoxid in the gas phase. Additionally, a low gas flow of 200 sccm through the jet was chosen in order to observe the same volume of gas during the analysis. Without which the hydroxyl would have been blown past the hydroxyl probe laser. To test for clipping effects a distance variation was completed by driving the jet at $v = 0.1\,^{mm}/_{s}$ and recording the hydroxyl LIF signal with 10 Hz (see figure 2.30).

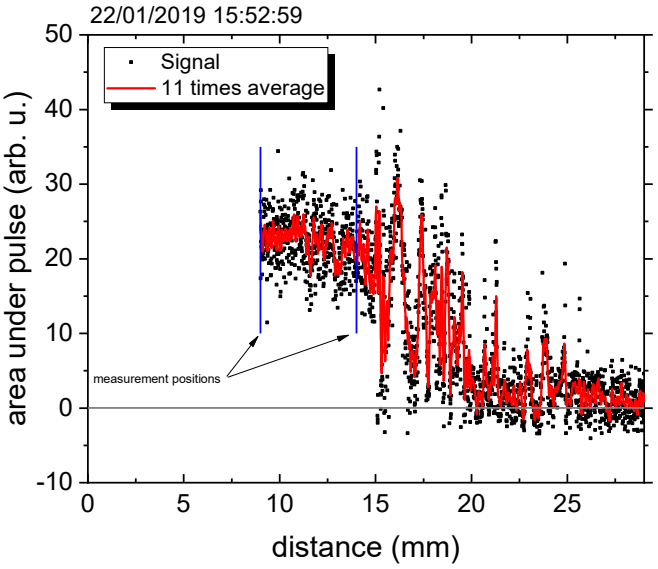

Figure 2.30: Distance variation from 9 mm to 29 mm distance to the jet using *tert*-Butyl hydroperoxid at 200 sccm helium flow and 5 sccm through the bubbler. 9 mm was the shortest distance usable without reflections from the photofragmentation laser. The black dots were the individual measurements and the red line was adjacent averaged with a window of 10 points. For clarification the zero line was drawn in gray and the points of measurement were shown with vertical blue lines.

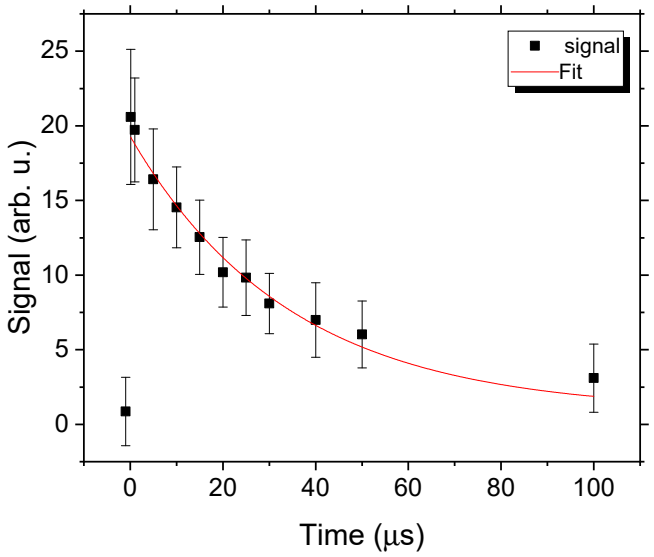

Figure 2.31: Chemical kinetics study to determine the amount of *tert*-Butyl hydroperoxid and thus hydroxyl 9 mm in from the jet. The fit function was an exponential decay first order. Conditions: 200 sccm helium and 5 sccm helium through the *tert*-Butyl hydroperoxid bubbler.

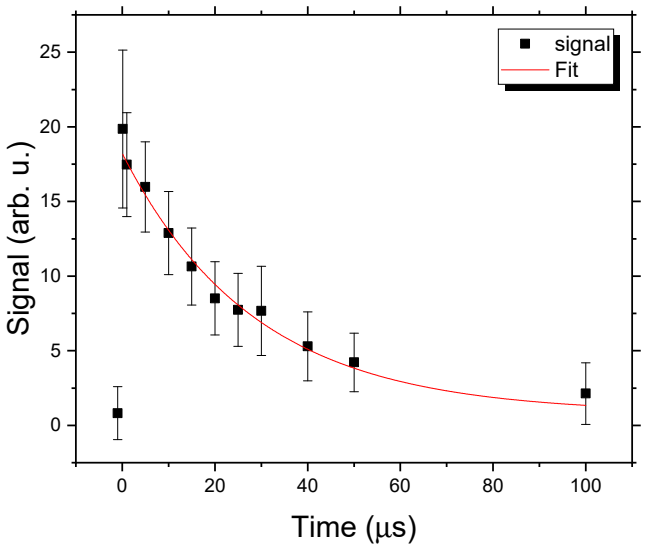

Figure 2.32: Chemical kinetics study to determine the amount of *tert*-Butyl hydroperoxid and thus hydroxyl 14 mm in from the jet. The fit function was an exponential decay first order. Conditions: 200 sccm helium and 5 sccm helium through the *tert*-Butyl hydroperoxid bubbler.

Figure 2.31 and 2.32 show the results of the calibration measurement at 9 mm and 14 mm respectively. Both initial values lie within errorbars, the same for the hydroxyl lifetime.
In order to calculate the absolute *tert*-Butyl hydroperoxid concentration the rate equation

$$\frac{dn}{dt} = k(T) n_{OH} n_{(CH_3)_3COOH} \tag{2.25}$$

had to be solved for $n_{(CH_3)_3COOH}$ which was assumed constant over time. Hereby, the rate $\frac{dn}{dt}$ and the reaction rate constant $k(T)$ were already known. With a known concentration of *tert*-Butyl hydroperoxid the produced amount of hydroxyl can be calculated by:

$$n_{\mathrm{OH}}(t=0) = \sigma(\lambda)\Phi(\lambda) n_{(CH_3)_3COOH} F \tag{2.26}$$

With $\sigma(\lambda)$ the cross section, $\Phi(\lambda)$ the quantum yield at this specific wavelength and $n_{(CH_3)_3COOH}$ the concentration of $(CH_3)_3COOH$ in the effluent and F was the photodissociation laser fluence (photons cm^{-2} per pulse). According to Baasandori et. al. [136] $\Phi(\lambda)$ was equal to 1. The laser fluence F can be calculated by knowing the photodissociation laser iris and the energy per pulse. Therefore, $F = {}^{(8.5\pm0.4)*10^{16}\,photons}/_{\pi*(0.7\,cm)^2} = (5.5 \pm 0.3) * 10^{16}\,photons\,cm^{-2}$. The UV absorption cross-section measured using a diode array spectrometer $\sigma(\lambda = 266\,nm) = 9.41 * 10^{-21}\,cm^2 molecule^{-1}$ is taken from [136]. This led to $n_{\mathrm{OH}}(9\,mm) = 4.1922\,cm^{-3}$ and $n_{\mathrm{OH}}(14\,mm) = 5.3308\,cm^{-3}$. The setup was the same for the calibration and measurement. Therefore, no measurements to calibrate the optics had

to be undertaken. The calibration formula is:

$$n_{\mathrm{OH}} = n_{\mathrm{OH}}^{cal} \frac{\tau^{cal} E^{cal} S^{jet}}{\tau^{jet} S^{cal} E^{jet}} \tag{2.27}$$

With n_{OH} the hydroxyl density, $n_{\mathrm{OH}cal}$ the calibration, OH density, E_{hydroxyl} and $E_{\mathrm{OH}cal}$ the energies for the calibration and measurement, S_{OH} and $S_{\mathrm{OH}cal}$ the LIF intensity for the measurement and calibration respectively. The hydrogen peroxide concentrations were determined by:

$$n_{\mathrm{H_2O_2}} \sigma_{\mathrm{H_2O_2}}(\lambda) \Phi_{\mathrm{H_2O_2}}(\lambda) F = (n_{\mathrm{OH}_{PLON}} - n_{\mathrm{OH}_{PLOFF}}) = \Delta n_{\mathrm{OH}} \tag{2.28}$$

With $n_{\mathrm{H_2O_2}}$ the hydrogen peroxide concentration, $\sigma_{\mathrm{H_2O_2}}(\lambda)$ the cross section of hydrogen peroxide at 266 nm , $\Phi_{\mathrm{H_2O_2}}(\lambda)$ the quantum yield at 266 nm for the reaction $\mathrm{H_2O_2} + h\nu \longrightarrow 2\,\mathrm{OH}$, Δn_{OH} the difference between the hydroxyl densities with the photodissociation laser on and off and F the laser fluence.

However, as can be seen in figure 2.33, some cross sections are overlapping the photodissociation laser wavelength. Notable is the ozone cross section. This could cause trouble in plasmas that produce ozone and will be discussed in the results chapter where appropriate.

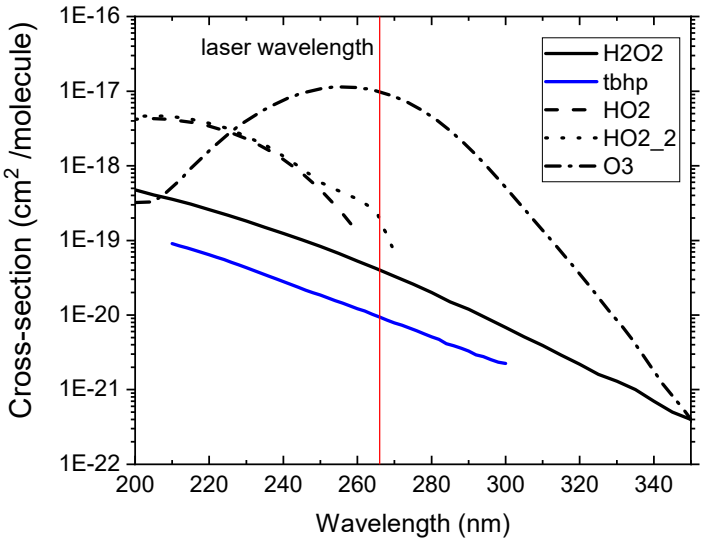

Figure 2.33: Crosssections at 298 K for all relevant species in the plasma effluent and the calibration substance *tert*-Butyl hydroperoxid. The vertical red line indicates the photofragmentation laser wavelength at 266 nm. Crosssections taken from [116].

2.8 Summary of diagnostic methods

To summarise the diagnostic methods used and provide an easy overview, following table lists all diagnostic methods, on what they were used, and where in the results chapter they can be found.

Diagnostic	Usage	Section
Power measurements	On COST jet and modified COST jet	3 4.2
Thermocouple	Effluent of the COST jet	3
Surface temperature	Surface temperature in front of COST jet	3
Rotational and vibrational temperature	Gas temperature derived from hydroxyl temperature in the plasma of the modified COST jet	4.4
Absorption spectroscopy	Hydroxyl density in the plasma and ozone density in the far effluent	3 4.2 4.3
OES	Line ratio measurements of he and oxygen lines in the COST jet plasma	3
FTIR	Hydrogen peroxide density in the far effluent	4.1
LIF	Hydroxyl density in the effluent of the COST jet and modified COST jet	4.3
PDLIF	Hydrogen peroxide density in the effluent of the COST jet and modified COST jet	4.1
TALIF	Atomic oxygen density in the effluent of the COST jet	3 4.5 5

Table 2.1: List of diagnostics and where they are used in this work

Chapter 3

Comparative Study of 'COST Reference Microplasma Jets'

The COST jet was introduced earlier in 2.1 as a reference jet. But it has not been tested, yet, if different builds of the jet produce the same output of, i.e. atomic oxygen, effluent temperature or perform similar in bacterial inactivation assays.

A reference plasma jet will make the comparisons of results across different labs easier. This should boost the understanding of chemistry, physics and biology and surface interactions.

This was done in this work by testing four of the COST jets for reproducibility in power characteristics, gas temperature and surface temperature, optical emission spectroscopy, ozone and atomic oxygen density as well as bacterial inactivation. For this, a gas admixture of 1 slm helium and 0.5 % oxygen was used.

The COST jets were provided by four different institutes listed in table 3.1. Their original jet names were kept in order to be able to trace them back to there origin.

Jet name	Origin
A	Leibniz Institute for Plama Science and Technology Greifswald
D	Technical University Eindhoven
E	Ruhr-University Bochum
G	Open University at Milton Keynes

Table 3.1: Labels and origin of the COST jets used in this study.

3.1 Protocol

Physical and chemical analysis

To compare the jets under stable operation a characterisation protocol was implemented.

This protocol was inspired by biological applications and to ensure repeatability.

For each jet, the same power supply, oscilloscope, spectrometer, ozone monitor and laser were used. The temperature and humidity of the labs were recorded. For this study, the conditions have been 22±0.5 °C and 50±10 % humidity throughout the experiments.

The gaslines were flushed for 30 min and after that the jets were warmed up by letting them run for 30 min before conducting any experiments. This ensured stable operating conditions of the gas supply and the jets and was done before each experiment. Additionally, it was waited for 10 min between each parameter change to ensure stable conditions during the measurement.

This protocol will also ensure that the results are comparable ,as long as the same equipment is being used, between different labs.

Bacterial inactivation assay

The bacterial inactivation assay was carried out as in [24]. *Eschericia coli* grown in Luria-Bertani (LB) broth were cultured until late logarithmic phase. Approximately 8×10^5 colony forming units (CFU) were plated onto LB-agar plates (containing 20 mL of LB plus 17.5 g/L agar). Pouring of plates were standardised as much as possible to ensure minimal differences between them that could have affected results. Following COST jet treatment, plates were incubated at 37 °C, then the area of inhibition (AOI) was measured the following day as the area where bacterial growth was inhibited. The AOI was measured, and surviving colonies counted using ImageJ software.

3.2 Results

3.2.1 Power characteristics

Figure 3.1a shows the results for the characteristic voltage power curve. The blue and red areas represent the standard deviation of the mean of all four jets for the cases of low to high voltage and high to low voltage sweep, respectively. As an example the characteristic of Jet G is shown (black dots).

The sweeps were done by increasing and, at the point of arcing, decreasing the output of the generator.

The relative deviation stays below 15 % above 190 V and increases fast above 300 V. Over 350 V the jets begin to arc. Stable operation for all of the jets is between 180 V and 350 V which corresponds to a power range of 0.18 W to 2.0 W.

The calibration factor can deviate up to 2.5 % while the reference phase deviation can affect the power up to 2 %. The deviation of the current sensing shunt resistor can be neglected because the deviation is too low to be noticeable. Analysis of these deviations show that this can lead to a power measurement error of 5 %, which will be assumed as an upper limit for the error for power measurements.

The 15 % deviation must come from somewhere other than only calibration factor and phase shift. Differences from the electrode distance and surface play a role, especially with regards to breakdown and arcing voltage. Two of the jets (A and E) were run for an unknown amount of time and show visible discolouration from arcing or high power operation on the electrode surface. Additionally, the inside of the glass appears white at the beginning of the plasma channels. This might have come from high power operations close to arcing.
In the following, the power will be used as the control parameter for all experiments.

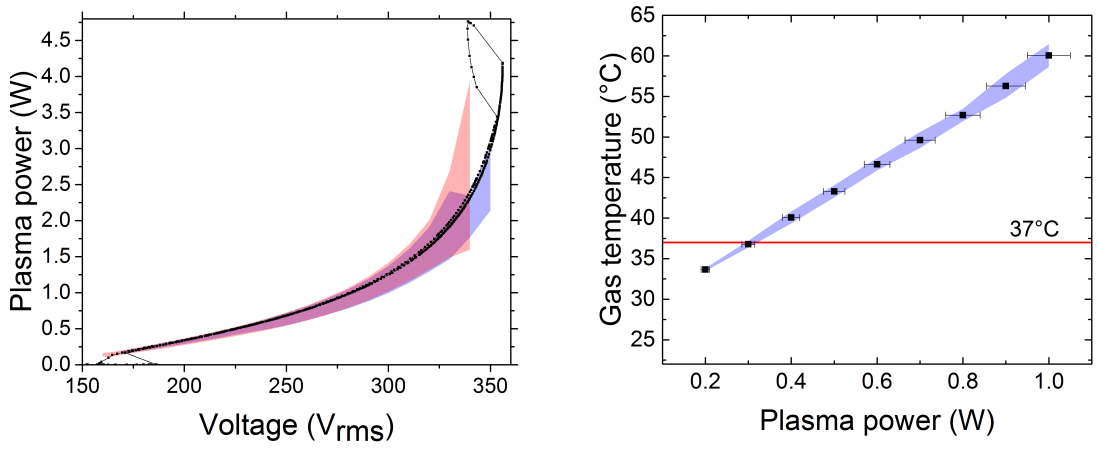

a) b)

Figure 3.1: Characteristic power voltage curve (a) and temperature power curve (b). The red line in (b) indicates the critical temperature for biological samples. In case of (a) the blue and red shaded area represent the standard deviation of all jets for low to high voltages and vice versa, respectively. Conditions: for 1 slm He, 5 sccm O_2

3.2.2 Gas temperature measurements

The gas temperature was measured with a thermocouple 3 mm away from the electrodes. More details can be found in 2.3. Figure 3.1b shows the results of the gas temperature measurements for all jets investigated in this study. It can be seen that the temperature deviation remains below 3 % over the whole range. The horizontal red line indicates a temperature of 37 °C which is the limit for treating biological samples.
As can be seen from graph 3.1b the power should be kept below 0.3 W to safely treat biological samples at 3 mm distance from the electrodes. The measurements were taken in free flow. This means that no obstacle is placed into the effluents stream other than the thermocouple that would obstruct and change the flow pattern. The temperatures may change due to geometrical factors in front of a surface. This was also investigated in this study and is shown in section 3.2.3.

3.2.3 Surface temperature measurements

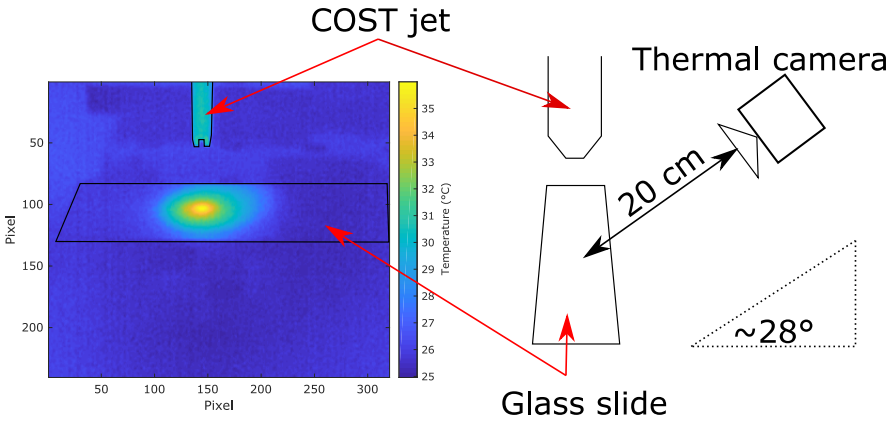

Figure 3.2: Thermal image of the plasma jet and sanded microscope slide. The long structure in the middle are the electrodes of the plasma jet. Right underneath the heat radiated from the sanded microscope slide can be seen. Conditions: 1 slm total helium flow, 0.5 % O_2, 0.3 W plasma power

The temperature of a surface is a vital parameter for sensitive or biological surfaces and can be different from the temperature in free flow presented in section 3.2.2 due to geometrical flow effects or evaporative cooling.

To measure the surface temperature, an inert glass surface was chosen. The surface is matte to minimize reflections from the surroundings. The temperature was recorded using a thermal camera as described in 2.3. The glass surface was chosen because wet samples are difficult to measure and less reproducible. Therefore, the glass surface comes with a caveat that does not necessarily represents measurements of wet surfaces, such as agar plates, because of the lack of evaporative cooling and different thermal conductivity and heat capacity.

Figure 3.2 shows an example thermal image captured by the thermal camera on the left and the schematic for this setup on the right. Figure 3.3a shows the average maximum surface temperature from all jets for a constant power of $0.3 \pm 5\,\%$ W and various distances from surface to electrodes. The blue shaded area is the standard deviation of the mean maximum surface temperature. Each measurement consists of 3 thermal images of the surface taken right after another. The distance shown is from the tip of the jet, not the electrodes.

It can be seen that the temperature decreases slowly with increasing distance. This is in agreement with [57] and supports that the effluent channel is stable over a distance of at least 3 cm as can be seen from Schlieren images taken by Kelly et al. [56].

The deviation of up to 1 °C between the jets is good taking into account that these measurements were taken with a thermal camera and not a thermocouple. 1 °C is considered "good" because it lies within the noise of this measurement method. Moreover, environmental influences take over with increasing distance from the surface. The temperature of the

first point at 3 mm is comparable to the thermocouple measurements with the same plasma power but 1 mm closer to the electrodes and free flow. This shows that free flow and surface temperature measurements for this parameter are in good agreement.
As the maximum temperature does not change much, the temperature profile may also not change. Figure 3.3b shows the averaged profiles of the jets at 3 mm and 30 mm. While the deviation between the jets is low at 3 mm the deviation is increased at 30 mm due to environmental factors and deviations in the jet mount. The mean area that is heated is approximately 25 mm in diameter for all distances. The only parameter that changes is the maximum temperature of the heat profile. The heat profile is also comparable to the one from [56].
This shows that thermocouple measurements in free flow are comparable to temperature measurements on a surface and the surface temperature does not change drastically with increasing distance. Additionally, all COST jets perform similar in terms of set power and temperature.

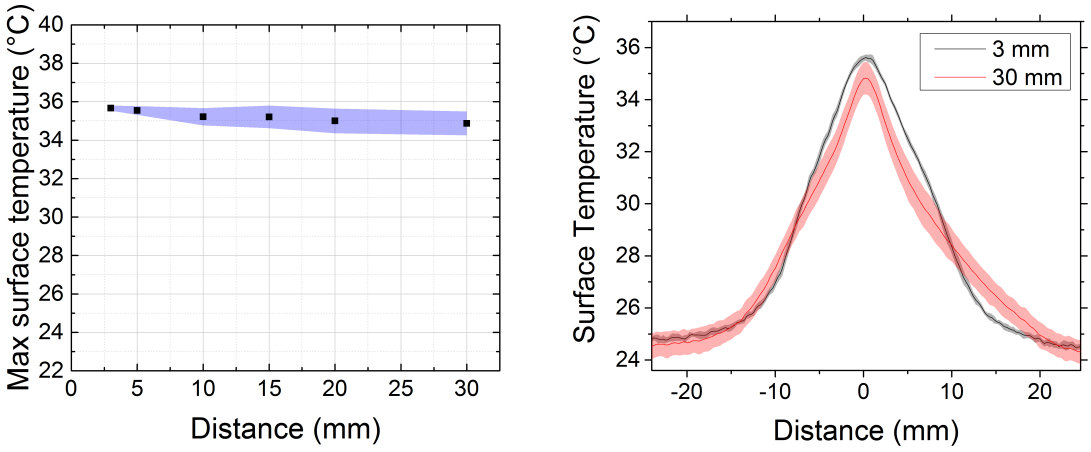

a) b)

Figure 3.3: Heat profiles for various distances (a) and maximum temperatures for each distance (b). All distances are measured from the tip of the jet. Conditions: 1 slm total helium flow, 0.5 % O_2, 0.3 W plasma power

3.2.4 Optical emission spectroscopy

Optical emission spectroscopy is a technical relatively simple way to see changes in plasma. OES was conducted using the COST jet OES cover. The cover ensures that all measurements are at the same position in the middle (lengthwise from the electrode) of the plasma within ±1 mm. A spacer ensures that the fibre is 3 mm away from the plasma in order to inhibit any interference of the metal part from the fibre to interact with the electric field. Otherwise the plasma could be altered.

Figure 3.4 shows the averaged intensity line ratios for the most prominent lines He 706 nm,

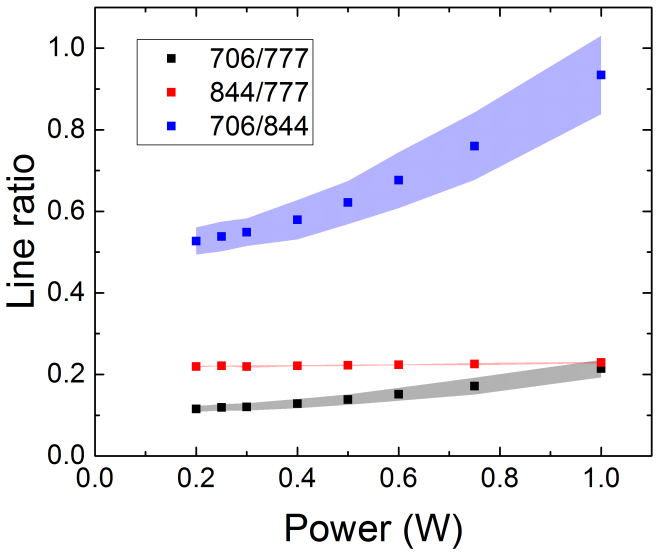

Figure 3.4: Line ratios from OES for different powers. Spectral lines: 706 nm (He), 777 nm (O) and 844 nm (O). Conditions: 1 slm total helium flow, 0.5 % O_2

O 777 nm and O 844 nm for all jets. The shaded areas represent the standard deviation of all jets. It can be seen that the oxygen line rations 844/777 stay the same over that range of powers tested.

The helium to oxygen line ratios 706/777 and 706/844 both increase with power suggesting that the helium transitions, the observed line is actually a triplet, are favoured by a raising electron temperature.

The deviations for 844/777 line ratio is about 1 %, for 706/777 8 % and for 706/844 ca. 8 % percentage. The spectra for each jet and power setting are ten times averaged. This leads to a deviation of less then 2 %. Therefore, the high deviation of 8 % for the helium/oxygen line ratios may come from different aged electrodes. The power deviation is standard 5 %. Atomic oxygen is created via electron impact dissociation [44,137]. This process is dependent on the EEDF which increases non-linearly with power and therefore higher variation might be expected.

A deviation of approximately 8 % for all jets is nonetheless a good agreement which indicates that the plasmas are very similar and the deviations are close to noise of the measurement method.

3.2.5 Ozone density

The ozone density was measured using a glass funnel attached to a commercial ozone monitor. The monitor sucked in the effluent of the COST jet and analysed it by absorption spectroscopy. More details on the setup can be found in 2.4. Figure 3.5 shows the ozone

densities for various power settings for 1 slm helium and 5 sccm oxygen. The shaded area represents the standard deviation of the mean of all jets. The ozone densities increases with increasing power. This can be explained by the larger production of atomic oxygen. The results for 0.5 W are in good agreement with measurements in the far effluent [58]. The densities closer to the jet will be smaller as can be seen in [58].

The deviation between the jets is maximal 3 % and, therefore, excellent because the deviation is barely higher than the noise of the measurement method.

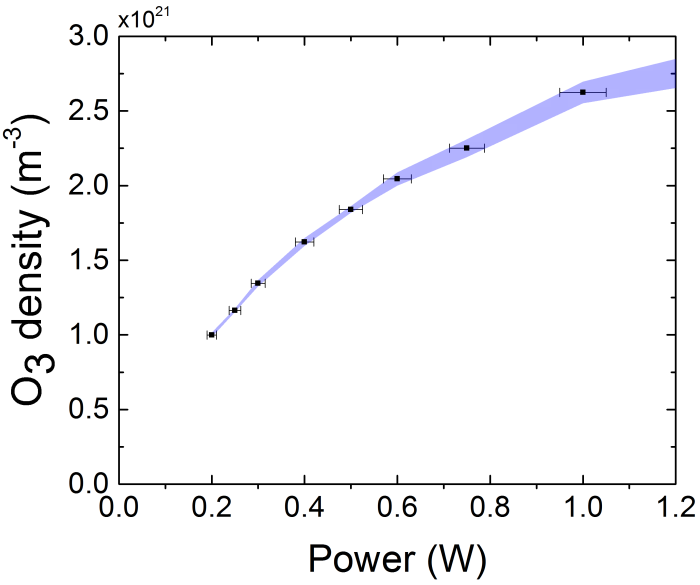

Figure 3.5: Ozone densities of all jets in the effluent of the plasma at various powers. Conditions: 1 slm total helium flow, 0.5 % O_2.

3.2.6 Atomic oxygen densities

Atomic oxygen densities were measured using TALIF for different powers. The measuring point is 1 mm away from the electrodes. The lifetimes were measured by a ps laser and the oxygen densities using a ns laser. The laser setups are described in 2.7 Figure 3.6 shows the averaged results of atomic oxygen measurements of all of the jets for various powers and 1 slm helium and 5 sccm oxygen. The shaded area represents the standard deviation of all jets.

It can be observed that the atomic oxygen densities rise with power. The deviation of the four jets is 8 % below 0.5 W and 13 % above 0.5 W. The measured lifetimes of excited atomic oxygen are 4.24 ns $\pm$ 1.6 %. These deviations also represent the repeatability within these measurements. Compared to [138], who used comparable conditions, the results are in agreement with the results from molecular mass beam spectrometry. This sort of spectroscopy is less direct than TALIF with the biggest challenge to overcome the pressure difference be-

tween atmospheric pressure and the vacuum the device needs to operate. This is described in detail in Große-Kreul et al. [62]. The overall systematic error of the TALIF measurements is higher due to uncertainties in the cross section of atomic oxygen but we only want to discuss the deviations between jets and the laser was the same for every jet.
Overall a maximum deviation of 13 % is very good for the COST jets because it is only slightly higher than the noise of the measurement method.

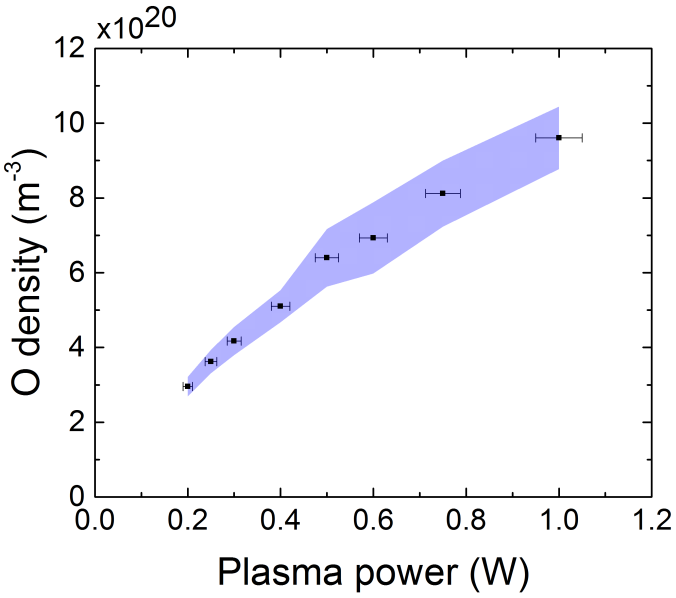

Figure 3.6: Absolute atomic oxygen densities as measured using TALIF at various powers. Conditions: 1 slm total helium flow, 0.5 % O_2.

3.2.7 Bacteria inactivation

Surface decontamination is an important biological application of LTPs, and due to their low temperature, surfaces can include biological tissues such as the skin. With this in mind, the ability of the COST jets to be able to kill bacteria was investigated, with particular interest in their comparability. For this, the non-pathogenic *E. coli* MG1655 strain was plated onto LB agar plates and subjected to treatment with the COST jets. The treatment effects were quantified in two ways, firstly, the area of inhibition (AOI) was measured, and secondly, surviving colonies were counted to calculate the log reduction of bacteria in the AOI. Experiments were repeated in triplicate for each jet, and the mean and standard deviation calculated.

The experimental process was to allow the jet to warm up for 30 minutes, carry out treatments, then repeat the process for another jet. As this was a fairly lengthy process, treatments with the first jet were then repeated to check that the bacteria had not changed over time due to being left in culture for longer on the bench. These checks showed that there

was no difference in the AOI or log reduction in bacteria between the first time the jet was used for treatments, and the second time approximately an hour later (data not shown). The chosen treatment time was 2 minutes as this was long enough to give a consistent sized AOI, without making the treatment process too long ,meaning bacteria was not left out for too long.

The treatments were carried out in a perspex box to reduce any effects of air flows in the laboratory. An extractor fan was used to prevent build-up of species in the box during treatments. Nitric oxide (NO) and ozone (O_3) levels were checked using monitors and were shown to not increase appreciably over the treatment time, therefore, showing that there was no build-up of these species causing bacterial killing.

Representative images of treated and control plates are shown in figure 3.7. In the top panel, one treated plate for each jet is shown, while gas-only and untreated control plates are shown. Treatment with each of the 4 jets gives circular AOI, with the different positions of the AOI resulting from the plate not being placed exactly centrally under the jet. Gas-only treatment controls and untreated controls were also included, to check that any killing effects were due to the plasma, and not just the gas flow. As shown by the control plates (figure 3.7, bottom panel), no killing was achieved by gas flow alone.

As shown in figure 3.8, the AOI (red points and axis) for each of the jets was very similar, with means ranging from 5.3 - 5.7 cm^2. The log reduction in bacteria due to treatment with each jet also appears to be consistent across all the jets (blue points and axis), showing approximately 2.5 - 3 log reduction by each jet. There is some variation between jets, however, this variation is generally smaller than the variation seen within each jet. In general, the 4 jets all seem to have similar abilities to kill our *E. coli* model bacteria.

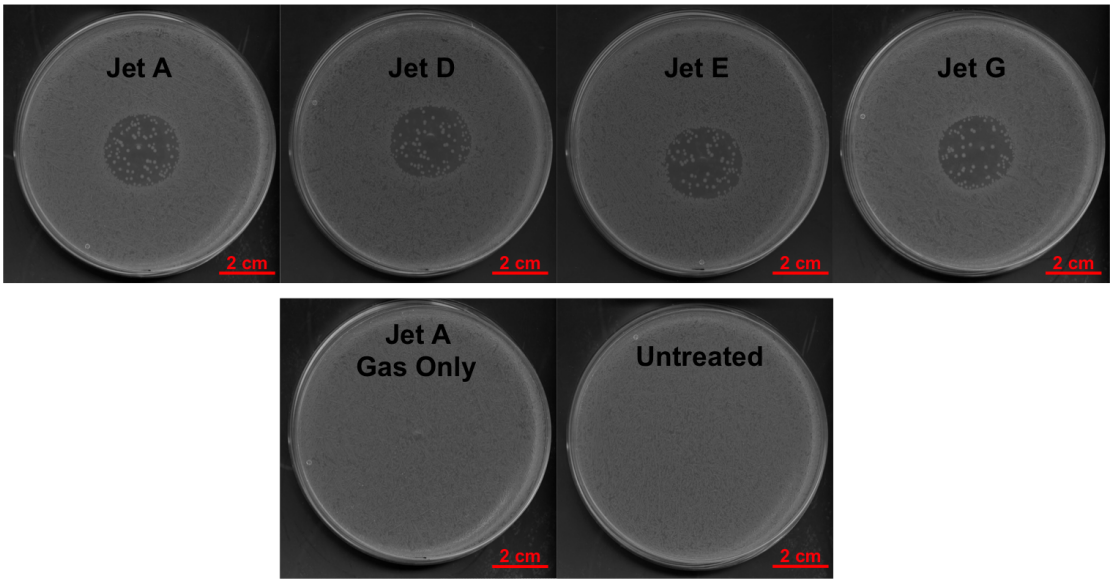

Figure 3.7: Representative images of bacterial plates treated by COST jets. 100 μL of *E. coli* MG1655 at approximately 8 x 10^6 cfu/mL were plated onto LB agar plates and exposed to a 2 minute treatment by COST jet. The plasma power was kept at 0.3 W, and the feed gas was 1 slm helium with 0.5 % oxygen admixture. The top panel shows a representative plate for each jet, plates following 2 minute COST jet treatment and overnight incubation. Representative control plates are shown in the bottom panel. The gas-only control was also treated for 2 minutes but the plasma power was turned off (therefore only the helium/oxygen gas was incident on the sample), and the untreated control was plated identically to all the other treatment plates, but did not receive a COST jet treatment. For each jet, treatments were carried out in triplicate.

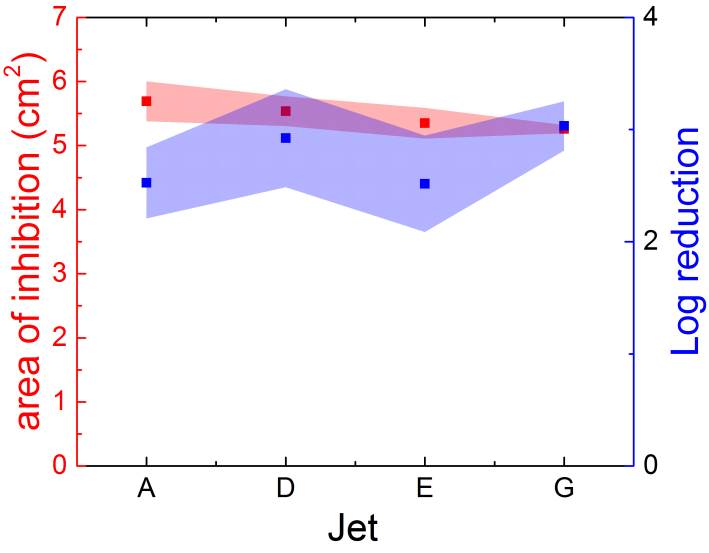

Figure 3.8: Figure showing area of inhibition (AOI) and bacterial log reduction following treatment with the different COST jets. The red points show the average AOI induced by each jet, with the error bars showing the standard deviation. The blue points show the mean log reduction in *E. coli* MG1655 colony forming units (cfu) following treatment with each jet, with the error bars showing standard deviation. For each jet, treatments were carried out in triplicate. Conditions were as stated in figure 3.7.

3.3 Summary and conclusions

It was shown that the deviation between the COST Reference Microplasma Jets is 15 % for the voltage to power characteristic, under 3 % for gas temperature in the effluent, ∼3 % for surface temperature, 3 % for ozone, 8-13 % and in case of atomic oxygen 8 % - 13,%. Most of the deviations are a mixture of experimental precision and deviations of the jets whereas the experimental deviations are as minimised as possible to below ∼8 % for atomic oxygen densities and under 2 -3 % for the rest of the measurements. The bacterial inactivation assay shows that the biological effect of the jets is the same within error bars.

As described in [36] the source is simple, inexpensive and robust. The weak point of the source however is the built in voltage probe which has to be calibrated. But this is also the case for a potential upgrade of the jets described in [106]. It is possible to calibrate one jet with very high precision and then derive the voltage calibration factors for the other jets by fitting the voltage-power characteristic. This makes it very easy for other labs to obtain a calibration factor.
Overall, the jets show very good agreement which make them suitable to act as a reference source for different labs.

Chapter 4

Reactive species production in the plasma with water and oxygen admixture

In the previous chapter, it was established that the COST jet is a viable reference source for fundamental plasma jet science.

Previous studies show that the plasma effluent extends up to 5 cm after the nozzle [56]. Knake et al. [57] reported that the atomic oxygen production is most efficient with an admixture of 0.5 % to 0.6 % molecular oxygen. Ellerweg et al. [58] reported an atomic oxygen density of $8 \cdot 10^{20}\, m^{-3}$ and an ozone density of $2 \cdot 10^{20}\, m^{-3}$, depending on operation conditions. Measurable quantities of atomic oxygen extend up to 30 mm from the nozzle. Using water admixtures, added to the discharge, hydroxyl and hydrogen peroxide can be produced. While the OH density reported by [1] is around $5 \cdot 10^{20}\, m^{-3}$ inside the plasma, it declines quickly down to $2 \cdot 10^{20}\, m^{-3}$ and lower outside the plasma but is still measurable by CRDS and MBMS in up to 20 mm distance to the active plasma in a helium atmosphere [59]. Willems et al. recently used MBMS to study hydrogen peroxide and hydroxyl in the effluent of the COST jet [139]. This study noted that hydrogen peroxide and hydroxyl densities are the same (approximately $2 \cdot 10^{14}\, cm^{-3}$) at 3 mm distance from the jet and 7980 ppm water admixture. By increasing the distance from the jet, hydroxyl decays and is measurable up until 20 mm. Hydrogen peroxide decreases linearly to a fourth of its starting value. Studies concerning reactive species densities inside the plasma have also been done. These examined at atomic oxygen and hydroxyl [1], ozone [37] and helium metastable [70, 71].

Some of the above mentioned studies have already shown how the hydrogen peroxide or hydroxyl densities change with water admixture and distance. However, these studies are based on MBMS or CRDS and were conducted in helium atmosphere. Especially MBMS, being a non-direct method to detect reactive species and the spatial resolution is limited.

Furthermore, this can change the flow dynamics of the effluent because MS only works in near vacuum. It was not shown how the reactive species, such as hydrogen peroxide and hydroxyl in the effluent behave in air. This is usually the use case in biomedical applications. It was also not shown how hydrogen peroxide, ozone, hydroxyl and atomic oxygen densities can be tailored by additional admixtures of oxygen to water containing plasmas.

In this chapter, the hydrogen peroxide densities in the effluent were measured by Fourier transform infrared spectroscopy (FTIR) and photodissociation laser induced fluorescence (PDLIF) and are presented in section 4.1. PDLIF is new to the field of APPJs and it has to be proven how viable it is. After which, ozone concentrations measured in the effluent by an ozone monitor in section 4.2 are discussed, followed by results from absorption spectroscopy focusing on hydroxyl in section 4.3. The gas temperature inside the plasma with water and oxygen admixtures are addressed in section 4.4. The atomic oxygen densities in the effluent measured by TALIF from water and oxygen variations are depicted in section 4.5.

4.1 Hydrogen peroxide concentrations

Hydrogen peroxide is a long-lived reactive species with the ability to travel over long distances outside the plasma [140]. This can easily diffuse from the gas into the liquid phase because of its high Henry's constant. This makes it interesting for biological applications. Active biological tissue is usually surrounded by water in order to function correctly. The hydrogen peroxide dissolved in the water can reach the cells and react with, or permeate through, the lipid membrane. In high concentrations, hydrogen peroxide is toxic and can trigger cell death mechanisms [45].

Because of these properties, it is vital to measure the amount of hydrogen peroxide produced by the plasma and find ways to control the production in the plasma and, possibly, the effluent.

The hydrogen peroxide concentrations in this chapter were measured with FTIR and PDLIF as described in sections 2.6 and 2.7, respectively.

Water variation

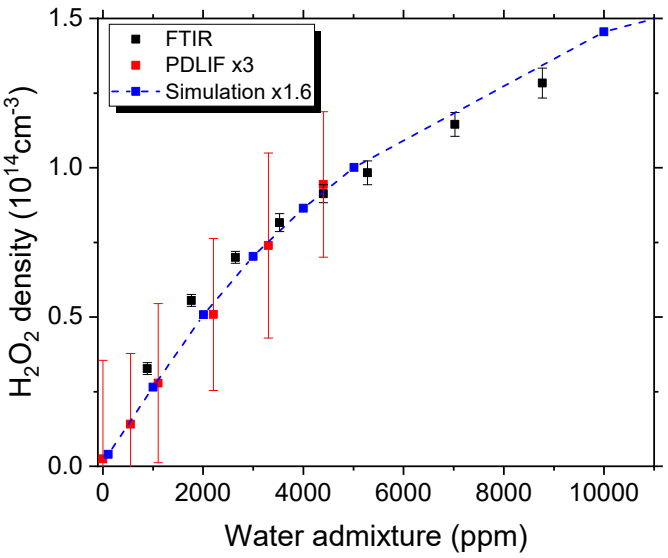

Figure 4.1: Hydrogen peroxide densities versus water admixture performed with the modified COST jet. Shown are results from FTIR, PDLIF and a simulation from [141]. Conditions: 5 slm helium flow, 178 V_{RMS}, 0 ppm to 10000 ppm water admixture.

Figure 4.1 depicts the hydrogen peroxide densities from a water variation performed with the modified COST jet measured with FTIR (black) and PDLIF (red). The conditions were a total helium flow of 5 slm and the voltage was maintained at 178 V_{RMS}. The water admixture ranges from 0 ppm to 4400 ppm in the case of the PDLIF measurements and up to 9000 ppm for the FTIR measurements. For both FTIR and PDLIF, the measurement point is 80 cm after the plasma. The effluent was contained in a tube until the measurement point, as was explained in 2.6. In the case of the PDLIF, measurements were taken 4 mm after the tube outlet in open air. This prevented clipping of the photodissociation laser (see 2.7). The FTIR measurements were taken inside a long path absorption cell with 5 m absorption path. The cell was heated to 30 °C to prevent condensation of water on the walls and to have a known gas temperature.

It can be noted that with increasing water admixture the hydrogen peroxide densities increased in both measurements. The PDLIF measurements were consistently three times lower than the FTIR measurements because of difficulties measuring low hydroxyl concentrations. The same can be observed for the standard deviation of the measurements. While the error bar of the FTIR densities remained consistently below 10 %, the PDLIF standard deviation is higher than 10 %. This can be attributed to the energy deviation of the LIF laser and the multiple factors that play a role for this measurement, which include the absorption cross section of *tert*-Butyl hydroperoxid, reaction coefficient of reaction 2.24, and

the absorption cross section of hydrogen peroxide. Another challenge was the noise in the measurements. This made fitting lifetimes at low hydroxyl densities difficult. This will be discussed further in section 4.3. Additionally, ozone could contribute towards a skewed signal because the ozone absorption cross section has its maximum around the photodissociation laser (266 nm). However, this can be rejected for the water variation because no ozone could be detected by ozone measurements, in this case.

The FTIR measurements were considered more accurate because they largely depend on the well known absorption cross sections of hydrogen peroxide as opposed to a chain of factors, including the hydroxyl calibration.

When compared to global model simulations from [141] for the same plasma, the hydrogen peroxide densities follow the same trend but do not agree in terms of absolute numbers. This can be attributed to large uncertainties regarding the hydrogen peroxide electron dissociation cross sections, as well as other cross sections, and reaction rates used in the simulation. This was discussed in Turner [142] for an oxygen containing helium plasma for the COST jet.

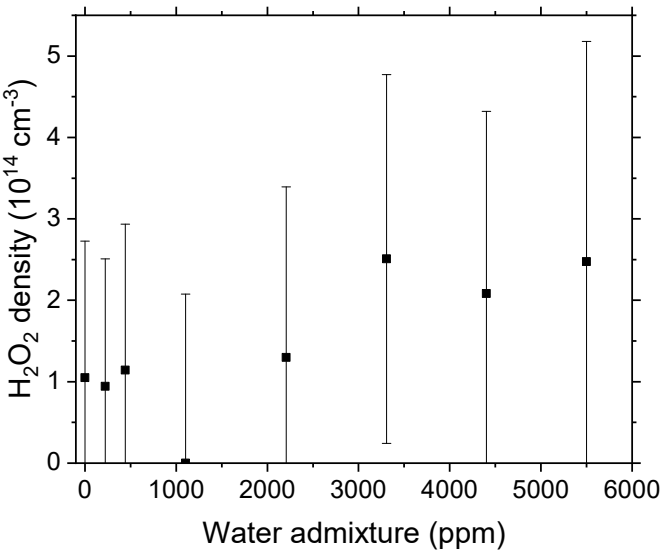

Figure 4.2: Hydrogen peroxide densities versus water admixture using the COST jet measured by PDLIF. The measurement point is 9 mm from the electrodes. Conditions: 500 sccm helium flow, 0 ppm to 5500 ppm water admixture, 178 V_{RMS}.

The above mentioned studies [141, 142] were all done with the modified COST jet. The COST jet should yield similar results. This was tested and the results are shown in **??**. These results were not included in figure 4.1 as they will be discussed later.

Figure 4.2 depicts the hydrogen peroxide densities versus water admixture measured with PDLIF for the COST jet.

The hydrogen peroxide densities start at $1 \cdot 10^{14}$ cm^{-3} and increased with water admixture to

$2.5 \cdot 10^{14}$ cm^{-3}. One exemption was found in 1100 ppm water admixture. These densities were approximately ten times higher than from the aforementioned studies. The high error bars pointed out that the difference in hydroxyl densities were small and could not overcome the deviation in laser energy from the probe laser. For this experiment, a more stable hydroxyl probe laser would have been beneficial.

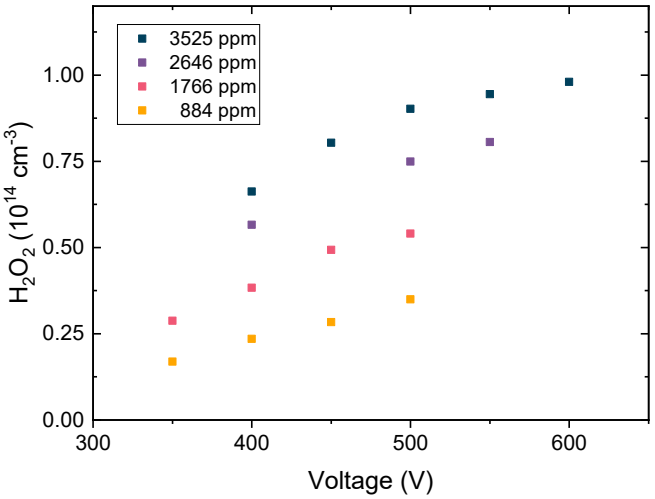

Figure 4.3: Hydrogen peroxide densities versus water admixture and applied voltage with the modified COST jet. Conditions: 5 slm total helium flow, 884 ppm to 3525 ppm and 124 V_{RMS} to 212 V_{RMS}

Figure 4.3 depicts the hydrogen peroxide densities versus voltage and water admixture for the modified COST jet measured with FTIR and the previously described conditions. The total helium flow was 5 slm. For water admixtures below 1800 ppm, the plasma can be operated from 124 V_{RMS} to 177 V_{RMS}. For water admixtures above 1800 ppm, the plasma can be operated from 141 V_{RMS} up to 212 V_{RMS}. For clarity, the error bars were omitted. The error was tested for several conditions during the measurement campaign on different days and the maximum error was estimated to be 5 %.

The hydrogen peroxide concentration rose with increasing water admixture and increasing voltage. The increase in hydrogen peroxide with voltage can be attributed to higher electron dissociation of water. The increase with water admixture is attributed to the increased availability of water to dissociate. This leads to an increase in hydrogen peroxide via following reaction with M as a generic third species:

$$OH + OH + M \longrightarrow H_2O_2 + M. \tag{4.1}$$

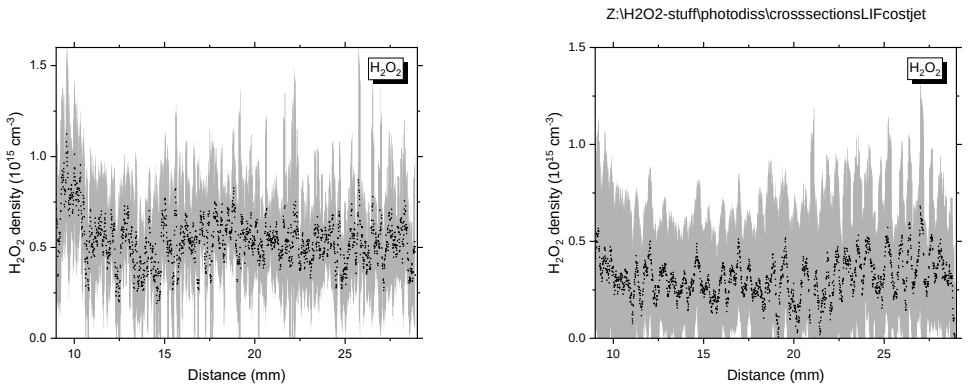

a) 500 sccm b) 1000 sccm

Figure 4.4: Hydrogen peroxide densities as a function of the distance from COST jet nozzle measured by PDLIF. The raw data is eleven point averaged (black) and the grey area represents the standard deviation from the average. Conditions: 500 sccm (a) and 1000 sccm (b) total helium flow, 4400 ppm water admixture, 178 V_{RMS}.

Distance variation

Figure 4.4 depicts the hydrogen peroxide densities as a function of distance from the COST jet. The plasma parameters were 500 sccm (a) and 1000 sccm (b) total helium flow, 4400 ppm water admixture and the voltage is 178 V_{RMS}. The distance was varied from 9 mm to 29 mm, from the tip of the COST jet, by moving the jet with a velocity $v = 0.5\,mm\,s^{-1}$. The measurements were taken with a frequency of 10 Hz. Therefore, a measurement was taken every 0.05 mm. The data was 21 point averaged and the grey area represents the standard deviation from this average.

For 500 sccm, the hydrogen peroxide densities remain constant at $0.5 \pm 0.3 \cdot 10^{15}\,cm^{-3}$ over the varied distance. A slight increase to $0.8 \pm 0.4 \cdot 10^{15}\,cm^{-3}$ between 9 mm and 11 mm can be observed, but is still within the error bars.

For 1000 sccm, the densities are $0.3 \pm 0.4 \cdot 10^{15}\,cm^{-3}$ over the varied distance. The relative standard deviation on average is 130 %. This is higher than the relative standard deviation of 500 sccm. This can be attributed to the higher gas flow which might introduce more fluctuations. As will be discussed later, the hydroxyl densities from the plasma and laser generated hydroxyl lie closer together. This causes the hydrogen peroxide densities to be less accurate. Overall, the hydrogen peroxide densities are more or less constant and long lived.

4.1.1 Oxygen admixture

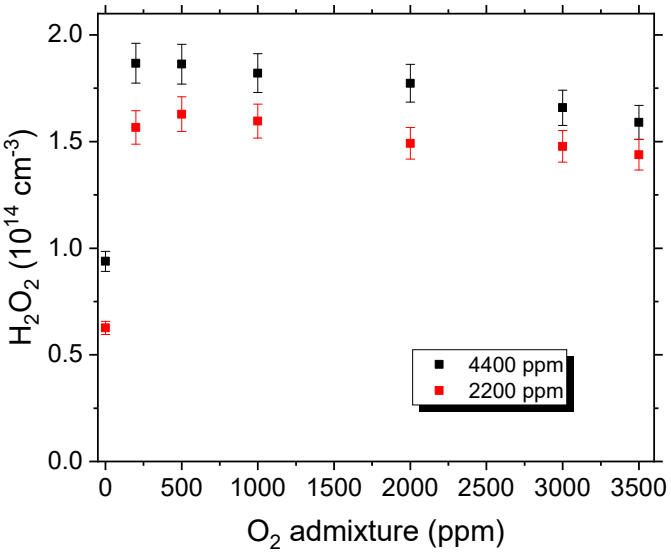

Figure 4.5: Hydrogen peroxide densities versus oxygen admixture measured with FTIR. Conditions: 5 slm total helium flow, 4400 ppm (black) and 2200 ppm (red) water admixture, 178 V_{RMS}, modified COST jet.

Figure 4.5 depicts the hydrogen peroxide densities measured with FTIR for the oxygen variation with a fixed water admixture of 4400 ppm (black) and 2200 ppm (red). The conditions were 5 slm total helium flow and 178 V_{RMS}. For 2200 ppm water admixture, the 0 ppm oxygen admixture was derived from figure 4.1 by interpolation.

By admixing 400 ppm of oxygen to a water admixture of 4400 ppm, the hydrogen peroxide densities increased nearly two fold from $9.4 \pm 0.5 \cdot 10^{13}$ cm^{-3} to $1.9 \pm 0.1 \cdot 10^{14}$ cm^{-3}. With an admixture of more than 2000 ppm oxygen the hydrogen peroxides densities declined slowly to $1.59 \pm 0.08 \cdot 10^{14}$ cm^{-3}. The standard deviation was estimated to be a maximum of 5 % based on several points tested on different days. For 2200 ppm water admixture, the 0 ppm oxygen admixture was derived from figure 4.3.

The trend for the hydrogen peroxide densities was the same for 4400 ppm and 2200 ppm water admixture. But the densities are approximately 40 % lower. The addition of oxygen usually produces ozone in dry plasmas. However, no ozone was detected by the FTIR measurements but from the ozone monitor, as will be discussed later. The reason for this is due to the higher cross sections of ozone in the UV than infrared wavelength regime.

The main pathway in wet plasmas to build hydrogen peroxide is the reaction

$$OH + OH + He \longrightarrow H_2O_2 + He. \tag{4.2}$$

This led to the question regarding if the addition of oxygen produces more hydroxyl or do other reaction pathways become more important. For example, reaction pathways involving atomic oxygen, ozone or hydroperoxyl. Oxygen molecules are usually dissociated by electrons in the plasma and react easily with water to produce hydroxyl. Atomic oxygen could form ozone which will then be dissociated by electrons or UV-photons. This leads to singlet delta oxygen, which also reacts quickly with water to form hydroxyl.

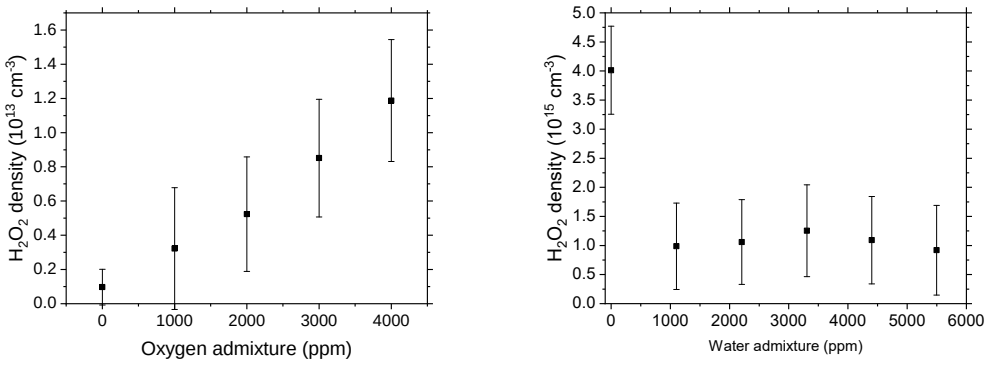

a) b)

Figure 4.6: Hydrogen peroxide densities as a function of a) oxygen admixture and b) water admixture measured with PDLIF. Conditions: 500 sccm total helium flow ,(a) 4400 ppm oxygen admixture (b) total helium flow, 4400 ppm water admixture, 178 V_{RMS}, COST jet.

Figure 4.6a depicts the hydrogen peroxide densities versus the oxygen admixture. The measurement point was 9 mm from the electrodes. The plasma conditions were, 500 sccm total helium flow, 4400 ppm water admixture and 178 V_{RMS}.

The hydrogen peroxide concentrations increase steadily from $2 \pm 2 \cdot 10^{14}\,cm^{-3}$ at 0 ppm oxygen admixture up to $2.5 \pm 0.8 \cdot 10^{15}\,cm^{-3}$ at 4400 ppm oxygen admixture.

This is contrary to figure 4.5, in which the densities first double with oxygen admixture and then slowly decline by adding more oxygen. The observed trend might be caused by ozone being photodissociated by the PDL, which leads to a higher atomic oxygen density by following reaction [115]:

$$O_3 + 266\text{ nm} \longrightarrow O(^1D) + O_2(^1\Sigma_g{}^+) \tag{4.3}$$

The atomic oxygen reacted with water to form hydroxyl (approximately 10 ns). This was previously seen in [115, 143, 144]. This reaction is fast ($2.01 \cdot 10^{-10}\,cm^3$ molecule $^{-1}s^{-1}$ [145]) compared to other reactions in the effluent. This is likely to dominate the atomic oxygen destruction. Due to the abundance of water, the decay rate of atomic oxygen can be approximated to $4.5 \cdot 10^{-5}\,s^{-1}$ in these conditions. The time between the PDL and the hydroxyl probe laser was 1 µs and, thus, the atomic oxygen lifetime and the time between lasers is

similar. The dissociation of ozone interferes with the hydroxyl measurements and does not allow for the measurement of the hydrogen peroxide densities, in this case.

Figure 4.6b depicts the hydrogen peroxide densities versus the water admixture. The conditions were only different for the constant 1000 ppm oxygen admixture.

The hydrogen peroxide density without oxygen admixture is $4.0 \pm 0.8 \cdot 10^{15}\,\mathrm{cm}^{-3}$. After admixing water, the density decreases to $10 \pm 7 \cdot 10^{14}\,\mathrm{cm}^{-3}$. Increasing the water admixture further does not lead to a significant change in hydrogen peroxide density. The high density at the beginning can be attributed to the ozone photodissociation by the PDL. The hydroxyl was produced by residue water from the inside of tubes and flowing into the effluent. With higher water admixtures, the ozone concentrations decreases (see figure 4.7) and the ozone interference decreases. All error bars are approximately $7.5 \cdot 10^{14}\,\mathrm{cm}^{-3}$ and do not change with higher hydrogen peroxide values. This can be attributed to the laser energy variation.

4.2 Ozone measurements

Ozone is another long lived species that is biologically active. It is used as a disinfection agent for water purification and decontamination [146,147]. Furthermore, it has been shown that the inactivation of *E. coli* is correlated to the concentration of ozone [46]. The formation and destruction of ozone in helium oxygen plasmas has been described before in [37, 148]. However, it has not been shown how ozone behaves in water containing plasmas.

The ozone densities were measured by using an ozone monitor attached to the modified COST jet as described in 2.4. The ozone monitor was in the same position after the plasma as the long path absorption cell used for the FTIR (80 cm) measurements. This ensured that the measurements were compatible with each other.

Measuring the ozone densities versus the water concentration with 5 slm helium flow, 4400 ppm water admixture, and $178\,\mathrm{V_{RMS}}$ revealed that no detectable ozone was produced. The detection limit of the ozone monitor was 2 ppb corresponding to a number density of $5 \cdot 10^{10}\,\mathrm{cm}^{-3}$.

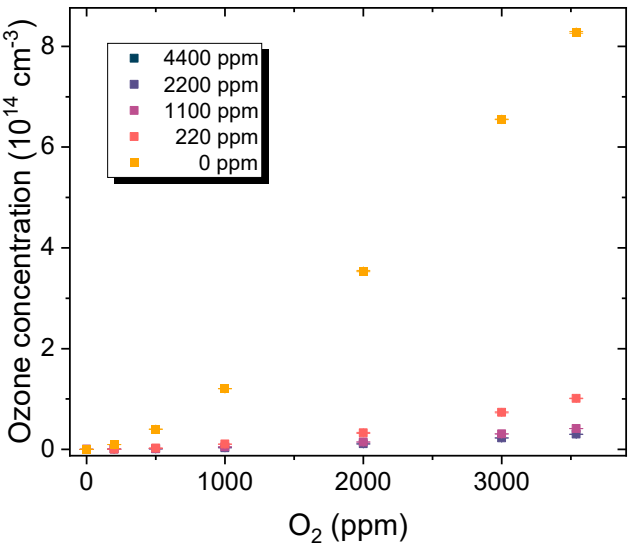

Figure 4.7: Ozone densities versus oxygen admixture for different water admixtures measured with ozone monitor in the far effluent. Conditions: 5 slm total helium flow, 0 ppm to 4400 ppm water admixture and 0 ppm to 3500 ppm oxygen admixture., 178 V_{RMS}, modified COST jet.

Admixing oxygen to the water containing plasma produced ozone. Figure 4.7 depicts ozone densities versus oxygen admixture for water admixtures which range from 0 ppm to 4400 ppm for the modified COST jet. The oxygen concentration was varied from 0 ppm to 3500 ppm. The total helium flow was 5 slm and the voltage kept constant at 178 V_{RMS}. Increasing oxygen admixtures resulted in higher ozone production, while increasing water admixture decreased the ozone concentration. The ozone production trend with increasing oxygen admixture was the same for higher water admixtures, as well as, without water admixture. The only difference being the dampened nature of the curves.

The efficiency of the ozone generation ranged from 0.19 % to 0.93 % for a dry plasma and drops to 0.03 % and below for 4400 ppm water admixture.

It was noticeable that the ozone concentration in the effluent does not increase linearly with the oxygen admixture as seen for other types of jets [149] measured with molecular mass beam spectrometry and argon.

The ozone production measured in the effluent without water showed the same trend as seen in [37] with a similar plasma. While it was expected that the water admixture dampens the ozone production, it was not expected that it continued to follow the same trend. This indicates that the oxygen and water chemistry are only coupled via a few reactions, which can potentially be determined by measurements of hydroxyl and atomic oxygen.

The main destruction pathways for ozone are tabulated in table 4.1. Only the fastest reactions were selected because these were more likely to play a role on short timescales.

Reaction	Rate	Reference
$O_3 + O \longrightarrow O_2 + O_2$	$7.96 \cdot 10^{-15}\ \frac{cm^3}{s}$	[115]
$O(1D) + O_3 \longrightarrow O_2 + O_2$	$1.20 \cdot 10^{-10}\ \frac{cm^3}{s}$	[150]
$O_3 + H \longrightarrow OH + O_2$	$2.89 \cdot 10^{-11}\ \frac{cm^3}{s}$	[150]

Table 4.1: Main destruction mechanism of ozone in the plasma the effluent.

This table 4.1 shows that mainly atomic species or, with faster reaction rates, excited atomic species such as atomic oxygen or hydrogen, play a major role due to the fast reaction rates.

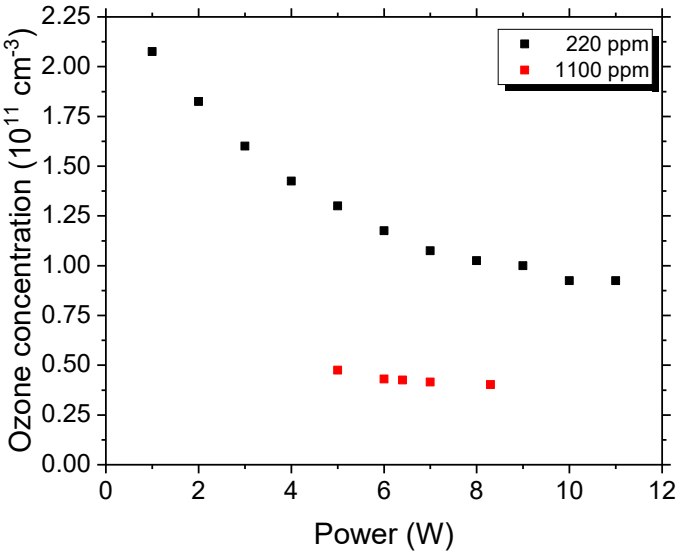

Figure 4.8: Ozone densities versus power variation and a fixed oxygen admixture for two different water admixtures measured with ozone monitor in the far effluent. Conditions: 5 slm total helium flow, 1100 ppm and 220 ppm water admixture, 3000 ppm oxygen admixture, modified COST jet.

Figure 4.8 depicts the power variation for the modified COST jet with the same oxygen admixture but with two different water admixtures. The overall trend for both cases is a decrease of ozone density with increasing plasma power. It shows that for powers between 5 W and 9 W, the deviation of the ozone density is below 30 %, for 221 ppm water admixture. For a water admixtures of 1100 ppm, the ozone density variation is below 10 %. This implies that the plasma power does not heavily impact the chemistry in plasmas with high molecular admixtures around 5 W to 9 W plasma power. The same negative ozone density trend can be observed in Wijaikhum et al. [37] with higher oxygen admixtures measured inside the plasma. The author also references that the influence of plasma power on the ozone concentration decreased, which is similar to figure 4.8.

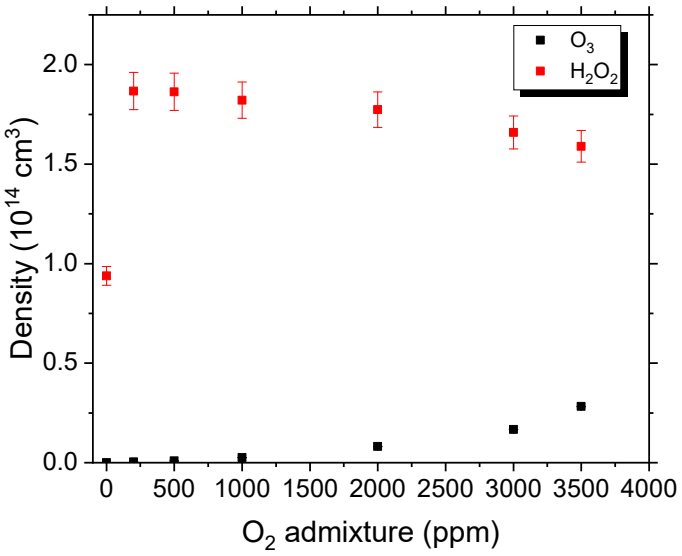

Figure 4.9: Ozone and Hydrogen peroxide density versus oxygen admixture versus oxygen admixture for water containing plasma measured with ozone monitor (ozone) and FTIR (hydrogen peroxide). Conditions: 5 slm total helium flow, 4400 ppm water admixture, 178 V_{RMS}, modified COST jet.

Figure 4.9 shows the ozone (black) and hydrogen peroxide densities (red) versus the oxygen admixture with a fixed water content of 4400 ppm. The oxygen was varied from 0 ppm to 3500 ppm. The total helium flow was 5 slm and the voltage is kept constant at 178 V_{RMS}.

The trends of ozone and hydrogen peroxide have been described above. However, the production of hydrogen peroxide doubled with more than 400 ppm and then maintains at the same level, while the ozone concentration rose with increasing oxygen admixture.

The ozone measurements indicate that no ozone can be measured in the effluent of a water containing plasma. Once oxygen is admixed, the ozone production decreases fast and the highest measured ozone production efficiency decreased from 0.93 % to under 0.2 %. The power had less influence on the ozone production with increasing water content. The main result was that oxygen admixture, to a water containing plasma, increased the hydrogen peroxide production, but the ozone production was not tightly coupled to the hydrogen peroxide production.

4.3 Hydroxyl densities

Hydroxyl is a short-lived radical (approximately 0.1 s in the atmosphere [151, 152]). It is not as long-lived as hydrogen peroxide, but highly reactive and water soluble. Furthermore, hydroxyl is a precursor for hydrogen peroxide. This makes it useful for biomedical applications.

Hydroxyl was measured in the plasma by means of absorption spectroscopy and outside the plasma by means of LIF. Both methods are active, but differ in sensitivity, with LIF being the more sensitive method.

This section starts with hydroxyl density LIF measurements on the COST and modified COST jet. Furthermore, the effluent of the COST jet is characterised below 9 mm.

This section starts with LIF measurements, as described in section 2.7, and then compares these to absorption measurements, as described in section 2.4.

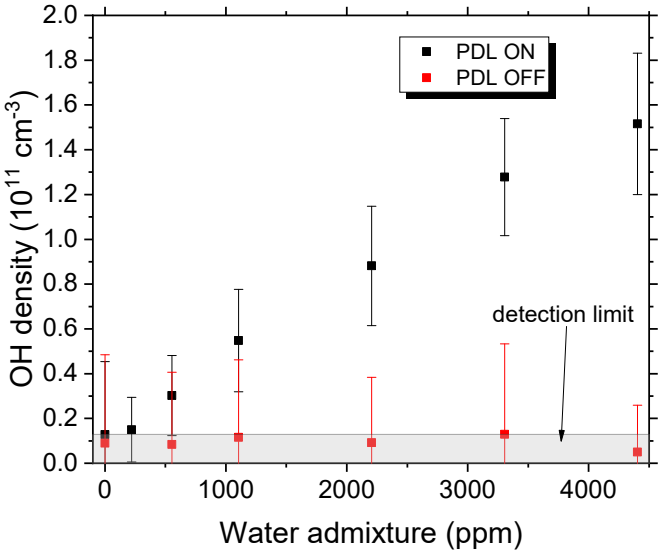

Figure 4.10: Hydroxyl densities versus water admixture using the modified COST jet measured with PDLIF. The hydroxyl density without photodissociation laser is shown in black, the hydroxyl density with photodissociation laser is shown in red. Conditions: 5 slm He, 178 V_{RMS}

Figure 4.10 depicts the hydroxyl densities versus the water admixture using the modified COST jet. The helium flow was 5 slm and the voltage was kept constant at 178 V_{RMS}. The point of measurement was approximately 5 mm after the 80 cm long tube from the jet. Given the inner diameter of the tube was 4 mm, the air was not likely to influence the measurements.

It can be observed that the hydroxyl densities, with PDL off, stay close to zero and do not increase.

This might indicate a detection limit or the non-existence of hydroxyl in the effluent. According to simulations, the chemistry at this point is in equilibrium.

However, with PDL on, the hydroxyl densities increased steadily from the detection limit to $(1.5 \pm 0.3) \cdot 10^{11}$ cm^{-3} with the highest tested water admixture of 4400 ppm.

This demonstrates that hydrogen peroxide is present, as already shown in figure 4.2, and the detection limit might be responsible for low absolute numbers.

While the hydroxyl densities at 80 cm after the plasma are very low, they should still be detectable at 9 mm and further. This was tested for the COST jet.

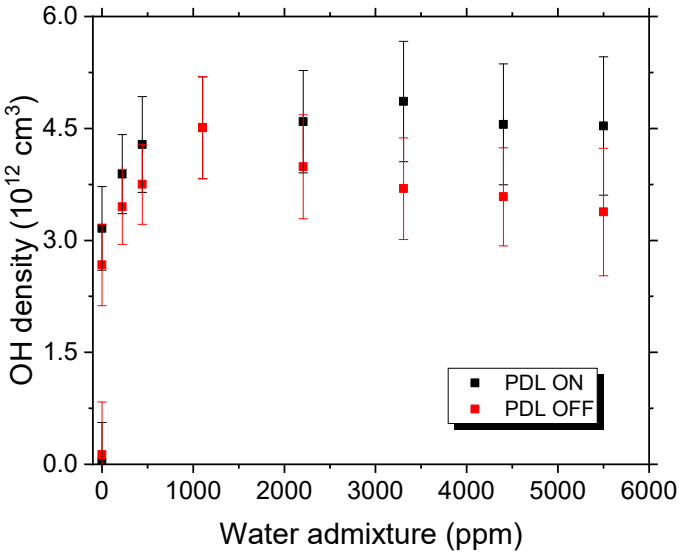

Figure 4.11: Hydroxyl densities with (black) and without (red) PDL for the water variation using the COST jet. The measurement point was 9 mm from the electrodes. Conditions: 500 sccm total helium flow, 178 V_{RMS}

Figure 4.11 shows the hydroxyl concentrations versus the water admixture using the COST jet. The hydroxyl densities without photodissociation laser are shown in red, while the hydroxyl densities with photodissociation laser are shown in black. The total helium flow was 500 sccm and the voltage was kept constant at 178 V_{RMS}. The measurement point was 9 mm from the electrodes.

In the case of the plasma produced hydroxyl, by increasing the water admixture up to 1300 ppm resulted in an increased hydroxyl density off $4.5 \pm 0.7 \cdot 10^{12}$ cm^{-3}. Increasing the water admixture further up to 5500 ppm resulted in a decrease of hydroxyl densities down to $3.4 \pm 0.9 \cdot 10^{12}$ cm^{-3}.

The sudden increase and then slow decline might be explained with a change of chemistry in the plasma. According to [1] the hydroxyl and atomic oxygen densities in the plasma rise and saturate after 5000 ppm water admixture. Atomic oxygen TALIF measurements have been done on the COST jet and water containing plasma but with a higher voltage. These show that the atomic oxygen production peaks at 6000 ppm water admixture.

In the event that hydroxyl is produced by the PDL, the trend was similar up to 1300 ppm but the hydroxyl densities are consistently (13 ± 2) % higher. After 1300 ppm, the PDL produced hydroxyl densities stay constant at $4.5 \pm 0.8 \cdot 10^{12}$ cm^{-3} which indicates, that the hydrogen peroxide densities raise, as was found previously from FTIR measurements.

At any admixture both, plasma and PDL produced hydroxyl, stay within error bars. The standard deviation stayed around (17 ± 3) %. This can be attributed to the deviation in laser power.

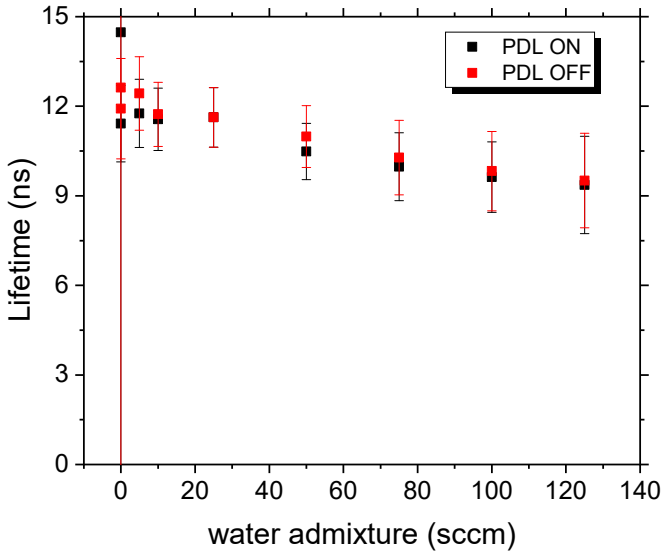

Figure 4.12: Lifetimes of hydroxyl for the water variation using the COST jet. The lifetimes without photodissociation laser are shown in red, the lifetimes with photodissociation laser are shown in black. The measurement point is 9 mm after the electrodes. Conditions: 500 sccm He, 178 V_{RMS}.

Figure 4.12 shows the lifetimes of plasma (red) and PDL (black) generated hydroxyl for the above discussed water variation. Both lifetimes overlap with each other and stay well within error bars. This indicates that the extra generated hydroxyl does not effect the lifetimes in a measurable manner, justifying the use of the PDL generated lifetimes. At 0 ppm water admixture, lifetimes could be measured but the relative standard deviation was higher than 100 %. The measured lifetimes result from water residue from the tube walls and impurities from the feed gas. Admixing 440 ppm of water resulted in a relative standard deviation of 9 % and a lifetime of 12 ns. Increasing the water admixture up to 5500 ppm permitted the lifetimes to decrease linearly down to 9.5±1.6 ns.

4.3.1 COST jet effluent

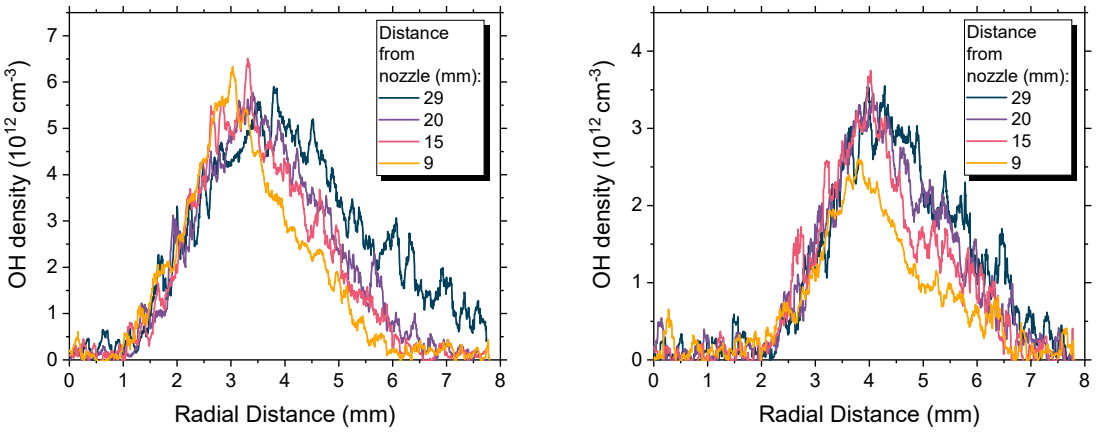

Figure 4.13: Hydroxyl density cross sections for 500 sccm a) and 1000 sccm b) total helium flow measured with PDLIF using the COST jet. The flow through the bubbler was 9 sccm in both cases. No plasma was used to generate the hydroxyl.

One advantage of the PDLIF setup was to obtain spatial resolution of hydroxyl densities. This allows for an investigation of the effluent of the COST jet and can characterise the hydroxyl distribution in space. To do this, the hydrodynamics of the flow were characterised by introducing *tert*-Butyl hydroperoxide into the helium without plasma. The *tert*-Butyl hydroperoxide was dissociated with the PDL. By using this method, the distribution of the helium exiting the jet can be visualized. The jet was mounted vertically, pointing downwards. The laser beam was estimated to be 0.2 mm to 0.5 mm, measured using an iris.

Figure 4.13 depicts the effluent profiles for a) 500 sccm and b) 1000 sccm total helium flow for 9 mm, 15 mm, 20 mm, and 29 mm. The plasma was switched off and the bubbler flow was 9 sccm for both cases. The PDL was used to dissociate *tert*-Butyl hydroperoxide and measure the resulting hydroxyl densities. In both cases, the profiles were approximately 4 mm wide and did not change significantly over the length of 9 mm to 29 mm. This suggests that the effluent is a stable gas channel. By using the lifetimes from this measurement, the air admixture to the gas stream can be estimated.

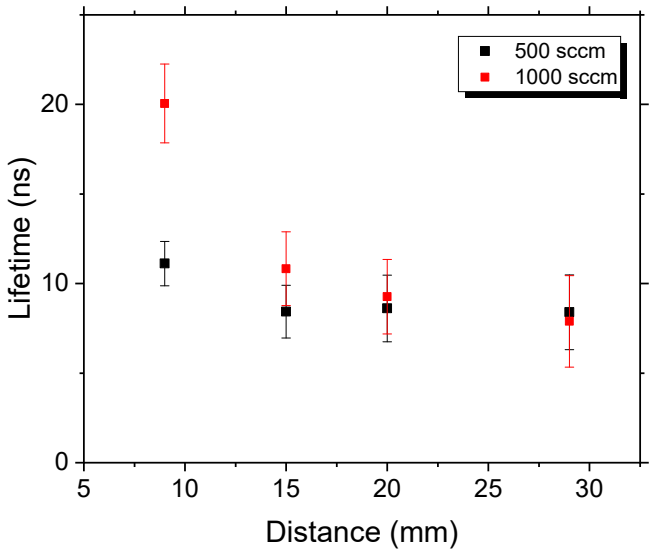

Figure 4.14: Hydroxyl lifetimes from tert-butyl hydroperoxide cross sections of the effluent for 500 sccm (black) and 1000 sccm (red) total helium flow for the COST jet. The lifetimes correspond to the maxima of the cross sections depicted in figure 4.13. No plasma was used for these measurements.

Figure 4.14 depicts the hydroxyl lifetimes from the effluent cross sections with *tert*-Butyl hydroperoxide. The lifetimes were taken from the maxima from figures 4.13a and 4.13b. In the case of 1000 sccm total helium flow (red), the lifetimes start at (20 ± 2) ns at 9 mm and decrease to (10 ± 2) ns at 15 mm and plateau after 20 mm at (8 ± 2) ns.

In the case of 500 sccm total helium flow (black), the lifetimes start at (11 ± 1) ns at 9 mm. They plateau after 15 mm at (8.5 ± 2.0) ns.

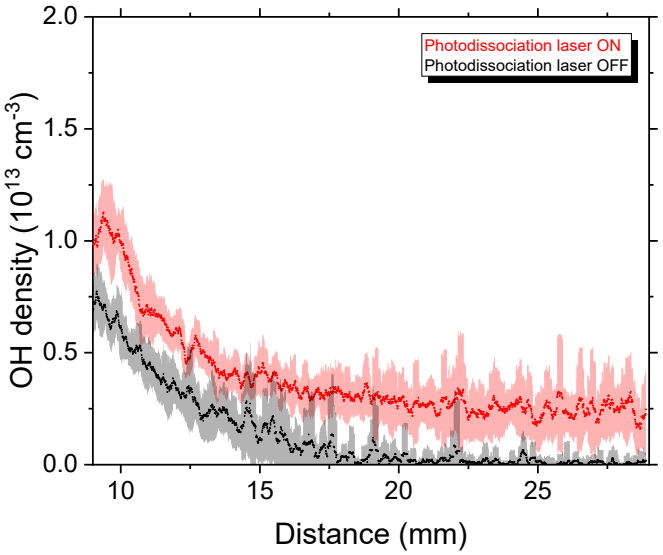

Figure 4.15: Hydroxyl densities for the distance variation of the effluent flowing into the atmosphere measured with PDLIF. Conditions: 500 sccm total helium flow, 4400 ppm, 178 V_{RMS}, COST jet.

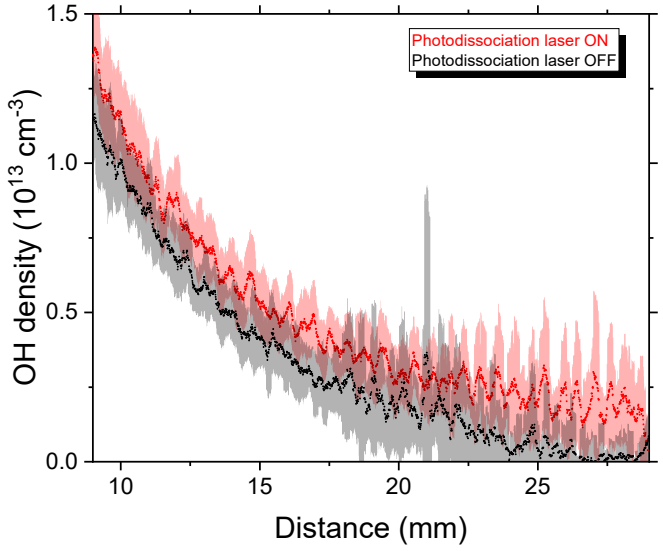

Figure 4.16: Hydroxyl densities for the distance variation of the effluent flowing into the atmosphere measured with PDLIF. Conditions: 1000 sccm total helium flow, 4400 ppm, 178 V_{RMS}, COST jet.

Figures 4.15 and 4.16 depict the hydroxyl densities for the distance variation using the COST jet. With the PDL off, the hydroxyl measurements are shown in black and the hydroxyl measurements with PDL on are shown in red. The conditions were 178 V_{RMV},

4400 ppm water admixture and 500 sccm and 1000 sccm total helium flow. In the case of 500 sccm helium flow (figure 4.4a), a clear difference between densities with and without PDL exists. The hydroxyl density without PDL decays exponentially and started with $7 \pm 1 \cdot 10^{12}\,\mathrm{cm}^{-3}$ from 9 mm to undetectable after 20 mm. While the densities with PDL on follow the exponential decay starting with $9.9 \pm 1.5 \cdot 10^{12}\,\mathrm{cm}^{-3}$ and slightly increased to $1.1 \pm 0.2 \cdot 10^{13}\,\mathrm{cm}^{-3}$. The densities followed the same trend but were still detectable and stayed constant after 20 mm at $2.6 \pm 0.9 \cdot 10^{13}\,\mathrm{cm}^{-3}$.

As was depicted earlier in graph 4.4a, the hydrogen peroxide densities stayed constant at $0.5 \cdot 10^{15}\,\mathrm{cm}^{-3}$ suggesting that no new significant amounts of hydrogen peroxide were formed. This argument is supported through a comparison of the hydroxyl and hydrogen peroxide densities. Assuming all hydroxyl from 9 mm after the plasma is converted into hydrogen peroxide, the resulting density would be approximately $3.25 \cdot 10^{12}\,\mathrm{cm}^{-3}$. This is two magnitudes lower than the measured hydrogen peroxide density and not measurable with this setup.

Thus, the majority of the hydrogen peroxide must have formed in the plasma and in the 9 mm after the plasma.

The lifetime trend is the same, within error bars, compared to figure 4.14. This suggests, that the same amount of air might have been transported into the effluent.

In the case of 1000 sccm total helium flow, the pattern of hydroxyl decay is similar. The hydroxyl density in the effluent decayed exponentially from $1.1 \pm 0.2 \cdot 10^{13}\,\mathrm{cm}^{-3}$ at 9 mm to not detectable at 25 mm. This is 5 mm longer than in the 500 sccm flow case above. With PDL on, the hydroxyl density is higher, but still within a standard deviation of PDL off. Also in this case, the hydroxyl density was constant after 25 mm, instead of 20 mm. To rule out the dispersion of the effluent, further investigations were made.

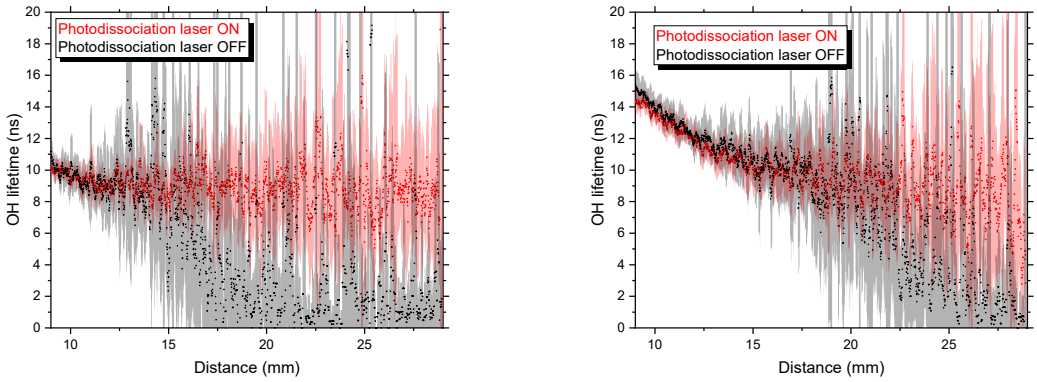

a) 500 sccm b) 1000 sccm

Figure 4.17: Hydroxyl lifetimes for the distance variation of the effluent flowing into the atmosphere measured with PDLIF. Conditions: 500 sccm (a) and 1000 sccm (b) total helium flow, 4400 ppm, 178 V_{RMS}, COST jet.

Species	Gas	Diffusivity (Torr cm^2 s^{-1})	Reference
OH	He	662 ± 33	[155]
	air	163 ± 20	[155]
H_2O_2	He		
	air	116 ± 35	[156]
He	air	0.7337	[157]
H_2O	air	0.282	[157]

Table 4.2: Diffusion coefficients in helium and air for species relevant in this study.

Figure 4.17 shows the hydroxyl lifetimes from the above mentioned hydroxyl measurements. The lifetimes were 11 point averaged. In the case of 500 sccm total helium flow, the lifetimes decay nearly linearly from (10.1 ± 0.5) ns until 15 mm to (8 ± 4) ns. After that, the hydroxyl lifetimes with PDL off decreased within 5 mm to nearly zero ns. The lifetimes of hydroxyl generated by the PDL stayed constant at (8 ± 2) ns, which suggests that the helium air mixture stays constant. The hydroxyl produced by the plasma must have diffused out of the gas stream or reacted with other components of the effluent or air. Another possible explanation would be that the hydroxyl density was not high enough to be distinguished from noise.

A similar behaviour can be seen for 1000 sccm total helium flow. In this case, however, the hydroxyl lifetimes with PDL off decreased from (15 ± 1) ns at 9 mm until 18 mm to (9 ± 4) ns and then rapidly decreased. The lifetimes for the hydroxyl generated by the PDL remained constant, suggesting that the helium air admixture stayed constant at (8 ± 5) ns. The hydroxyl coming from the plasma, might have reacted or diffused out of the gas stream.

The lifetimes at 9 mm are (10.1 ± 0.5) ns for 500 sccm and (15 ± 1) ns for 1000 sccm. This can be linked to the different speeds of the gas. The lifetimes at the separation of the plasma and PDL generated hydroxyl are approximately 8 ns for both flow cases but at 15 mm (500 sccm) and 20 mm (1000sccm) indicating the different gas velocities. This also indicates that the effluent stream was of the same air helium mixture at this position and the separation point extended with higher gas flows.

Compared to figure 4.14, it is noticeable that the *tert*-Butyl hydroperoxide derived hydroxyl lifetime at 9 mm is 5 ns higher. This can be attributed to the unknown quenching coefficient and lower density of *tert*-butyl hydroperoxide. Moving further away from the jet, the lifetimes become the same values, within error bars. This indicates that more air was transported in to the effluent and the quenching coefficients of nitrogen and oxygen start to dominate. Another possibility would be, that the plasma changes the behaviour of the effluent. This has been observed in Boselli et al. [153] and Robert et al. [154] using Schlieren images. However, the jets used in these studies were of different nature and the plasma protrudes into the air. This would be an unlikely occurrence for the COST jet.

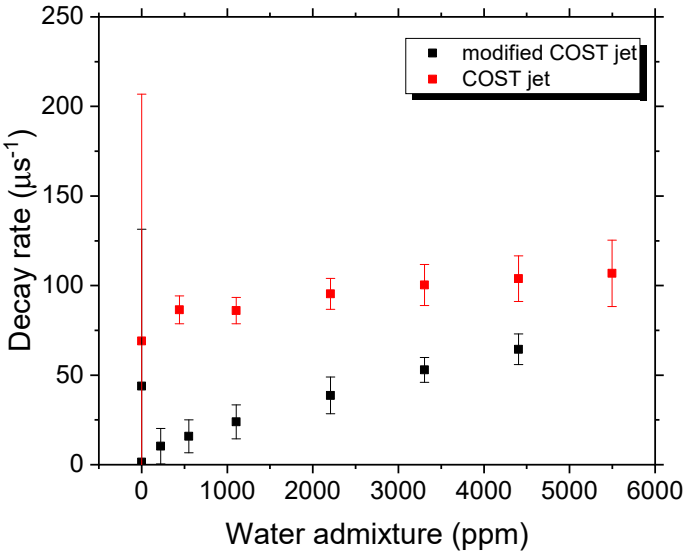

Figure 4.18: Hydroxyl decayrates for the water variation using the modified COST jet (black) and COST jet (red) measured with PDLIF. The hydroxyl lifetimes are measured with PDL on. Conditions: 5 slm (modified COST jet) and 500 sccm (COST jet) total helium flow, 178 V_{RMS}

Figure 4.18 shows the decay rates of hydroxyl from the water variation with the modified COST jet (black) and the COST jet (red). The measurement points were 5 mm after the 1 m tube (modified COST jet) and 9 mm after the electrodes (COST jet). In the case of the modified COST jet, the hydroxyl generated from hydrogen peroxide is shown because the hydroxyl generated by the plasma already reacted in the effluent and is no longer detectable. In both cases, the measurements at 0 ppm water admixture show high standard deviations. This is because only trace amounts of hydroxyl or noise were detected. In the case of the modified COST jet, decay rates increase with increasing water admixture with $12.9 \pm 0.4\,\mu s^{-1}(1000\,ppm)^{-1}$ while in the case of the COST jet, the decay rates increased with $4.7 \pm 0.6\,\mu s^{-1}(1000\,ppm)^{-1}$ and did not rise more than 10 % over the tested admixtures. The discrepancy between both measured series was due to the air admixture into the gas stream of the COST jet. The effluent of the modified COST jet was not diluted by incoming gases at 5 mm after the tube. Based on [56], the effluent of the COST jet can be estimated to be diluted as much as 70 % at 9 m after the electrodes. However, according to Ellerweg et al. [58] it might be less than 80 % diluted.

Therefore, quenching by air plays a major role for the COST jet measurements.

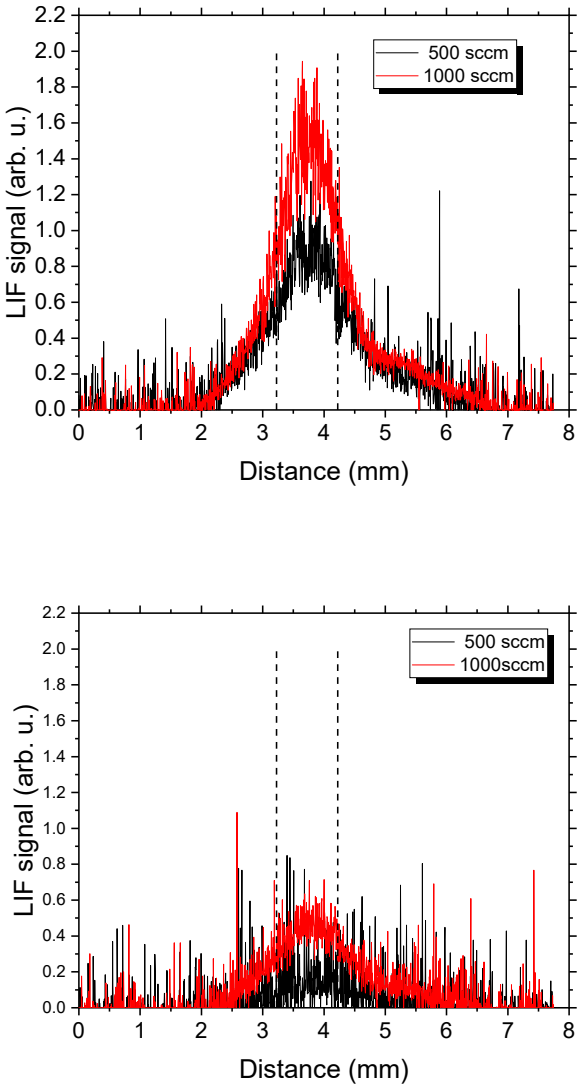

Figure 4.19: Hydroxyl density profiles at 9 mm, 15 mm, and 25 mm (top to bottom figure) after the plasma for 500 sccm (black) and 1000 sccm (red) total helium flow measured with PDLIF. Conditions: 4400 ppm water admixture, 178 V_{RMS}, COST jet.

Figure 4.19 depict the cross sections of the effluent for 500 sccm (black) and 1000 sccm (red) total helium flow 9 mm, 15 mm, and 29 mm after the plasma, respectively. The water content for both cases was 4400 ppm and the voltage was 178 V_{RMS}. The position of the plasma channel is indicated with black dashed lines. The cross sections were recorded by moving the jet 8 mm with a speed of 0.5 mm s^{-1} through the laser beam. The laser beam was estimated to be 0.2 mm to 0.5 mm, measured using an iris.

At 9 mm and 1000 mm, the hydroxyl density started increasing approximately 1 mm outside the 1 mm wide plasma channel. The density plateaued within the plasma channel at $(1.4 \pm 1.0) \cdot 10^{13}$ cm^{-3}. It is noteworthy that the plateau is relatively flat and is 0.5 mm wide. This is half the channel width. Moving on to a distance of 15 mm from the plasma, the density has approximately the same shape, but the profile plateaued at $(5.0 \pm 1.0) \cdot 10^{12}$ cm^{-3}. At 29 mm, no hydroxyl could be detected.

The maximum densities followed the trend previously observed in figure 4.16 within error bars. This confirms that the density trend in this figure 4.19 is solely a physical and chemical effect as opposed to a measurements artefact.

4.3.2 Stern-Volmer plot

To estimate the gas composition in the effluent for the water variations, the Stern-Volmer plot can be used. For this, the decay rates were plotted against the water admixture. Then, a linear regression was fitted.

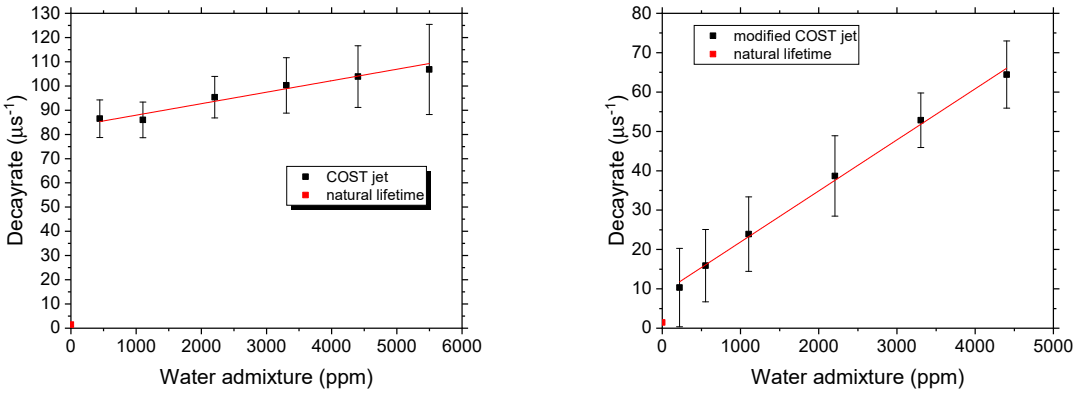

a) b)

Figure 4.20: Stern-Volmer plots for (a) the COST jet 9 mm after the plasma and (b) the modified COST jet directly 4 mm after the tube. Conditions for the COST jet: 500 sccm total helium flow, 178 V_{RMS}. Modified COST jet: 5 slm helium, 500 V_{pp}

Figure 4.20 shows the Stern-Volmer plot for the COST jet (a) and modified COST jet (b). The measured decay rates are in black and the actual, natural decay rate of hydroxyl is shown as a red square. To calculate the quenching rate, a linear plot was fitted to the data

Species	Quenching rate ($10^{-10} cm^{-3} s^{-1}$)	Reference
N_2	0.247	[135]
O_2	1.36	[159]
H_2O	7.23	[160]
H_2O_2	unknown	
He	0	[161]

Table 4.3: Quenching coefficients

points. In the case of the COST jet, the linear fit has an offset of 83±2 µs^{-1} and for the modified COST jet 9±1 µs^{-1}. This can be explained with a much higher air admixture into the effluent stream. The quenching rates of both measurements were not identical. The rates were 0.0047±0.0006 µs^{-1}ppm^{-1} for the COST jet and 0.0130±0.0004 µs^{-1}ppm^{-1} for the modified COST jet. One would expect that these should be the same. However, it is not known how much water remains in the effluent of the COST jet. To test this, the quenching rates were fitted to the measured lifetimes.

The lifetime of the hydroxyl molecule can be calculated with equation 4.4:

$$\begin{aligned} \tau^{-1} &= \tau_{natural}^{-1} + Q + k_V n \\ Q &= (0.8 k_{Q_{\mathrm{N_2}}} + 0.2 k_{Q_{\mathrm{O_2}}}) n_{air} + k_{Q_{\mathrm{H_2O}}} n_{H2O} \end{aligned} \tag{4.4}$$

With τ the lifetime, $\tau_{natural}$ the natural lifetime, Q the overall quenching coefficient, k_v the vibrational energy transfer, n_x the density of the species x and k_x the quenching rate of the species x.

This approach has been used in [34, 158] to calculate the air admixture into a plasma effluent and in [135] to measure the vibrational energy transfer of OH(A ^{2} Σ^+, v'=1). In this case, vibrational energy transfer has been disregarded because the conditions between measurements and calibration are similar and the vibrational transfer is fast compared to the rotational.

With the the quenching coefficients from table 4.3 for the most abundant quenchers in the effluent, it is possible to determine the gas admixture. For this, the Stern-Volmer plots from figure 4.20 were fitted with a linear fit.

The fit for the COST jet is $\tau^{-1} = n_{\mathrm{H_2O}}[ppm](4.7 \pm 0.6) \cdot 10^{-3}[s^{-1}] + (83.2 \pm 1.5)[s^{-1}]$. With the intercept, the air admixture in the effluent can be estimated. For 0 ppm water admixture the air admixture is 5.53 % which is in agreement with the model from Ellerweg et al. [58], predicting 5 % to 15 %. The model used a circular symmetry and a fluid model with helium and nitrogen to represent the air. This stands in contrast to Kelly et al. [56] . According to Kelly et al., the effluent should be diluted by 60 % to 80 % with air. This was shown in Schlieren images and simulation. The difference between the two models was that the jet in Kelly's paper was mounted horizontally and not vertically and buoyancy was taken into account. These were two parameters that were different in Ellerweg et al..

The linear fit for the modified COST jet yielded $\tau^{-1} = n_{H_2O}[ppm](13.0 \pm 0.4) \cdot 10^{-3}[s^{-1}] + (9 \pm 2)[s^{-1}]$. By comparing the intercept and the natural lifetime of hydroxyl, one can see an offset of $5.5\,s^{-1}$.

Using the air admixture ratio derived from the intercept, the water admixture in the effluent was fitted as close as possible. The results are depicted in figure 4.21. The black line represents the case of no water loss, the black data points are the water content in the effluent of the COST jet and the red data points are the water content in the modified COST jet effluent.

For the discrepancy between the water content in the effluent of the COST jet, several possibilities arise. The measurement point was 9 mm after the plasma. During this time, water is able to diffuse out of the stream. This effect can be estimated to be low because the exchange between effluent and surrounding air is below 10 % and the diffusion coefficients of water in air is one magnitude lower than in helium. Table 4.2 lists the diffusion coefficients for hydrogen and oxygen species.

Another possibility could be that species with high quenching coefficients could be produced. These are not included in this simplistic approach because it was not known what species this could be or how high the densities were. However, these would be bigger molecules because the quenching coefficient for hydroxyl increases with complexity of the quenching partner (as can be seen in Martini et al. [77]).

The last possibility would be that vibrational transfer from the higher level had a larger impact. This was not tested because only one optical filter for the Q(1) transition was available at the time.

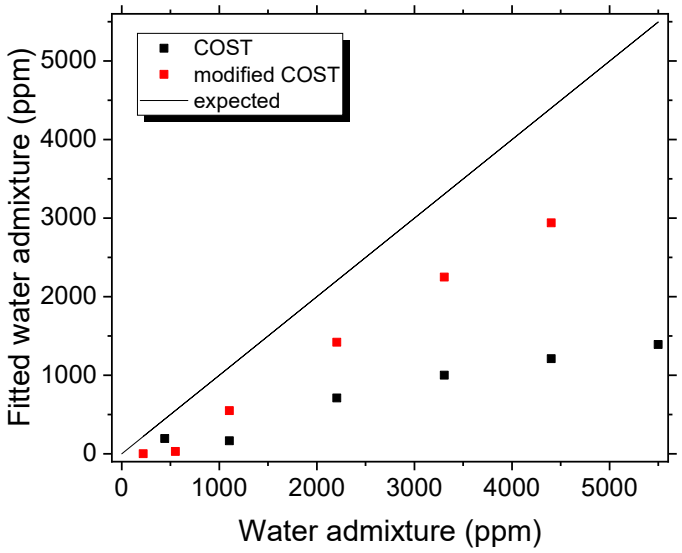

Figure 4.21: Water admixtures in the effluent extracted from the Stern-Volmer plots from figure 4.20.

4.3.3 Oxygen admixture

To complement the hydrogen peroxide measurements with water and oxygen, the atomic oxygen densities with similar parameters have been measured.

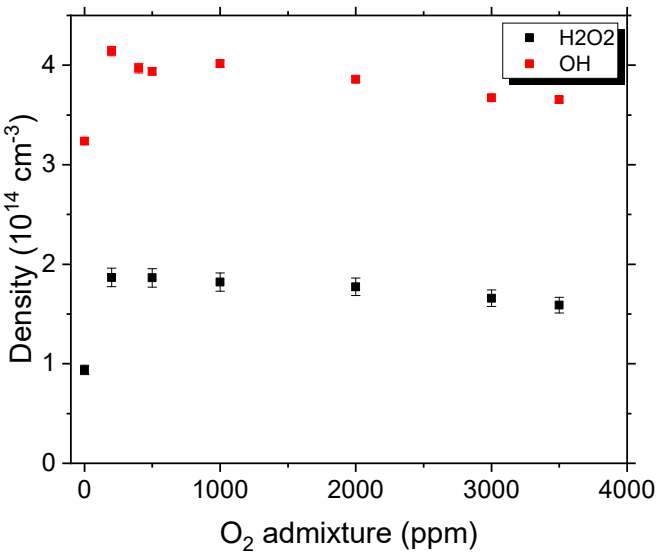

Figure 4.22: Hydroxyl and hydrogen peroxide densities versus oxygen admixture measured with FTIR (hydrogen peroxide) and absorption spectroscopy (hydroxyl). Conditions: 5 slm total helium flow, 4400 ppm water admixture, 0 ppm to 3488 ppm oxygen admixture, 178 V_{RMS}, modified COST jet.

Figure 4.22 depicts the hydroxyl densities for the oxygen variation using the modified COST jet. The hydroxyl densities were measured in the middle of the jet. The voltage was kept at 178 V_{RMS}, 5 slm total helium flow and 4400 ppm water admixture. The oxygen was varied from 0 ppm to 3488 ppm. It can be seen that from 0 ppm to 200 ppm oxygen admixture the hydroxyl density increased by 20 % and then slowly declined.

The hydroxyl densities in the plasma were approximately 3.5 times higher than the hydrogen peroxide densities in the far effluent. However, they follow the same trend as hydroxyl after oxygen was added. The conversion efficiency of hydroxyl in the plasma to hydrogen peroxide outside the plasma was 56 % without oxygen admixture and was increased to 88 % with oxygen admixture. This shows that the main hydroxyl consumption in the effluent of the plasma is the build up of hydrogen peroxide.

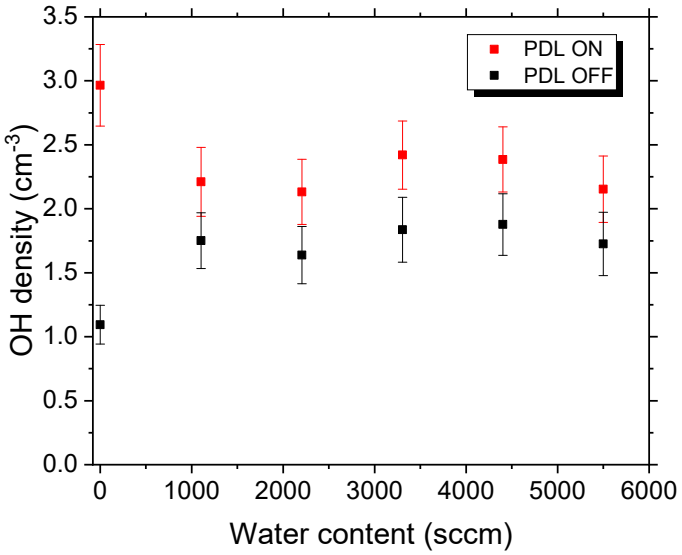

Figure 4.23: Hydroxyl densities with (black) and without (red) PDL versus water admixture with a fixed oxygen admixture using the COST jet. The measurement point is 9 mm from the electrodes. Conditions: 500 sccm total helium flow, 1000 ppm oxygen admixture, 178 V_{RMS}.

Figure 4.23 shows the hydroxyl densities for the water variation with a fixed oxygen admixture of 1000 ppm using the COST jet. The total helium flow was 500 sccm and the voltage was kept constant at 178 V_{RMS}. In the case of PDL off, it can be seen that adding 110 ppm water resulted in an increase of hydroxyl densities of approximately 1.5 times from $(1.1 \pm 0.2) \cdot 10^{13}\,cm^{-3}$ to $(1.8 \pm 0.2) \cdot 10^{13}\,cm^{-3}$. Adding more water did not increase hydroxyl densities. In the case the of PDL on, admixing water led to a decrease in hydroxyl densities by approximately 0.8 times from $(2.9 \pm 0.3) \cdot 10^{13}\,cm^{-3}$ to $(2.2 \pm 0.3) \cdot 10^{13}\,cm^{-3}$. This density difference between PDL on and off for 0 ppm water admixture indicated that the tubes were not completely dry and a large amount of H_2O_2 is generated, or ozone interferes with the hydroxyl measurements. Ozone is split by the PDL into one oxygen molecule and atomic oxygen which reacts with water to hydroxyl. This was the most likely explanation because no hydroxyl could be detected without the plasma.

Figure 4.24 shows the oxygen variation with fixed water admixture of 4400 ppm. The voltage was kept constant at 178 V_{RMS} and the overall helium flow was 500 sccm.

In the case of PDL off, it can be seen that the hydroxyl density rose by approximately 4 times from $(3.6 \pm 0.7) \cdot 10^{12}\,cm^{-3}$ to $(1.5 \pm 0.2) \cdot 10^{13}\,cm^{-3}$ by adding 1000 ppm of oxygen to the plasma. Any further oxygen admixture led to a slow decline of hydroxyl down to $(1.1 \pm 0.2) \cdot 10^{13}\,cm^{-3}$ with the highest oxygen admixture of 4000 ppm. This increase of hydroxyl in the plasma by admixing oxygen was already observed in figure 4.22. With 20 %, the increase was lower than outside the plasma. The density was one magnitude lower in the effluent than in the plasma. Assuming both jets can be compared, the much higher

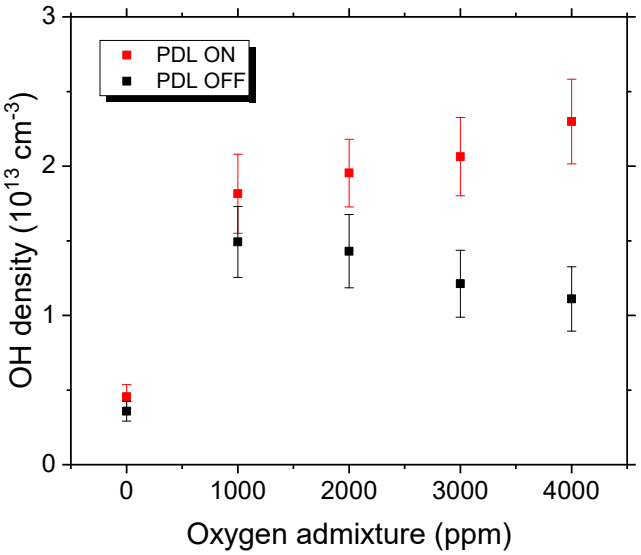

Figure 4.24: Hydroxyl densities with (black) and without (red) PDL versus oxygen admixture with a fixed water admixture using the COST jet. The measurement point is 9 mm from the electrodes. Conditions: 500 sccm total helium flow, 1000 ppm oxygen admixture, 178 V_{RMS}

sensitivity of the effluent to oxygen admixture could be explained by ozone formation from atomic oxygen after the plasma. For this, the atomic oxygen density was measured and is depicted in 4.26.

In the case of PDL on, the added oxygen led to a nearly four fold higher density and increasing the oxygen admixture led to an increase of hydroxyl densities up to $(2.3 \pm 0.3) \cdot 10^{13}\,\mathrm{cm}^{-3}$ with 4000 ppm oxygen admixture. This indicates a growing hydrogen peroxide density which is contrary as seen in figure 4.5. The increased hydroxyl densities might be caused by abundant ozone that was dissociated by the PDL and the subsequent reaction of atomic oxygen with water.

4.4 Gas Temperature from hydroxyl rotational spectrum

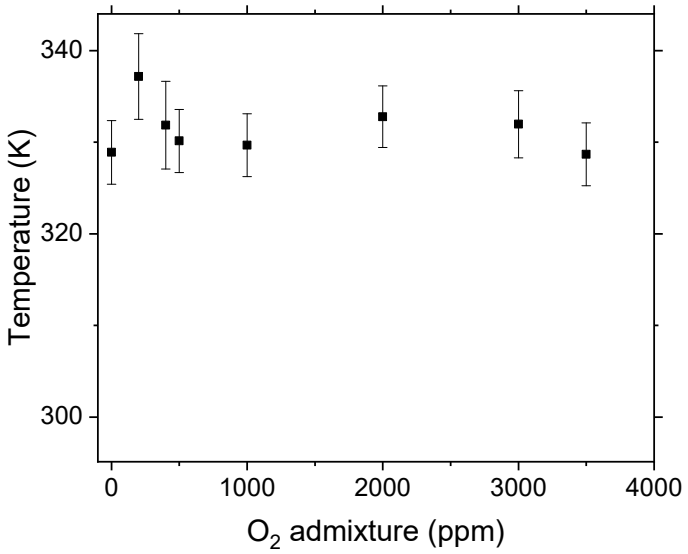

Figure 4.25: Gas temperatures derived from hydroxyl rovibrational absorption spectra versus oxygen admixture. The measurement point is in the middle of the plasma. Conditions: 5 slm helium, 4400 ppm water admixture, 178 V_{RMS}, modified COST jet.

To rule out any gas temperature effects that could effect the plasma chemistry, the temperature inside the plasma was measured using the absorption spectroscopy measurements. The spectra were fitted as described in section 2.4.

Figure 4.25 depicts the gas temperature derived from the rovibrational absorption spectra of hydroxyl for the oxygen variation. The conditions were 178 V_{RMS}, 5 slm total helium flow and 4400 ppm water admixture. It can be seen that the rovibrational temperatures are stable at (331 ± 4) K with a small peak to (337 ± 5) K at 200 ppm oxygen admixture. The relative standard deviation for the fit of the measurements was approximately 1 %. Deriving the gas temperature from hydroxyl rovibrational spectra harbours some challenges due to the nature of the hydroxyl molecule as explained in this paper [113]. The energy levels were not necessarily Boltzmann distributed, which can result in elevated temperatures not representing the gas temperature. This problem is more pronounced in emission spectra. The low fitting error depicted that the simulated spectra represent accurately the situation in the plasma.

This indicates that the oxygen admixture had no influence on the gas temperature. Therefore, the temperature can be excluded from potential factors that alter the hydrogen peroxide and hydroxyl densities.

4.5 Atomic oxygen densities

Atomic oxygen is a highly reactive species. It decays quickly after the plasma to form ozone or hydroxyl from water. Atomic oxygen is one of the last variables to explain why hydrogen peroxide that was measured. This high reactivity makes it an interesting radical for biomedical applications because it can set off a chain reaction, which creates more radicals and highly reactive molecules that are longer lived than atomic oxygen itself.

The most common and direct method to measure atomic oxygen densities is TALIF. In this work, it was measured with the picosecond TALIF system described in 2.7.

To complement the measurements above, atomic oxygen was measured on the COST for conditions that mix water and oxygen. The atomic oxygen concentration as a function of water admixture has been measured before in [1] and was not repeated. In this study, atomic oxygen densities were measured by vacuum ultra violet-fourier transformation absorption spectroscopy (VUV-FTAS) in the plasma of the modified COST jet. The densities rise from zero water admixture up to 2000 ppm and plateau at approximately $3.0 \pm 0.5 \cdot 10^{13}\,\mathrm{cm}^{-3}$.

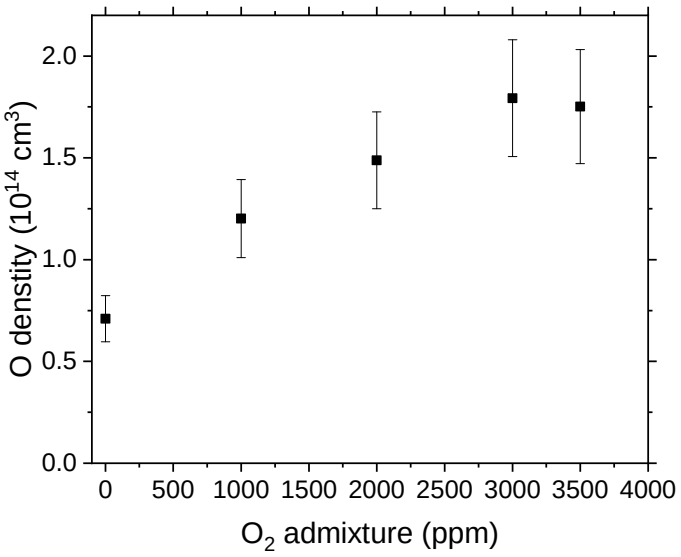

Figure 4.26: Atomic oxygen densities versus oxygen admixture with a fixed water admixture of 4400 ppm. Measured with TALIF 1 mm in front of the electrodes. Conditions: COST jet: 500 sccm total helium flow, 178 V_{RMS}.

Figure 4.26 shows the atomic oxygen densities from the oxygen variation for a fixed water admixture of 4400 ppm for the COST jet. The atomic oxygen densities are measured 1 mm in front of the electrode tips and the total flow of helium was 500 sccm and the voltage kept constant at 178 V_{RMS}.

With increasing oxygen admixture the atomic oxygen densities also increased. For oxygen admixtures above 2000 ppm, the densities plateau. The density without additional oxygen

admixture is with $6.7 \cdot 10^{13}\,\mathrm{cm}^{-3}$ in the same magnitude as measured in [59]. The total helium flow and voltage were 1.4 slm and $200\,\mathrm{V_{RMS}}$ in this study and, therefore, higher than in this work. Additionally, a nanosecond laser was used instead of a picosecond laser. This means that the quenching rates have to be calculated, instead of being measured directly as was done in this work.

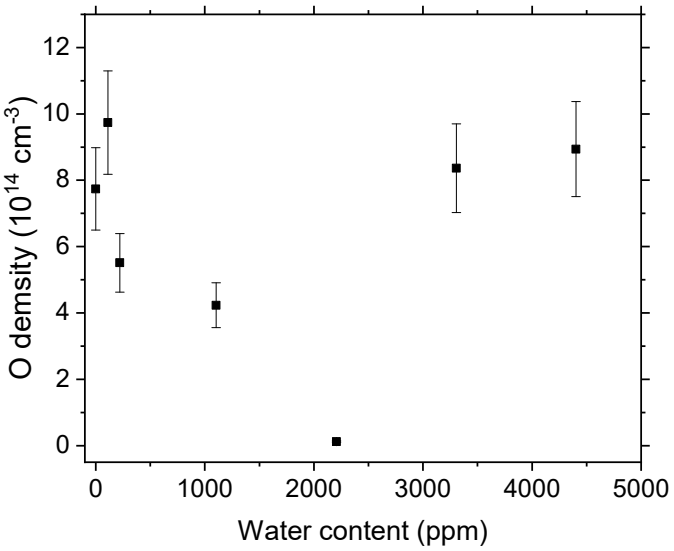

Figure 4.27: Atomic oxygen densities versus water admixture with fixed oxygen admixture. Measured with TALIF 1 mm in front of the electrodes of the COST jet. Conditions: 500 sccm total helium flow, 3000 ppm oxygen admixture, $178\,\mathrm{V_{RMS}}$

Figure 4.27 shows the atomic oxygen densities for a water variation with a fixed amount of 3000 ppm oxygen admixture. The ozone data was measured with the modified COST jet and can also be found in figure 4.7. The atomic oxygen densities were measured by TALIF 1 mm in front of the electrode tips. 500 sccm total helium flow and $178\,\mathrm{V_{RMS}}$ and 3000 ppm oxygen admixture were chosen to make the modified and original COST jet as comparable as possible.

It can be observed that the oxygen densities decline from 0 ppm to 2200 ppm and afterwards rise with increasing water admixture. Benedikt et al. [59] showed that a maximum atomic oxygen concentration will be reached around 6000 ppm water admixture without oxygen admixture. However, these measurements were not done with additional oxygen admixture. The atomic oxygen densities reported in Benedikt et al. were consistently one magnitude lower than the densities measured with added oxygen.

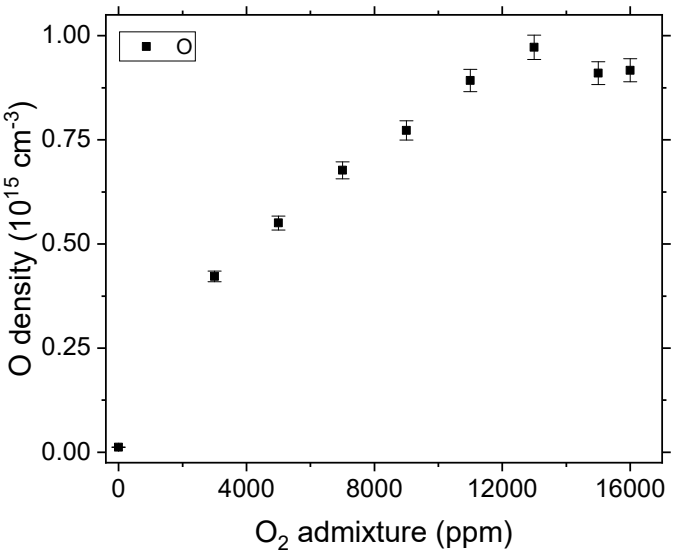

Figure 4.28: Atomic oxygen density as a function of oxygen admixture for a water containing plasma. Measured with TALIF 1 mm in front of the electrodes. Conditions: 500 sccm total helium flow, 4400 ppm water admixture, 300 V_{RMS}, COST jet.

Figure 4.28 shows the oxygen variation for the COST jet with a water containing plasma. The atomic oxygen is measured with TALIF 1 mm in front of the electrodes. The conditions were 500 sccm total helium flow, 4400 ppm water admixture and 300 V_{RMS}. This voltage was chosen because it allowed for the use of the highest range of oxygen admixture.

The atomic oxygen densities increased linearly from 3000 ppm to 13000 ppm oxygen admixture from $0.42 \cdot 10^{15}$ cm^{-3} to $0.97 \cdot 10^{15}$ cm^{-3}. Afterwards, the density drops to $0.92 \cdot 10^{15}$ cm^{-3}. The linear increase was unexpected because the ozone densities did not increase linearly. One has to take into account that for the atomic oxygen measurements and ozone measurements two different jets and distances to the plasma were used. The atomic oxygen was measured very close to the plasma and the ozone was measured in the far effluent. As can be observed from previous measurements with an earlier version of the COST jet and water admixtures [59], the atomic oxygen density declines within 10 mm after the electrodes. During that time, the atomic oxygen reacts with atomic hydrogen, hydroxyl, water, hydrogen peroxide and oxygen to mainly form oxygen, ozone and atomic hydrogen.

4.6 Summary and conclusion

In this chapter, FTIR, LIF, and PDLIF were used to investigate the influence of various water and water plus oxygen admixtures on the formation of hydrogen peroxide, ozone, hydroxyl, and atomic oxygen. In the following the key results of this chapter will be summarised.

H_2O_2 Absolute hydrogen peroxide densities were measured by FTIR in the far effluent of the modified COST jet and by PDLIF 9 mm to 29 mm from the electrodes of the COST jet. Increasing the water admixture at a constant voltage of 178 V_{RMS} increased the hydrogen peroxide concentrations in the far effluent. While varying the voltage at low water admixtures (884 ppm), the hydrogen peroxide concentrations increased linearly. Adding more water to the voltage variation saturates the hydrogen peroxide densities.

Comparing the results from the FTIR with PDLIF for the water variation, the PDLIF densities are three times lower. This might be a result from the underlying hydroxyl measurements as discussed above.

The distance variation from the COST jet revealed a constant hydrogen peroxide density from 9 mm to 29 mm from the jet nozzle in both flow cases.

Adding oxygen to the water containing plasma doubles the amount of hydrogen peroxide in the far effluent. This allows to tailor the plasma which has not been shown before. Measurements with the PDLIF setup did not result in useable data due to ozone interference.

O_3 Absolute ozone densities were measured by a commercially available ozone monitor in the far effluent of the plasma of the modified COST jet. Without oxygen admixture, no ozone could be detected. Adding oxygen to the wet plasma results in an increased ozone density which is only weakly coupled to the hydrogen peroxide densities. The ozone concentration did not increase linearly with oxygen admixture.

OH Absolute hydroxyl densities were measured by LIF and absorption spectroscopy. While the hydroxyl density has been measured for water containing plasmas in and outside of the plasma in the past, it has not been done for water and oxygen containing plasmas. Absorption spectroscopy on the modified COST jet revealed that the hydroxyl density only increased by 20 % in the middle of the plasma. Adding oxygen also increased the conversion efficiency of hydroxyl to hydrogen peroxide from 56 % to 88 %. The gas temperature extracted from the hydroxyl spectra remained constant over the range of oxygen admixtures.

Absolute hydroxyl densities have been measured in the effluent of the COST jet by LIF. The hydroxyl densities decreased exponentially from 9 mm to 29 mm and stay within a narrow gas stream. Absolute numbers were achieved by calibrating the setup with a PDL and tert-Butyl hydroperoxide. By testing the cross section of the effluent without plasma, it could

be determined that the effluent is a narrow and homogeneous gas channel in which air is admixing over the length of a few centimetres.

O Absolute atomic oxygen densities were measured by TALIF 1 mm above the electrodes of the COST jet. This tested how the atomic oxygen density changed in a plasma with 4400 ppm water admixture for 178 V_{RMS}. The atomic oxygen density increased linearly with the oxygen admixture until the plasma distinguished. A further investigation with 300 V_{RMS} revealed a similar behaviour, but with a clear maximum at 13000 ppm oxygen admixture.

The atomic oxygen density was also tested for a constant oxygen admixture of 1000 ppm and varying water admixtures at 178 V_{RMS}. This revealed a u-shaped characteristic graph behaviour with the minimum at 2200 ppm water admixture.

Chapter 5

Investigation of kINPen with water admixture and different gas curtains

In the previous chapter, the effects of oxygen admixture to water containing plasmas in the COST and modified COST jet have been experimentally characterised. It was found that the admixture of oxygen can be used to tailor hydrogen peroxide, ozone and atomic oxygen production in water containing plasma. This chapter looks at the atomic oxygen production of a more application based plasma source, the kINPen, and tests if the plasma of the kINPen behaves similarly to that of the COST jet.

Many studies have been conducted on the various versions of the kINPen [31].

The kINPen will be briefly explained in section 5.1 and the experimental setup in 5.2. After this, the effect of water admixture to the kINPen with different gas curtains will be presented in section 5.3, while in section 5.4 the effect of dry and wet surfaces without a gas curtain along with wet and dry plasma will be presented.

5.1 Plasma source kINPen

The kINPen is a plasma jet that was developed by the INP Greifswald and made commercially available by the neoplas tools GmbH [162]. The name derives from Dr E Kindel for the "k", "INP" for the institute and "Pen" for the pen-like shape of the device.

Different versions of the kINPen exist today and a comprehensive overview is provided in Reuter et al. [31]. The model used in this work is the kINPen Sci [29]. This jet operates with argon and molecular admixtures in the plasma and with a pulse frequency of 940 kHz. The jet consists of a dielectric tube with an inner diameter of 1.6 mm and an outer diameter of 2 mm in which the working gas flows. The driven electrode inside the tube is a metal rod with 1 mm diameter and is sharpened at the tip. The tip is 3.5 mm away from the nozzle

exit inside the tube. To shield the plasma effluent, an additional nozzle can be placed on top of the plasma nozzle [123, 163, 164]. This additional nozzle (black part around the nozzle in figure 5.1) is fed by a separate gas supply. In this work, oxygen, nitrogen and synthetic air (80 % nitrogen, 20 % oxygen) are used as a gas curtain.

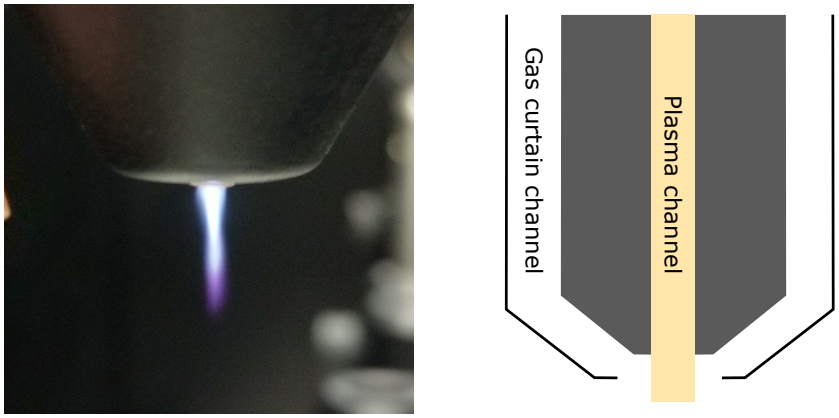

Figure 5.1: Plasma produced by the KINPen. The gas curtain is switched off. The visible after glow of the plasma is approximately 1 cm long. Conditions: plasma: 3 slm Ar, 2200 ppm water.

Figure 5.1 shows a close up of the plasma effluent and the black plastic nozzle that enables plasma effluent gas shielding on the left and a cross-section of the plasma jet on the right. The effluent is approximately 10 mm long and exhibits a blue colour up until half of its length. The rest of the plasma effluent is purple. The blue colour originates from the wet argon gas and the purple colour indicates nitrogen streaming in from the side of the plasma effluent.

Because the kINPen is powered by pulses and operates in a semi dielectric way (one bare metal and one covered electrode), it is not a continuous plasma. With a fast camera, such as 4picos, one can see that the plasma is made up of a succession of streamers with a repetition of 940 kHz.

5.2 Setup

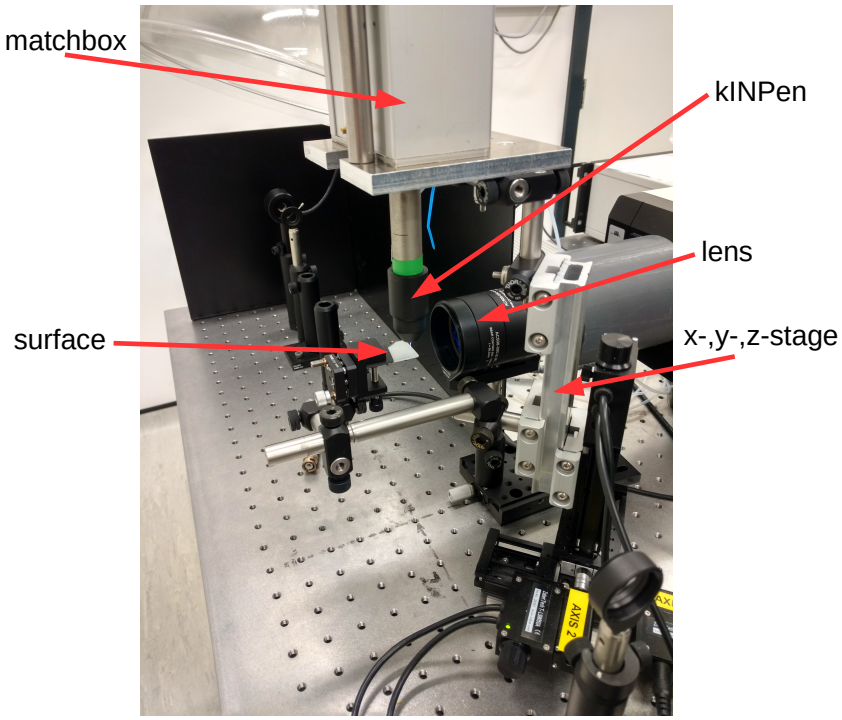

Figure 5.2: Overview of the kINPen TALIF setup.

Figure 5.2 shows the setup used for the kINPen investigation. This is the same picosecond laser setup as in 2.7.2. The jet with the matching box on top is mounted onto a steel plate which is secured with Thorlabs optical poles to the linear actuators (the same Zaber stages as in section 2.7.2). In this configuration, the plasma effluent points downward and the jet can be moved on the x-,y-, and z-axis. The placing of the kINPen and the optics led to a resolution of approximately 104 pixel per mm.

Unfortunately, the fluorescence filter for the TALIF setup does not exclude the argon metastable emission at 811.5 nm. The metastables are produced with every pulse of the discharge and declined exponentially until the next pulse as shown in [165]. This diminishes the signal to noise ratio. It does not effect the absolute number density because it is part of the background that was subtracted.

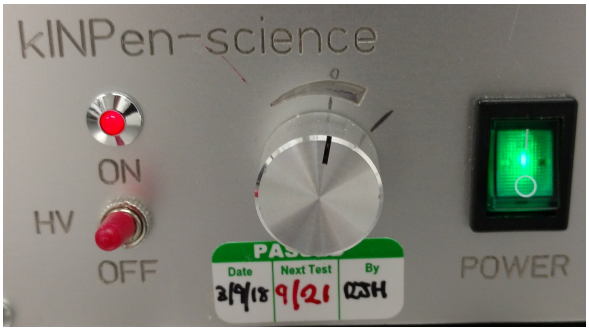

Figure 5.3: The kINPen power supply with markings for the standard setting used in this work.

Figure 5.3 shows the kINPen power supply, which is directly attached to the matching box on top of the plasma jet. Throughout all of the experiments, the setting of the power supply was not changed and remained on the setting visible in figure 5.3. The voltage, current and, thus, power have not been measured at any time.

The gas is supplied by MKS massflow controllers and a MKS massflow controller unit. In order to admix water to the gas, a bubbler system filled with distilled water was used.

Prior to the experiments, the jet and the laser were warmed up for at least 40 minutes. This ensures repeatability of the experiments.

The kINPen med is intended to be used on surfaces such as human skin or photographic plates [15, 162]. The current kINPen med has no gas shielding device and, thus it was not used for this experiment. Figure 5.4 provides a close up of the setup for the surface species experiments in close up. A sanded microscpe slide was used to prevent reflections from the laser or the fluorescence signal. The sanded microscope slide is mounted on the same linear actuator as the kINPen 7 mm below the nozzle exit.

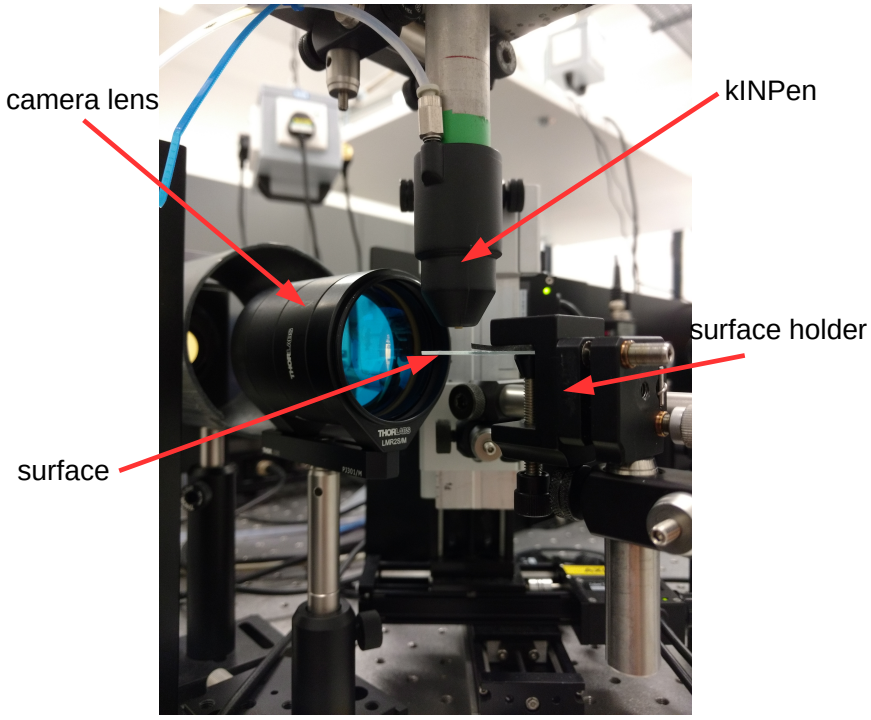

Figure 5.4: Closup of the kINPen setup of the kINPen surface setup

5.3 Effect of the gas curtain

The gas curtain was introduced with the kINPen sci to shield the plasma from uncontrolled environmental air. This allows a more precise control of the plasma chemistry. However, the gas curtain also introduces turbulences and mixes into the plasma [166]. This results in a shorter plasma. The mixing with the gas curtain introduces one more dimension that can be tweaked. One study looked at the hydroperoxyl concentration versus the oxygen concentration in the shielding gas and found that more oxygen in the shielding gas produces more hydroperxyl [167]. However, they have not tested what the difference of other shielding gases are or the effect of having no gas curtain. It has also not been tested how the atomic oxygen concentration is affected by the gas curtain or different shielding gases.

In the following, the effect of the gas curtain on the atomic oxygen density will be presented. After this, the effect of different water admixtures with different shielding gases will be presented.

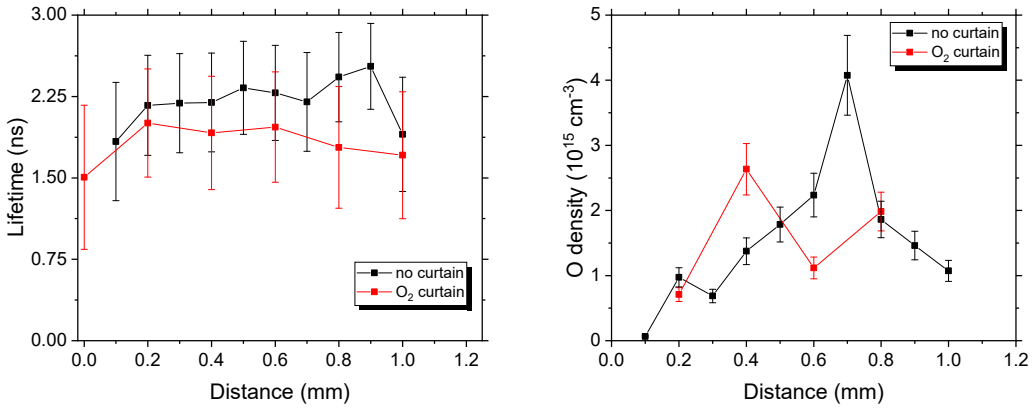

a) b)

Figure 5.5: Lifetimes (a) and densities (b) of atomic oxygen for no gas curtain (black) and an 5 slm oxygen gas curtain (red). Conditions: 3 slm argon flow, 2200 ppm water admixture, power as seen in figure 5.3

Figure 5.5 depicts the effect of an oxygen gas curtain on the plasma. The measurement point is 1 mm below the nozzle exit. The laser was scanned in 0.05 mm (black) and 0.1 mm (red) steps radially through the plasma. The decrease in resolution was done because it was not necessary to scan in 0.05 mm steps. The laser has a diameter of 0.1 mm and 0.05 mm would have let to overlapping measurement points. Additionally, the image from the camera was not sliced and, therefore, it was not accounted for different absorption path lengths through the plasma. This can alter the measured atomic oxygen densities and make them appear too low at the plasma edges. The gas flow for the plasma was 3 slm argon with 2200 ppm water admixture. The gas curtain was 5 slm oxygen. The power was set at the standard setting seen in figure 5.3.

In figure 5.5a the lifetimes for no gas curtain (black) and gas curtain (red) are depicted. One can see that the measurable lifetimes do not span the entire cross section of the effluent. This can be attributed to the low signal to noise ration outside the plasma and, thus, high fitting errors for the lifetimes. This results in unrealistic high lifetimes and the measurement points are not shown in the plot. The lifetime observed for no gas curtain and gas curtain are similar and average around (2.2 ± 0.7) ns. Compared to the natural lifetime of $O(3p\,^3P_J)$ of 35.1 ns the measured lifetimes are approximately 16 times lower, which can be attributed to quenching mainly from water, hydroxyl and oxygen in the plasma.

The absolute atomic oxygen densities are depicted in figure 5.5b. The absolute atomic oxygen densities are depicted in figure 1.5b, with the gas curtain indicated as red and no gas curtain indicated as black. While the densities with the oxygen gas curtain vary around $(2 \pm 1) \cdot 10^{15}\,\mathrm{cm}^{-3}$, the densities without the gas curtain rise asymmetrically from left and right to $(2.0 \pm 0.4) \cdot 10^{15}\,\mathrm{cm}^{-3}$ and then rise to a spike of $(4.0 \pm 0.5) \cdot 10^{15}\,\mathrm{cm}^{-3}$ at 0.7 mm. The

plasma with the gas curtain on is more diffuse than without because gas from the gas curtain is mixed into the plasma. Without the gas curtain, the plasma is not diffusive anymore and has a sharp appearance. This can explain the spike. These results indicate that the gas curtain makes the plasma more diffused and does influence the atomic oxygen lifetimes in a major way. The next step was to investigate the influence of different curtain gases, as this can influence the chemistry heavily.

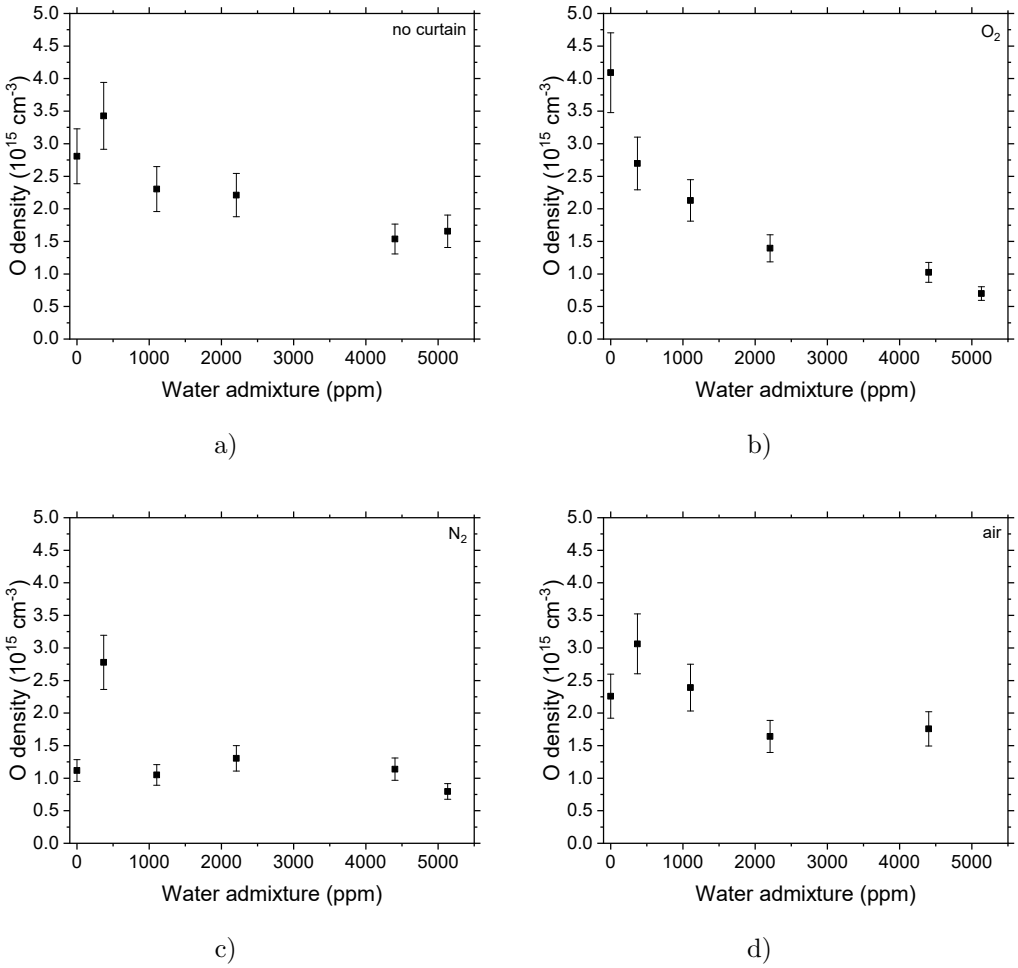

Figure 5.6: Atomic oxygen densities for a) no gas curtain, b) O_2, c) N_2 and d) synthetic air gas curtains. The measurements point is 1 mm below the jet. Conditions: 3 slm total argon flow, 5 slm gas curtain flow and power set as shown in figure 5.3.

Figure 5.6 depicts the water variation for different curtain gases. The measurements were taken 1 mm in front of the nozzle exit. This is the same position as previously used for the cross effluent cross sections. The total argon flow was 3 slm, the water admixture ranged from 0 ppm to 5133 ppm. In the case of a gas curtain, the flow was 5 slm.

In the case of no gas curtain (figure 5.6 a)), adding more water led to a slight increase of atomic oxygen density from $(2.8\pm0.4)\cdot10^{15}$ cm^{-3} at 0 ppm to $(3.4\pm0.5)\cdot10^{15}$ cm^{-3} at 370 ppm.

Further, increasing the water admixture led to a slow declined of the atomic oxygen down to $(1.6 \pm 0.2) \cdot 10^{15}\,\mathrm{cm}^{-3}$ at 5133 ppm.

In the case of the oxygen gas curtain, the atomic oxygen densities start from $(4.1 \pm 0.4) \cdot 10^{15}\,\mathrm{cm}^{-3}$ without water and declined steadily with increasing water admixture. The lowest density was measured at 5133 ppm water admixture with $(0.7 \pm 0.1) \cdot 10^{15}\,\mathrm{cm}^{-3}$. In the case of a nitrogen gas curtain, the densities stay constant between $(0.8 \pm 0.1) \cdot 10^{14}\,\mathrm{cm}^{-3}$ and $(1.3 \pm 0.2) \cdot 10^{14}\,\mathrm{cm}^{-3}$. The only exception is $(2.8 \pm 0.4) \cdot 10^{15}\,\mathrm{cm}^{-3}$ at 370 ppm water admixture. The difference between these curtains is the chemistry. A small water admixture leads to a higher water dissociation in both oxygen and nitrogen cases. While atomic oxygen densities decay slowly with increasing water admixture, with the oxygen curtain the atomic oxygen densities stay constant ,with one exemption, with the nitrogen curtain. This might be a result of the different chemistries of nitrogen, oxygen and water containing plasmas. This is a call for further investigation including measuring other species ,such as atomic hydrogen, and chemical kinetic simulations.

In the scenario of the dry air gas curtain, the atomic oxygen density starts at $(2.3 \pm 0.3) \cdot 10^{15}\,\mathrm{cm}^{-3}$. Admixing water caused the atomic oxygen densities to increase to $(3.0 \pm 0.5) \cdot 10^{15}\,\mathrm{cm}^{-3}$. Increasing the water admixture further resulted in a decrease of atomic oxygen density down to $(1.8 \pm 0.3) \cdot 10^{15}\,\mathrm{cm}^{-3}$. The last point at 5133 ppm is missing because the wavelength scan revealed only noise. The reason for this might be the low signal to noise ratio induced by the visible argon metastables emission at 811.5 nm.

The trend of this variation resembles the trend of the no curtain variation, but shifted down by approximately $0.5 \cdot 10^{15}\,\mathrm{cm}^{-3}$. This indicates that the surrounding air has the same effect on plasma chemistry as the dry air gas curtain. The offset can be attributed to higher turbulences due to the relatively high (5 slm) gas flow around the plasma.

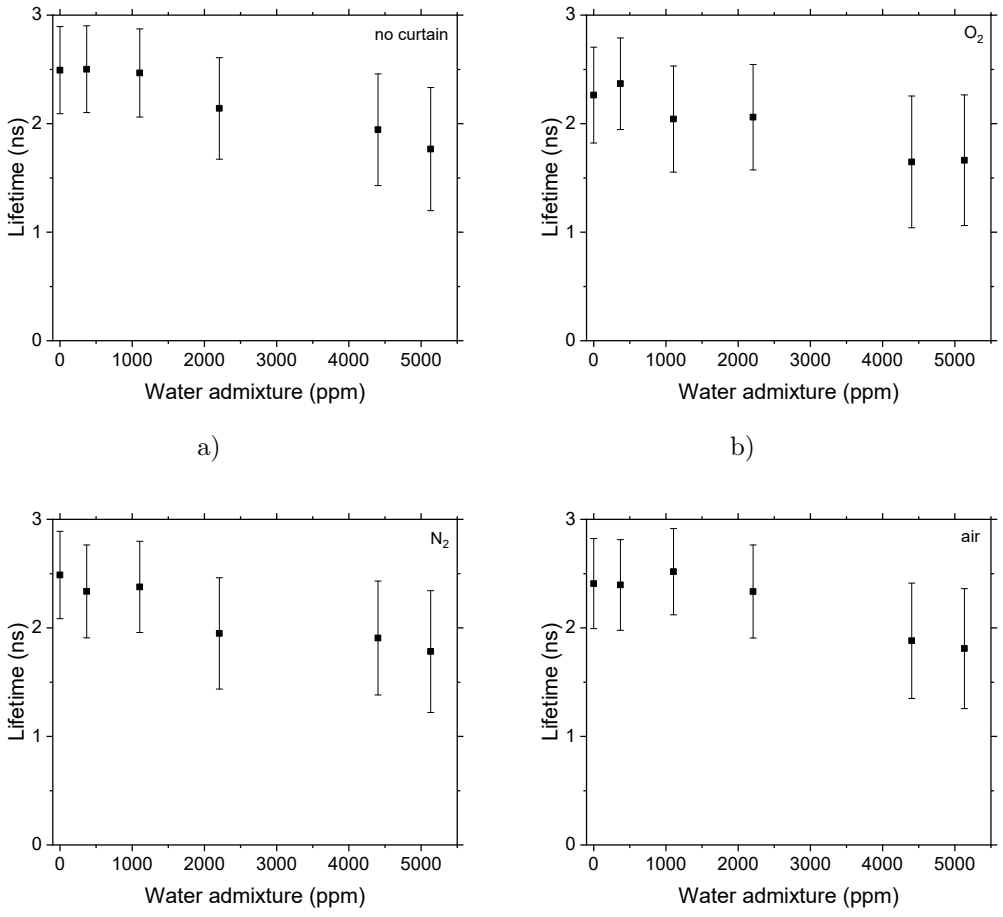

Figure 5.7: Lifetimes of atomic oxygen for a) no gas curtain, b) O_2, c) N_2 and d) synthetic air gas curtains. The measurements point is 1 mm below the jet. Conditions: 3 slm total argon flow, 5 slm gas curtain flow and power set as shown in figure 5.3.

Figure 5.7 shows the lifetimes of the water variation. The same measurement conditions apply as above. All four cases, no curtain, oxygen, nitrogen and air, had very similar trends. Each started at approximately 5 ns and then declined linearly to 3.5 ns. The natural lifetime of atomic oxygen is (34.7 ± 1.7) ns [93]. This suggests that, without water admixture, the main quenching partners are argon and the respective gas curtain gas with a quenching coefficient of $0.25 \cdot \mathrm{cm}^3\,\mathrm{s}^{-1}$ (argon) [132]. The quenching coefficients for nitrogen and oxygen are $5.9 \pm 0.2 \cdot \mathrm{cm}^3\,\mathrm{s}^{-1}$ [168] and $9.4 \pm 0.5 \cdot \mathrm{cm}^3\,\mathrm{s}^{-1}$ [132]. The admixture water changes the lifetimes by 20 % despite the quenching coefficient of $49 \pm 3 \cdot \mathrm{cm}^3\,\mathrm{s}^{-1}$ [90]. This can be explained by the low admixture of water less then 0.5 %.

This shows that admixture of water from the atmosphere in the lab can be neglected and does not influence the measurements as was discussed in [169].

5.4 Surface interactions

Many studies described in [31] only tested various versions of the kINPen in free flow or measure the hydrogen peroxide concentration in an aqueous solution or grow medium. Therefore, it is not known how the reactive species distribution looks like and how the kINPen is able to deliver highly reactive atomic species from the plasma to the surface.

The kINPen med needs a spacer of 7 mm in order to not burn patiences according to Mann et al. [170]. This was the distance the sanded glass microscope slide was placed in order to simulate a surface. The criteria for the surface was that it had to be chemically inert in order to last long enough for the measurements and it has to be matte in order to scatter the laser light. In addition, the matt surface does allow simple temperature measurements with the thermal camera as done in section 3.

a) b)

Figure 5.8: Comparison of the kINPen effluent hitting the glass surface with water admixed a) and without water b) to the argon.

A first assessment of the plasma with dry surface and water admixture and no water admixture can be done by eye. For this, pictures of the plasma were taken with a mobile phone camera (Motorola X Play). Figure 5.8 shows the difference between the a) wet argon plasma and b) dry argon hitting a dry glass surface. The first thing to observe is the difference in colour: the wet plasma inhibits a blue colour while the dry plasma is brighter and purple in colour. Another observation is the higher diffusion of the wet plasma opposed to the sharp plasma edges for dry plasma. Furthermore, the photograph reveals some striations that resembles streamers to the surface.

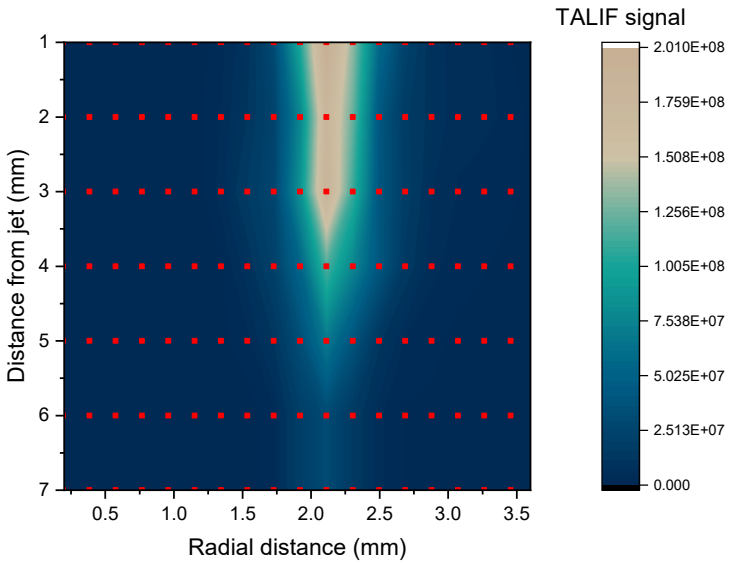

Figure 5.9: The atomic oxygen signal from nozzle to surface. The slice was taken in the middle of the kINPen nozzle. The red squares represent the measurement points. Conditions: 3 slm total argon flow, 2200 ppm water admixture.

In order to see the spatial distribution of atomic oxygen in the wet plasma, a scan through the middle of the effluent from 1 mm to 7 mm from the nozzle was done. 7 mm is the position just over the surface at which the laser is not clipping on the microscope slide. This was checked by eye with a fluorescence card and the laser energy meter behind the microscope slide. The camera image was sliced horizontally in 20 pixel slices and integrated vertically over the laser beam width (20 pixel broad). Figure 5.9 depicts the TALIF signal from bespoke distance variation. The measurement points are depicted as red squares. From 1 mm to 3 mm the signal is strong and declined to half the starting value from 3.5 mm until 4 mm. Above the surface, only a few percentage of the original signal are present. No clipping correction has been done for this plot. The absolute densities could not be calculated because the wavelength scan was noisy below 3 mm distance from the jet. This is probably due to the reduced signal to noise ratio caused by the argon metastable emission at 811.5 nm. The time scan at the maximum wavelength allowed for the atomic oxygen distribution to be plotted. It also allowed for the calculation of the lifetimes of atomic oxygen. It is now known that the atomic oxygen signal are low at the surface. However, not too low to plot the atomic oxygen density across the surface.

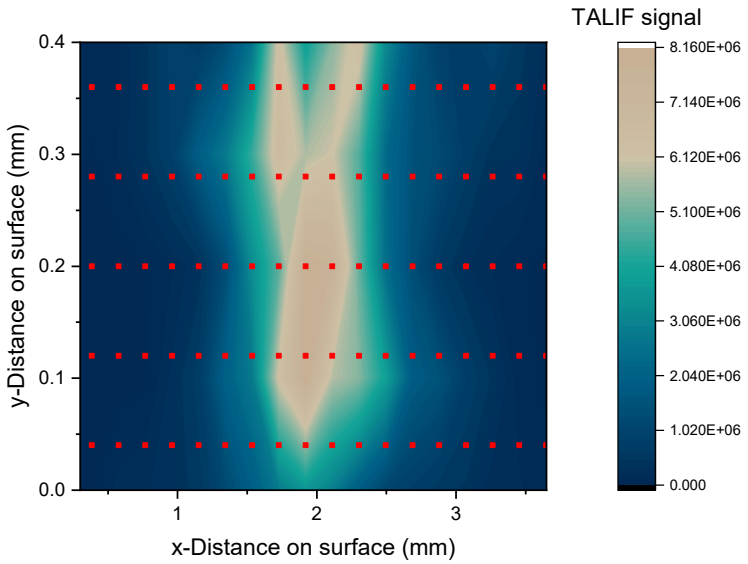

Figure 5.10: Atomic oxygen distribution across the surface. The red squares represent the measurement points. Conditions: 3 slm total argon flow, 2200 ppm water admixture, power see figure 5.3

This was done in figure 5.10. It depicts the TALIF signal of atomic oxygen on the dry surface of the sanded microscope slide. The water admixture was 2200 ppm, the gas curtain is off and the power is as depicted in figure 5.3. The laser was scanned above the surface in 0.1 mm steps. Each image was sliced into 20 pixel horizontally and 20 pixel vertically over the TALIF emission. The measurement points are depicted as red squares.

The TALIF signal maximum is at 2 - 0.15 mm. From there, it decays rapidly, so that the main TALIF signal stays within an area of 1 mm by 0.4 mm. This is also what can be expected from figure 5.5 and 5.8a . The two arms extending to the top are remnants of the filamentary structure of the plasma.

The laser beam is approximately 100 µm in diameter and right above the surface. Thus, it is very likely to show the atomic oxygen directly above the surface. This shows that the atomic oxygen distribution does not protrude beyond the nozzle width of 1.6 mm.

This leads to speculation regarding how the atomic oxygen distribution on the surface compare to the distribution further up. One could expect that atomic oxygen distribution flattens out directly above the surface and is more contracted and concentrated further up. This was tested for the same setup as above for dry and wet surfaces.

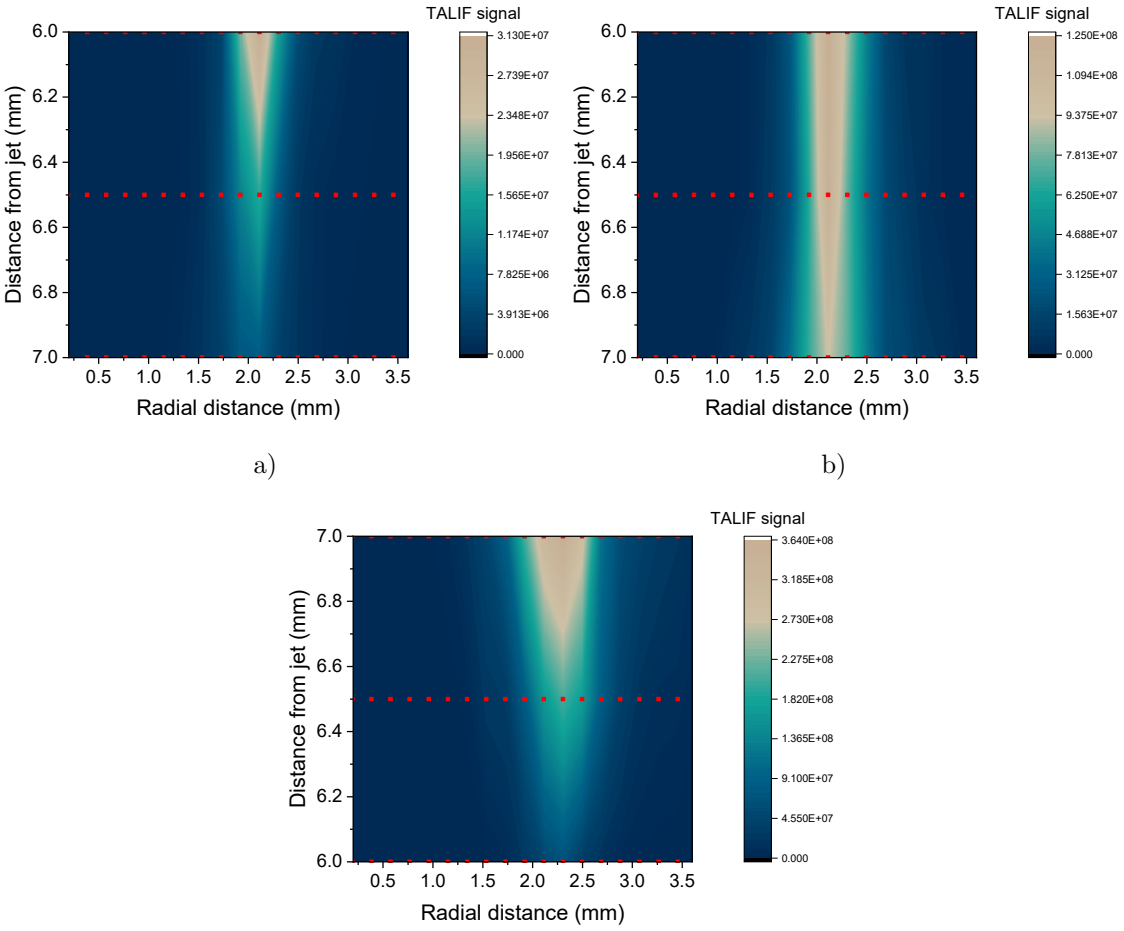

Figure 5.11: TALIF signal for a plasma with 2200 ppm water admixture (a)-b)) and no water admixture in the plasma c) above a dry surface (a), c)) and a wet surface b). The red squares represent the measurement points.

Figure 5.11 depicts the TALIF signal close to the surface for three different cases. The images were produced as described above for 7 mm, 6.5 mm, and 6 mm from the jet. 7 mm is directly above the surface. No correction for clipping has been applied. This does not matter for this comparison because all distances from the surface are the same for every sub-figure. The measurement points are depicted as red squares.

The first case a) depicts the TALIF signal for a plasma with 2200 ppm water admixture and a dry surface. The surface is a sanded microscope slide. The effluent is centred around 2.1 mm. This is the same as in figure 5.10. The signal declined between 6 mm and 6.4 mm from the maximum of $3.1 \cdot 10^7$ to a third of it's value. From 6.4 mm to the surface, the signal declined to a third of the original intensity. As no clipping correction had been applied, this image had to be compared to other cases with the same conditions in order to gain knowledge.

Case b) depicts the same plasma but with a wet surface. The wet surface was realised by placing a blue paper towel on the microscope slide and wetting it periodically (every 60 s) with distilled water. This is needed because the gas flow of the jet dried out the wetted paper.

The maximum signal is $1.2 \cdot 10^8$ and declined slowly to $0.9 \cdot 10^8$ above the surface. The atomic oxygen formed a tub that reaches the surface. Compared with case a) this suggested that more atomic oxygen reached the surface. One possible explanation for this might be the higher humidity content in the micro environment around the plasma. Thus, more water is re-fed into the effluent to produce more atomic oxygen.

Case c) depicts the case of a dry plasma and dry surface. In this case, the signal is three times higher than in the previous cases. The atomic oxygen profile is similar to case a). The majority of the signal declined between 7.0 mm and 6.4 mm to half of the signal and then to a third of the starting signal at the surface. Taking into consideration that the signal intensity is much higher than in case a) and b), more atomic oxygen might have reached or was created on the surface.

For this study, it is not known what the power dissipated by the plasma was. This might render these studies not directly comparable to the kINPen med. Especially the high temperature of the glass during this studies might indicate that the power setting was too high for sensitive surface such as plastics, bacteria or skin.

However, these results indicate that wet surfaces have an influence on the kINPen plasma likely influencing the chemistry and, thus, the reactive particles delivered to the surface.

5.5 Summary

In this chapter, TALIF has been utilised to investigate the effect of different gas curtains on the atomic oxygen densities in the plasma of the kINPen sci.

Effect of gas curtain The effects of the gas curtain on the atomic oxygen density were investigated by comparing cross sections of the effluent with an oxygen gas curtain and without a gas curtain. The results indicate that in the case of no gas curtain, the atomic oxygen is asymmetrically distributed. Introducing the oxygen gas curtain makes the discharge narrower and evens out the atomic oxygen densities. The introduction of the gas curtain does not significantly change the lifetimes of atomic oxygen. The lifetimes decrease from an average of 2.25 ns to 1.87 ns. At all times, the lifetimes lie within error bars.

The effect of the gas curtain versus the water content has been tested against no gas curtain, oxygen, nitrogen and synthetic air. The synthetic air gas curtain reveals the same trend as no gas curtain. Due to more turbulence caused by the gas curtain, the densities are 20 % lower.

In the case of the oxygen gas curtain, increasing the water admixture led to a linear decline of atomic oxygen because it reacts strongly with the water and species produced in the plasma.

The nitrogen gas curtain reveals a baseline density of $(6.3 \pm 0.9) \cdot 10^{14}\,\mathrm{cm}^{-3}$ and a peak at 370 ppm water admixture with a height of $(1.3 \pm 0.2) \cdot 10^{15}\,\mathrm{cm}^{-3}$ cm atomic oxygen. This peak is at the same position as in the synthetic air and no gas curtain case, suggesting that at this point the chemistry might be related to stoichiometry or an interference in the florescence signal occurs. This presents an opportunity for future research.

Surface interactions The TALIF signal of the effluent of the kINPen 7 mm in front of a surface has been measured. Due to the low signal strength, only the time series presented useable data that can represent the atomic oxygen distribution in a qualitative manner.

It was found that the atomic oxygen density rapidly declined in the first 3 mm after the jet. After comparing wet and dry surfaces, it was found that a wet surface increases the atomic oxygen density above the surface. This might be due to higher humidity in the micro-environment of the effluent above the surface or higher plasma power due to a different electrical environment because the water has more electrical capacitance then a dry surface or a combination of both effects. Further research should be undertaken in this area because it represents the interface between gas and liquid and is a very important zone for the development of reactive species.

Chapter 6

Summary and conclusion

Multiple objectives have been identified in chapter 1 for this work. The first objective was to test if the COST jet is a viable reference source for completing fundamental research on APPJs. For this, four COST jets have been tested for reproducibility. The parameters were dissipated power, emission spectroscopy, gas temperature, ozone and atomic oxygen production, as well as bacterial inactivation. The deviation was below 15 % for all measured quantities. The voltage power characteristics revealed a deviation of up to 15 % with most of this being related to the limited accuracy of the measurements as was shown in a recent paper [171]. The gas temperature, a vital parameter for temperature-sensitive and biological samples, revealed a difference below 3 % across all the devices. This is valid for both, the gas temperature and the surface temperature on a sanded glass slide. It was also shown that the temperature profile and the maximum temperature did not vary much during a distance variation. The main knowledge results from the temperature versus plasma power graph figure 3.1b. From this, one can derive an upper plasma power limit of 0.3W for which the temperature did not exceed 37 °C. This prevents bacteria from being burned and the effects of plasma generated species can be observed in isolation. The other vital parameter is the production of ozone and atomic oxygen. Both species were measured for power from 0.2 W to 1.0 W. The standard deviation for the ozone densities is a maximal of 3 % and thus smaller than the power uncertainty. The atomic oxygen production standard deviation is 8 % below 0.5 W and 13 % above. It is not known why this jump occurs. At 0.3 W the atomic oxygen density is $4 \cdot 10^{20}\,\mathrm{m}^{-3}$ and the ozone density $1.2 \cdot 10^{21}\,\mathrm{m}^{-3}$. The deviations are a mixture of experimental deviation and precision. However, the experimental deviations for the atomic oxygen measurements are likely higher than the differences from the jets. The bacterial inactivation assay showed that the log reduction deviation for one jet is greater than the difference between the jets. This indicates that the jets are comparable in biological experiments. In conclusion, the COST Reference Microplasma Jet is a simple, inexpensive and robust plasma source. Results obtained with different devices consistently show less than 15 % differences when power is used as the control parameter. This makes the COST

jet design a suitable candidate for a reference source to compare the results obtained in different laboratories and accelerate the advancement of research on atmospheric plasmas faster. Smaller improvements could be done to make power measurements easier as was previously discussed in [106].

The second and third objectives were to measure hydrogen peroxide, hydroxyl and atomic oxygen with new or improved optical diagnostic methods and identify a method in which to tailor the production of reactive species in the plasma. This was done for water containing plasmas, as well as water and oxygen-containing plasma. Hydrogen peroxide densities have been measured by FTIR and PDLIF in the gas phase in the far effluent (80 cm after the plasma) on the modified COST jet. For the water variation, both measurement methods agreed in the trend, but the PDLIF values were three times lower. The trend exhibited an increase in hydrogen peroxide until 4000 ppm water admixture. Increasing the water admixture further led to a slow saturation of hydrogen peroxide production. The trend might be slightly caused by a variation in power as the voltage was kept constant. The difference between FTIR and PDLF can be explained due to difficulties in measuring very low hydroxyl concentrations accurately. However, the agreement in the trend shows that PDLIF is a viable option for measuring hydrogen peroxide in the effluent of an APPJ if the sensitivity could be increased and more stable lasers would be used. Additionally, an intensified camera may be beneficial to aid spatial resolution. The FTIR measurements acted as a benchmark in this case and are deemed to be more reliable. This proof of concept expands the pool of measurement techniques to do science on atmospheric plasmas.

The water and voltage variation on the same jet, as measured with FTIR, revealed that the hydrogen peroxide densities at low water admixture increased linearly with voltage. However, increasing the water admixture led to a saturation effect as previously discussed. Adding small amounts of oxygen to the water-containing plasma produced twice as much hydrogen peroxide than without. The hydrogen peroxide production is only weakly coupled to the oxygen admixture, once it had been added. The ozone concentration had been measured at the same position after the plasma with an ozone meter. These measurements revealed that an increase in oxygen admixture led to an exponential growth of ozone concentration. Absorption measurements in the plasma showed that the hydroxyl concentrations follow the same trend as the hydrogen peroxide densities in the far effluent. The water admixture led to an increase of hydrogen peroxide production efficiency from hydroxyl from 55 % to 88 %. Because the atomic oxygen densities could not be measured inside or in the far effluent of the plasma, they have been measured directly in front of the COST jet. These measurements reveal that the atomic oxygen density increased linearly until 3000 ppm oxygen admixture before the plasma extinguishes. Temperature measurements from hydroxyl absorption measurements reveal that the plasma temperature did not change significantly for the oxygen variation. This had not been shown before and opens the possibility to tailor the plasma

further in terms of atomic oxygen, ozone, hydroxyl and hydrogen peroxide production without the need for multiple frequencies or pulsed plasma operation. By adding these methods, the plasma might be tailored even further. Mixing other gases to the water admixture, for example nitrogen, might open pathways to other chemistries. This had been considered in this work, but many nitrogen compounds that might be produced are toxic in small doses and might not be suitable for biomedical applications. However, further research for other fields might bring fruitful results.

More measurements with PDLIF had been done on the COST jet in the effluent 9 mm from the electrodes. The water variation exhibits large error bars on the hydrogen peroxide concentration, rendering it difficult to speculate on the hydrogen peroxide trend. For this, a hydroxyl LIF laser with less noise would have been beneficial. The oxygen variation with fixed water admixture did not yield usable results because of ozone interference as discussed previously. The same can be said regarding the water variation with fixed oxygen admixture. The distance variation from 9 mm to 29 mm after the electrodes reveals an unvarying hydrogen peroxide concentration for both total helium flow cases. To place this result, the findings of the hydroxyl distance variation have to be taken into account.

The LIF hydroxyl measurements for the water admixture were completed 9 mm away from the electrodes on the COST jet and showed that the hydroxyl densities rise fast with water admixture to a maximum at 1100ppm, before slowly declining in a linear manner. For the oxygen variation with fixed water content, the hydroxyl densities follow the same trend as the hydroxyl densities measured in the plasma with the modified COST jet.

The distance variation from 9 mm to 29 mm with only water admixed reveals that the hydroxyl concentrations exponentially decays with increasing distance to the jet. The hydroxyl concentrations are a few magnitudes lower than the hydrogen peroxide concentrations. Thus, the hydrogen peroxide must have been primarily generated before the 9 mm distance.

Cross-sections of the effluent at 9 mm, 15 mm and 25 mm showed that the hydroxyl stayed within a narrow gas channel. The gas channel shape had been confirmed by using *tert*-Butyl peroxide as a tracer substance. Moreover, the gas channel profile was comparable to the heat profile on a surface measured for the COST jet comparison. In conclusion, the effluent was a narrow channel, as previously suggested by Schlieren photography and simulations. The above results underline this and show that the reactive species or chemicals do not diffuse out of this channel. However, the hydroxyl LIF results show another possibility to tailor the delivered reactive species by changing the position of the plasma jet. Further studies, with a less noisy LIF laser and a smaller photodissociation laser beam, would be needed to complete the data from the tip of the jet until 9 mm. As the interface of the plasma effluent and the target is a very important zone further studies with this technique would further complete the understanding of plasma target interaction.

PDLIF is a new technique to use on APPJs, which has been adapted from atmospheric

chemistry and combustion science. The use of two lasers also allowed for the use of tert-butyl hydroperoxide as a tracing agent to make gas stream visible and, more importantly, as a calibration method for the hydroxyl measurements. This had not been done previously and this method, with a pico second laser to resolve smaller lifetimes and a smaller photodissociation laser beam, might be, in limits, more versatile for measuring hydroxyl and hydrogen peroxide densities in the effluent of the plasma jet than mass spectrometry or long path absorption cells.

Atomic oxygen was measured with TALIF on an application-oriented plasma jet, the kINPen. This jet has a gas curtain that can be operated with different gases. First, the effect of the gas curtain was investigated. For this, the atomic oxygen was measured for a transverse cross-section of the kINPen effluent 1 mm in front of the nozzle. This revealed, that the gas curtain only had a minor influence on the atomic oxygen lifetimes and atomic oxygen densities. A frontal cross-section was done without the gas curtain and with a surface 7 mm in front of the jet. This revealed that the atomic oxygen signal was only strong until 4mm after the jet. Below this point, lens shading effects might play a roll and reduce the amount of fluorescent signal. Nonetheless, this is an important result that shows that atomic oxygen, a short lived and highly reactive species, might not play as big as a role as for example, hydrogen might. However, this would have to be confirmed by other measurements. This had not been done with a pico second laser in uncontrolled air before.

A water variation was done with no, nitrogen, oxygen and synthetic air gas curtain. This revealed that no gas curtain and synthetic air gas curtain had the same effect suggesting that impurities from the surrounding air did not have much influence on the atomic densities. A conspicuous atomic oxygen peak at 370 ppm water admixture for no, air and nitrogen gas curtain occurred which had not been seen before. It would be interesting to examine the chemistry at this point in detail. Further power measurements would be needed to explain if this effect is purely chemical or related to power changes through added water in the plasma. For this, a model with accurate water and nitrogen chemistry would be beneficial. But to date, no accurate nitrogen model has been published. The above results add more insight to the plasma chemistry of the kINPen and allow, with more measurements of other plasma species, to tailor the plasma chemistry even more than is done until now. As the surrounding air did not seem to have a big influence on the water containing plasma, the gas curtain might be omitted completely if desirable. Further studies should be made to investigate the possibility of admixing oxygen or nitrogen directly to the water containing plasma as was done with the COST jet in this work.

The atomic oxygen signal directly above a dry and a wet surface was also measured for the first time for this jet. The sanded microscope slide was mounted 7 mm away from the jet and the water admixture 2200 ppm and no gas curtain in order to simulate a use case scenario. These parameters were chosen, not only because the kINPen med does not have

the gas curtain, but also because it is the only medically accredited plasma jet.

The measurements revealed that a wet surface can alter the atomic oxygen signal. This can possibly be explained by the higher water concentration in the micro-environment around the plasma of the kINPen or a change in plasma power due to a changed electrical environment showing the disadvantage of pulsed DC plasma jets for applications with changing electrical environments. It would be interesting to make changes in the setup to get absolute atomic oxygen densities for this measurement. For this, a different mounting of the jet and surface are needed in order to achieve higher fluorescence signal strength. Accurate power measurements would also be important to explain the changes. This would add more value to the understanding of the plasma target interface.

In conclusion, this work established that the COST jet is a viable reference source and, thus, has the ability to propel research on atmospheric pressure plasmas further and possibly faster. Moreover, PDLIF was introduced as a new measurement technique for atmospheric pressure plasma jets and the possibility to easily tailor the plasma chemistry by mixing several molecular gases to the plasma. Furthermore in this work, a better understanding of the plasma effluent of the COST jet has been established through PDLIF.

Further investigations should include more chemistry simulations and other molecular gas admixtures in conjunction with water. More stable lasers to use with PDLIF would be beneficial for a better signal to noise ratio and a smaller photodissociation laser beam to study the gas surface interface. Especially PDLIF with different wavelength can be used to study other reactive species in the effluent.

The kINPen investigations showed a great potential to tailor the plasma chemistry but was limited to measure atomic oxygen. Other species, such as atomic nitrogen or atomic hydrogen, should be measured too in order to better understand the plasma of the kINPen with and without gas curtain. The plasma to target interface was investigated and revealed differences between dry and wet surfaces. This study could be improved by bettering the signal to noise ratio through changes in the setup and having more time to use the setup. The use of 2D or 3D simulations would aid this study to better understand the spatial distribution of reactive species.

Appendix A

Agar surface temperatures

The surface temperature is very important for biological experiments. In these experiments it is desirable to investigate the effects of the plasma without deactivating the specimens with too much heat. To treat bacteria, agar plates are usually used. These contain water which can evaporate or transport heat efficiently.

For this, agar plates without cell cultures were treated with an earlier version of the COST jet and the surface temperature was recorded with a thermal camera (see figure A.1). The distance between the agar and the electrodes was 10 mm and the maximum treatment time 190 s. The plasma parameter were 1 slm helium flow and 0.5 % oxygen admixture.

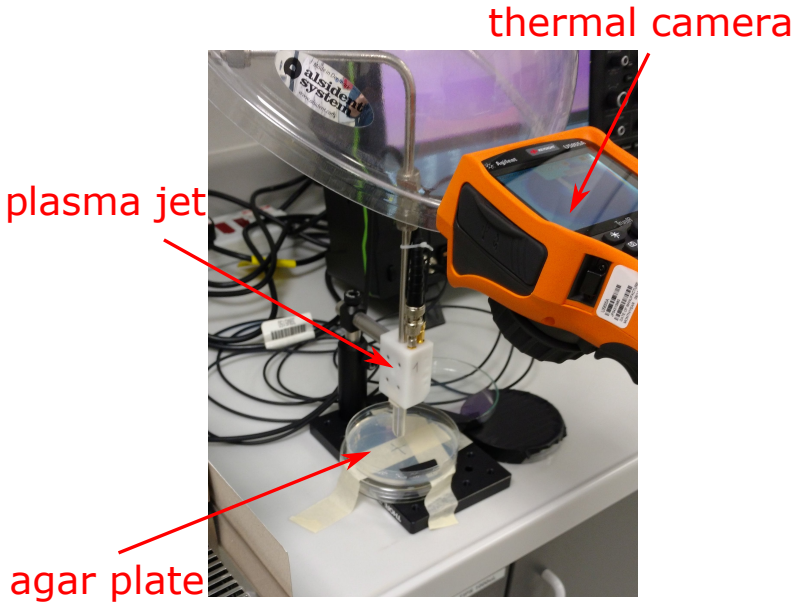

Figure A.1: Experimental setup to measure the agar surface temperature.

The jet was warmed up and the agar plates were placed under the jet. The first thermal

image was taken immediately after the agar plate was placed under the plasma.

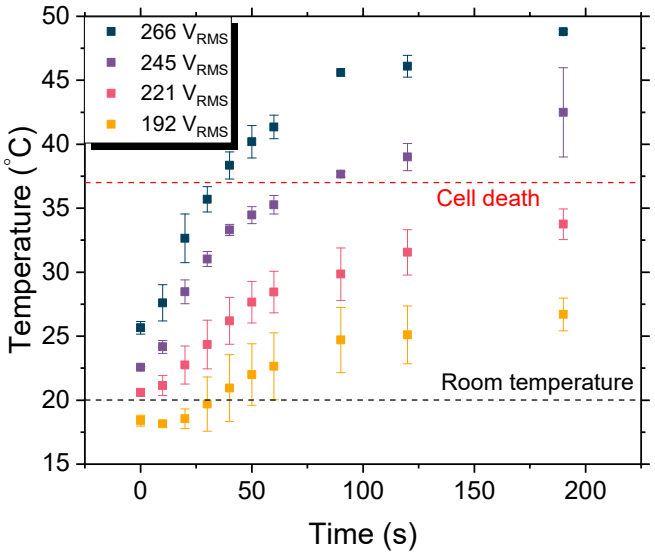

Figure A.2: Agar surface temperature over time for different voltages. Conditions: 1 slm helium, 5 sccm oxygen.

Figure A.2 depicts the agar surface temperature for four different voltages versus time. Additionally, the room temperature and the cell death temperature of 37°C are depicted. For lower voltages, the temperature stays close or below room temperature for up to 40 seconds. This shows the evaporative cooling effect. Additionally, the surface temperature stays below 37°C. For the higher higher voltages, the evaporative cooling is not strong enough and the surface temperature quickly reaches 37°C in 75 s (245 V_{RMS}) and 45 s (266 V_{RMS}).

List of References

[1] S. Schröter, et al. Chemical kinetics in an atmospheric pressure helium plasma containing humidity. *Physical Chemistry Chemical Physics*, 20(37):24263, 2018.

[2] A. M. Hirst, M. S. Simms, V. M. Mann, N. J. Maitland, D. O'Connell, and F. M. Frame. Low-temperature plasma treatment induces DNA damage leading to necrotic cell death in primary prostate epithelial cells. *British journal of cancer*, 112(9):1536, 2015.

[3] A. Privat-Maldonado, D. O'Connell, E. Welch, R. Vann, and M. W. Van Der Woude. Spatial Dependence of DNA Damage in Bacteria due to Lowerature Plasma Application as Assessed at the Single Cell Level. *Scientific Reports*, 6(1):35646, 2016.

[4] M. Laroussi. Nonthermal decontamination of biological media by atmospheric-pressure plasmas: Review, analysis, and prospects. *IEEE Transactions on Plasma Science*, 30(4 I):1409, 2002.

[5] A. M. Hirst, F. M. Frame, M. Arya, N. J. Maitland, and D. O'Connell. Low temperature plasmas as emerging cancer therapeutics: the state of play and thoughts for the future. *Tumor Biology*, 37(6):7021, 2016.

[6] C. a. J. van Gils, S. Hofmann, B. K. H. L. Boekema, R. Brandenburg, and P. J. Bruggeman. Mechanisms of bacterial inactivation in the liquid phase induced by a remote RF cold atmospheric pressure plasma jet. *Journal of Physics D: Applied Physics*, 46(17):175203, 2013.

[7] K.-D. Weltmann, R. Brandenburg, T. von Woedtke, J. Ehlbeck, R. Foest, M. Stieber, and E. Kindel. Antimicrobial treatment of heat sensitive products by miniaturized atmospheric pressure plasma jets (APPJs). *Journal of Physics D: Applied Physics*, 41(19):194008, 2008.

[8] M. Y. Alkawareek, Q. T. Algwari, S. P. Gorman, W. G. Graham, D. O'Connell, and B. F. Gilmore. Application of atmospheric pressure nonthermal plasma for the in vitro eradication of bacterial biofilms. *FEMS Immunology and Medical Microbiology*, 65(2):381, 2012.

[9] Y. Gorbanev, D. O'Connell, and V. Chechik. Non-Thermal Plasma in Contact with Water: The Origin of Species. *Chemistry - A European Journal*, 22(10):n/a, 2016.

[10] B. Barwe, F. Riedel, O. E. Cibulka, I. Pelant, and J. Benedikt. Silicon nanoparticle formation depending on the discharge conditions of an atmospheric radio-frequency driven microplasma with argon/silane/hydrogen gases. *Journal of Physics D: Applied Physics*, 48(31):314001, 2015.

[11] D. Mariotti and R. M. Sankaran. Microplasmas for nanomaterials synthesis. *Journal of Physics D: Applied Physics*, 43(32):323001, 2010.

[12] J. Benedikt, V. Raballand, A. Yanguas-Gil, K. Focke, and A. von Keudell. Thin film deposition by means of atmospheric pressure microplasma jet. *Plasma Physics and Controlled Fusion*, 49(12B):B419, 2007.

[13] A. West, M. Van Der Schans, C. Xu, M. Cooke, and E. Wagenaars. Fast, downstream removal of photoresist using reactive oxygen species from the effluent of an atmospheric pressure plasma Jet. *Plasma Sources Science and Technology*, 25(2):02LT01, 2016.

[14] D. Shaw, A. West, J. Bredin, and E. Wagenaars. Mechanisms behind surface modification of polypropylene film using an atmospheric-pressure plasma jet. *Plasma Sources Science and Technology*, 25(6):065018, 2016.

[15] M. Boselli, C. Chiavari, V. Colombo, M. Gherardi, C. Martini, and F. Rotundo. Atmospheric pressure non-equilibrium plasma cleaning of 19th century daguerreotypes. *Plasma Processes and Polymers*, 14(3):1600027, 2017.

[16] X. Liao, D. Liu, Q. Xiang, J. Ahn, S. Chen, X. Ye, and T. Ding. Inactivation mechanisms of non-thermal plasma on microbes: A review. *Food Control*, 75:83, 2017.

[17] V. Karanassios. Microplasmas for chemical analysis: Analytical tools or research toys? *Spectrochimica Acta - Part B Atomic Spectroscopy*, 59(7):909, 2004.

[18] D. O'Connell, L. J. Cox, W. B. Hyland, S. J. McMahon, S. Reuter, W. G. Graham, T. Gans, and F. J. Currell. Cold atmospheric pressure plasma jet interactions with plasmid DNA. *Applied Physics Letters*, 98(4), 2011.

[19] J.-W. W. Lackmann, S. Schneider, E. Edengeiser, F. Jarzina, S. Brinckmann, E. Steinborn, M. Havenith, J. Benedikt, and J. E. Bandow. Photons and particles emitted from cold atmospheric-pressure plasma inactivate bacteria and biomolecules independently and synergistically. *Journal of the Royal Society, Interface / the Royal Society*, 10(89):20130591, 2013.

[20] S. Schneider, J.-W. Lackmann, D. Ellerweg, B. Denis, F. Narberhaus, J. E. Bandow, and J. Benedikt. The Role of VUV Radiation in the Inactivation of Bacteria with an Atmospheric Pressure Plasma Jet. *Plasma Processes and Polymers*, 9(6):561, 2012.

[21] E. Wagenaars, M. Van Der Woude, and R. Vann. An atmospheric-pressure low-temperature plasma jet for growth inhibition of Escherichia coli. *IEEE Transactions on Plasma Science*, 39(11 PART 1):2346, 2011.

[22] M. Moisan, J. Barbeau, S. Moreau, J. Pelletier, M. Tabrizian, and L. Yahia. Low-temperature sterilization using gas plasmas: A review of the experiments and an analysis of the inactivation mechanisms. *International Journal of Pharmaceutics*, 226(1-2):1, 2001.

[23] M. Laroussi. Low-Temperature Plasma Jet for Biomedical Applications: A Review. *IEEE Transactions on Plasma Science*, 43(3):703, 2015.

[24] A. Privat-Maldonado, D. O'Connell, E. Welch, R. Vann, M. W. van der Woude, D. O'Connell, E. Welch, R. Vann, and M. W. van der Woude. Spatial Dependence of DNA Damage in Bacteria due to Lowerature Plasma Application as Assessed at the Single Cell Level. *Scientific Reports*, 6(1):35646, 2016.

[25] A. West, M. van der Schans, C. Xu, M. Cooke, and E. Wagenaars. Fast, downstream removal of photoresist using reactive oxygen species from the effluent of an atmospheric pressure plasma Jet. *Plasma Sources Science and Technology*, 25(2):02LT01, 2016.

[26] A. Indarto, D. R. Yang, J. W. Choi, H. Lee, and H. K. Song. Gliding arc plasma processing of CO2 conversion. *Journal of Hazardous Materials*, 146(1-2):309, 2007.

[27] C. J. Liu, G. H. Xu, and T. Wang. Non-thermal plasma approaches in CO_2 utilization. *Fuel processing technology*, 58(2):119, 1999.

[28] J. Winter, R. Brandenburg, and K.-D. Weltmann. Atmospheric pressure plasma jets: an overview of devices and new directions. *Plasma Sources Science and Technology*, 24(6):064001, 2015.

[29] A. Schmidt-Bleker, R. Bansemer, S. Reuter, and K. D. Weltmann. How to produce an NO_x- instead of O_x-based chemistry with a cold atmospheric plasma jet. *Plasma Processes and Polymers*, 13(11):1118, 2016.

[30] A. Privat-Maldonado, et al. Non-target Biomolecules Alter Macromolecular Changes Induced by Bactericidal Low-temperature Plasma. *IEEE Transactions on Radiation and Plasma Medical Sciences*, 2(2):1, 2017.

[31] S. Reuter, T. von Woedtke, and K.-D. Weltmann. The kINPen—a review on physics and chemistry of the atmospheric pressure plasma jet and its applications. *Journal of Physics D: Applied Physics*, 51(23):233001, 2018.

[32] A. Sobota, O. Guaitella, and A. Rousseau. The influence of the geometry and electrical characteristics on the formation of the atmospheric pressure plasma jet. *Plasma Sources Science and Technology*, 23(2):025016, 2014.

[33] V. V. V. Kovačević, et al. The effect of liquid target on a nonthermal plasma jet – imaging, electric fields, visualization of gas flow and optical emission spectroscopy. *Journal of Physics D: Applied Physics*, 51(6):0, 2018.

[34] S. Yonemori and R. Ono. Flux of OH and O radicals onto a surface by an atmospheric-pressure helium plasma jet measured by laser-induced fluorescence. *Journal of Physics D: Applied Physics*, 47(12):125401, 2014.

[35] T. Darny, J. M. Pouvesle, J. Fontane, L. Joly, S. Dozias, and E. Robert. Plasma action on helium flow in cold atmospheric pressure plasma jet experiments. *Plasma Sources Science and Technology*, 26(10), 2017.

[36] J. Golda, et al. Concepts and characteristics of the 'COST Reference Microplasma Jet'. *Journal of Physics D: Applied Physics*, 49(8):084003, 2016.

[37] A. Wijaikhum, D. Schröder, S. Schröter, A. R. Gibson, K. Niemi, J. Friderich, A. Greb, V. Schulz-von der Gathen, D. O'Connell, and T. Gans. Absolute ozone densities in a radio-frequency driven atmospheric pressure plasma using two-beam UV-LED absorption spectroscopy and numerical simulations. *Plasma Sources Science and Technology*, 26(11):115004, 2017.

[38] N. Knake and V. Schulz-Von Der Gathen. Investigations of the spatio-temporal build-up of atomic oxygen inside the micro-scaled atmospheric pressure plasma jet. *European Physical Journal D*, 60(3):645, 2010.

[39] E. Wagenaars, T. Gans, D. O'Connell, and K. Niemi. Two-photon absorption laser-induced fluorescence measurements of atomic nitrogen in a radio-frequency atmospheric-pressure plasma jet. *Plasma Sources Science and Technology*, 21(4):042002, 2012.

[40] D. Maletić, N. Puač, S. Lazović, G. Malović, T. Gans, V. Schulz-von der Gathen, and Z. L. Petrović. Detection of atomic oxygen and nitrogen created in a radio-frequency-driven micro-scale atmospheric pressure plasma jet using mass spectrometry. *Plasma Physics and Controlled Fusion*, 54:124046, 2012.

[41] S. Schröter, et al. Atomic oxygen and hydroxyl density measurements in an atmospheric pressure RF-plasma with water admixtures using UV and synchrotron VUV absorption spectroscopy. In *22nd International Symposium on Plasma Chemistry*. Antwerp, Belgium, 2015.

[42] T. Murakami, K. Niemi, T. Gans, D. O'Connell, and W. G. Graham. Afterglow chemistry of atmospheric-pressure helium–oxygen plasmas with humid air impurity. *Plasma Sources Science and Technology*, 23(2):025005, 2014.

[43] K. Niemi, S. Reuter, L. M. Graham, J. Waskoenig, N. Knake, V. S.-v. der Gathen, and T. Gans. Diagnostic based modelling of radio-frequency driven atmospheric pressure plasmas. *Journal of Physics D: Applied Physics*, 43(12):6pp, 2010.

[44] J. Waskoenig, K. Niemi, N. Knake, L. M. Graham, S. Reuter, V. Schulz-von der Gathen, and T. Gans. Atomic oxygen formation in a radio-frequency driven micro-atmospheric pressure plasma jet. *Plasma Sources Science and Technology*, 19:045018, 2010.

[45] D. B. Graves. The emerging role of reactive oxygen and nitrogen species in redox biology and some implications for plasma applications to medicine and biology. *Journal of Physics D: Applied Physics*, 45(26):263001, 2012.

[46] M. J. Pavlovich, H.-W. Chang, Y. Sakiyama, D. S. Clark, and D. B. Graves. Ozone correlates with antibacterial effects from indirect air dielectric barrier discharge treatment of water. *Journal of Physics D: Applied Physics*, 46(14):145202, 2013.

[47] J. S. Oh, E. J. Szili, N. Gaur, S. H. Hong, H. Furuta, H. Kurita, A. Mizuno, A. Hatta, and R. D. Short. How to assess the plasma delivery of RONS into tissue fluid and tissue. *Journal of Physics D: Applied Physics*, 49(30), 2016.

[48] M. J. Traylor, M. J. Pavlovich, S. Karim, P. Hait, Y. Sakiyama, D. S. Clark, and D. B. Graves. Long-term antibacterial efficacy of air plasma-activated water. *Journal of Physics D: Applied Physics*, 44(47):472001, 2011.

[49] A. Bogaerts, J. Van der Paal, S. Dewilde, W. Van Boxem, and Y. Gorbanev. Reaction of chloride anion with atomic oxygen in aqueous solutions: can cold plasma help in chemistry research? *Physical Chemistry Chemical Physics*, 21(8):4117, 2019.

[50] V. M. Dcosta, et al. Antibiotic resistance is ancient, 2011.

[51] N. Høiby, T. Bjarnsholt, M. Givskov, S. Molin, and O. Ciofu. Antibiotic resistance of bacterial biofilms. *International Journal of Antimicrobial Agents*, 35(4):322, 2010.

[52] N. I. Paphitou. Antimicrobial resistance: Action to combat the rising microbial challenges. *International Journal of Antimicrobial Agents*, 42(SUPPL.1):S25, 2013.

[53] E. Kvam, B. Davis, F. Mondello, and A. L. Garner. Nonthermal atmospheric plasma rapidly disinfects multidrug-resistant microbes by inducing cell surface damage. *Antimicrobial Agents and Chemotherapy*, 56(4):2028, 2012.

[54] K. A. Dill, K. Ghosh, and J. D. Schmit. Physical limits of cells and proteomes. *Proceedings of the National Academy of Sciences of the United States of America*, 108(44):17876, 2011.

[55] S. Schneider, J.-W. Lackmann, F. Narberhaus, J. E. Bandow, B. Denis, and J. Benedikt. Separation of VUV/UV photons and reactive particles in the effluent of a He/O_2 atmospheric pressure plasma jet. *Journal of Physics D: Applied Physics*, 44(37):379501, 2011.

[56] S. Kelly, J. Golda, M. M. Turner, and V. Schulz-von der Gathen. Gas and heat dynamics of a micro-scaled atmospheric pressure plasma reference jet. *Journal of Physics D: Applied Physics*, 48(44):444002, 2015.

[57] N. Knake, S. Reuter, K. Niemi, V. Schulz-von der Gathen, and J. Winter. Absolute atomic oxygen density distributions in the effluent of a microscale atmospheric pressure plasma jet. *Journal of Physics D: Applied Physics*, 41(19):194006, 2008.

[58] D. Ellerweg, A. von Keudell, and J. Benedikt. Unexpected O and O_3 production in the effluent of He/O_2 microplasma jets emanating into ambient air. *Plasma Sources Science and Technology*, 21(3):034019, 2012.

[59] J. Benedikt, D. Schröder, S. Schneider, G. Willems, A. Pajdarová, J. Vlček, and V. Schulz-von der Gathen. Absolute OH and O radical densities in effluent of a He/H_2O micro-scaled atmospheric pressure plasma jet. *Plasma Sources Science and Technology*, 25(4):045013, 2016.

[60] J. Dedrick, et al. Controlled production of atomic oxygen and nitrogen in a pulsed radio-frequency atmospheric-pressure plasma. *Journal of Physics D: Applied Physics*, 50(45):1, 2017.

[61] A. T. West. *Optical and Electrical Diagnosis of Atmospheric Pressure Plasma Jets*. Ph.D. thesis, University of York, 2016.

[62] S. Große-Kreul, S. Hübner, S. Schneider, D. Ellerweg, A. von Keudell, S. Matejčík, and J. Benedikt. Mass spectrometry of atmospheric pressure plasmas. *Plasma Sources Science and Technology*, 24(4):044008, 2015.

[63] J. Benedikt, D. Ellerweg, and A. Von Keudell. Molecular beam sampling system with very high beam-to-background ratio: The rotating skimmer concept. *Review of Scientific Instruments*, 80(5), 2009.

[64] R. Ono. Optical diagnostics of reactive species in atmospheric-pressure nonthermal plasma. *Journal of Physics D: Applied Physics*, 49(8):83001, 2016.

[65] S. Reuter, J. S. Sousa, G. D. Stancu, and J.-P. Hubertus van Helden. Review on VUV to MIR absorption spectroscopy of atmospheric pressure plasma jets. *Plasma Sources Science and Technology*, 24(5):54001, 2015.

[66] J. S. Sousa, K. Niemi, L. J. Cox, Q. T. Algwari, T. Gans, and D. O'Connell. Cold atmospheric pressure plasma jets as sources of singlet delta oxygen for biomedical applications. *Journal of Applied Physics*, 109(12), 2011.

[67] J. Winter, et al. Tracking plasma generated H_2O_2 from gas into liquid phase and revealing its dominant impact on human skin cells. *Journal of Physics D: Applied Physics*, 47:285401, 2014.

[68] S. Reuter, J. Winter, S. Iseni, A. Schmidt-Bleker, M. Dunnbier, K. Masur, K. Wende, and K.-D. Weltmann. The Influence of Feed Gas Humidity Versus Ambient Humidity on Atmospheric Pressure Plasma Jet-Effluent Chemistry and Skin Cell Viability. *IEEE Transactions on Plasma Science*, 43(9):3185, 2015.

[69] T. Verreycken, R. Mensink, R. Van Der Horst, N. Sadeghi, P. J. Bruggeman, R. V. D. Horst, N. Sadeghi, and P. J. Bruggeman. Absolute OH density measurements in the effluent of a cold atmospheric-pressure Ar-H2O RF plasma jet in air. *Plasma Science and Technology*, 22(5):055014, 2013.

[70] K. Niemi, J. Waskoenig, N. Sadeghi, T. Gans, and D. O'Connell. The role of helium metastable states in radio-frequency driven helium–oxygen atmospheric pressure plasma jets: measurement and numerical simulation. *Plasma Sources Science and Technology*, 20(5):055005, 2011.

[71] S. Spiekermeier, D. Schröder, V. Schulz-von Der Gathen, M. Böke, and J. Winter. Helium metastable density evolution in a self-pulsing μ-APPJ. *Journal of Physics D: Applied Physics*, 48(3):035203, 2015.

[72] S. Schneider, M. Dünnbier, S. Hübner, S. Reuter, and J. Benedikt. Atomic nitrogen: a parameter study of a micro-scale atmospheric pressure plasma jet by means of molecular beam mass spectrometry. *Journal of Physics D: Applied Physics*, 47:505203, 2014.

[73] J. Benedikt, D. Ellerweg, S. Schneider, K. Rügner, R. R, H. Kersten, and T. Benter. Mass spectrometry of positive ions and neutral species in the effluent of an atmospheric pressure plasma with hexamethyldisiloxane and oxygen. *Journal of Physics D: Applied Physics*, 46(46):464017, 2013.

[74] C. Douat, S. Hübner, R. Engeln, and J. Benedikt. Production of nitric/nitrous oxide by an atmospheric pressure plasma jet. *Plasma Sources Science and Technology*, 25(2):025027, 2016.

[75] T. Verreycken and P. J. Bruggeman. OH Dynamics in a Nanosecond Pulsed Plasma Filament in Atmospheric Pressure He–H_2O upon the Addition of O_2. *Plasma Chemistry and Plasma Processing*, 34(3):605, 2014.

[76] A. F. Van Gessel, K. M. Alards, and P. J. Bruggeman. NO production in an RF plasma jet at atmospheric pressure. *Journal of Physics D: Applied Physics*, 46(26):265202, 2013.

[77] L. M. Martini, N. Gatti, G. Dilecce, M. Scotoni, and P. Tosi. Rate constants of quenching and vibrational relaxation in the OH(A2Σ+,v = 0,1), manifold with various colliders. *Journal of Physics D: Applied Physics*, 50(11):114003, 2017.

[78] A. Nikiforov, L. Li, N. Britun, R. Snyders, P. Vanraes, and C. Leys. Influence of air diffusion on the OH radicals and atomic O distribution in an atmospheric Ar (bio)plasma jet. *Plasma Sources Science and Technology*, 23(1):15015, 2014.

[79] S. Iseni, S. Zhang, A. F. H. van Gessel, S. Hofmann, B. T. J. van Ham, S. Reuter, K.-D. D. Weltmann, and P. J. Bruggeman. Nitric oxide density distributions in the effluent of an RF argon APPJ: effect of gas flow rate and substrate. *New Journal of Physics*, 16(12):123011, 2014.

[80] G. Dilecce, P. F. Ambrico, M. Simek, S. D. Benedictis, and S. De Benedictis. LIF diagnostics of hydroxyl radical in atmospheric pressure He-H_2O dielectric barrier discharges. *Chemical Physics*, 398(1):142, 2012.

[81] a. F. H. van Gessel, B. Hrycak, M. Jasiński, J. Mizeraczyk, J. J. a. M. van der Mullen, and P. J. Bruggeman. Temperature and NO density measurements by LIF and OES on an atmospheric pressure plasma jet. *Journal of Physics D: Applied Physics*, 46(9):095201, 2013.

[82] J. a. Thornton, P. J. Wooldridge, and R. C. Cohen. Atmospheric NO_2: in situ laser-induced fluorescence detection at parts per trillion mixing ratios. *Analytical chemistry*, 72(2):528, 2000.

[83] D. Venizelos and R. Sausa. Laser-induced fluorescence, mass spectrometric, and modeling studies of neat and NH3-doped H2/N2O/Ar flames. *Combustion and Flame*, 115(3):313, 1998.

[84] J. E. Goldsmith. Photochemical effects in two-photon-excited fluorescence detection of atomic oxygen in flames. *Applied optics*, 26(17):3566, 1987.

[85] U. Meier, J. Bittner, K. Kohse-Höinghaus, and T. Just. Discussion of two-photon laser-excited fluorescence as a method for quantitative detection of oxygen atoms in flames. *Symposium (International) on Combustion*, 22(1):1887, 1989.

[86] I. J. Wysong, J. B. Jeffries, and D. R. Crosley. Laser-induced fluorescence of $O(3p^{3P})$, O_2, and NO near 226 nm: photolytic interferences and simultaneous excitation in flames. *Optics Letters*, 14(15):767, 1989.

[87] K. C. Smyth and P. J. H. Tjossem. Radical concentration measurements in hydrocarbon diffusion flames. *Applied Physics B Photophysics and Laser Chemistry*, 50(6):499, 1990.

[88] K. C. Smyth and P. J. H. Tjossem. Relative H-atom and O-atom concentration measurements in a laminar, methane/air diffusion flame. *Symposium (International) on Combustion*, 23(1):1829, 1991.

[89] L. Gasnot, P. Desgroux, J. F. Pauwels, and L. R. Sochet. Improvement of two-photon laser induced fluorescence measurements of H- and O-atoms in premixed methane/air flames. *Applied Physics B*, 65(4-5):639, 1997.

[90] U. Meler, K. Kohse-Höinghaus, and T. Just. H and O atom detection for combustion applications: study of quenching and laser photolysis effects. *Chemical Physics Letters*, 126(6):567, 1986.

[91] A. W. Miziolek and M. A. Dewilde. Multiphoton photochemical and collisional effects during oxygen-atom flame detection. *Optics Letters*, 9(9):390, 1984.

[92] J. E. M. Goldsmith. Photochemical effects in 205-nm, two-photon-excited fluorescence detection of atomic hydrogen in flames. *Optics Letters*, 11(7):416, 1986.

[93] K. Niemi, V. S.-v. D. Gathen, H. F. Döbele, V. Schulz-Von Der Gathen, and H. F. Döbele. Absolute atomic oxygen density measurements by two-photon absorption laser-induced fluorescence spectroscopy in an RF-excited atmospheric pressure plasma jet. *Plasma Sources Science and Technology*, 14(2):375, 2005.

[94] W. K. Bischel, B. E. Perry, and D. R. Crosley. Two-photon laser-induced fluorescence in oxygen and nitrogen atoms. *Chemical Physics Letters*, 82(1):85, 1981.

[95] P. Das, G. S. Ondrey, N. van Veen, and R. Bersohn. Two photon laser induced fluorescence of carbon atoms. *The Journal of Chemical Physics*, 79(1983):724, 1983.

[96] D. A. Everest, C. R. Shaddix, and K. C. Smyth. Quantitative two-photon laser-induced fluorescence imaging of CO in flickering CH4/air diffusion flames. *Symposium (International) on Combustion*, 26(1):1161, 1996.

[97] K. Niki, M. Fujiwara, Y. Motoshima, T. Kawauchi, and K. Fukutani. Laser-induced fluorescence of hydrogen via the transition: Rotational-state-dependent collisional quenching. *Chemical Physics Letters*, 504(4-6):136, 2011.

[98] C. Brackmann, O. Hole, B. Zhou, Z. S. Li, and M. Aldén. Characterization of ammonia two-photon laser-induced fluorescence for gas-phase diagnostics. *Applied Physics B: Lasers and Optics*, 115(1):25, 2014.

[99] H. Neij and M. Aldén. Application of two-photon laser-induced fluorescence for visualization of water vapor in combustion environments. *Applied Optics*, 33(27):6514, 1994.

[100] E. Malmqvist, M. Jonsson, K. Larsson, M. Aldén, and J. Bood. Two-dimensional OH-thermometry in reacting flows using photofragmentation laser-induced florescence. *Combustion and Flame*, 169:297, 2016.

[101] O. Johansson, J. Bood, B. Li, A. Ehn, Z. S. Li, Z. W. Sun, M. Jonsson, A. A. Konnov, M. Ald??n, and M. Aldén. Photofragmentation laser-induced fluorescence imaging in premixed flames. *Combustion and Flame*, 158(10):1908, 2011.

[102] E. C. o. S. and Technology(COST). Action: biomedical applications of atmospheric pressure plasma technology BIOPLASMA MP1101.

[103] D. Marinov and N. S. J. Braithwaite. Power coupling and electrical characterization of a radio-frequency micro atmospheric pressure plasma jet. *Plasma Sources Science and Technology*, 23(6):062005, 2014.

[104] S. Schröter, A. R. Gibson, M. J. Kushner, T. Gans, D. O'Connell, and D. O. Connell. Numerical study of the influence of surface reaction probabilities on reactive species in an rf atmospheric pressure plasma containing humidity. *Plasma Physics and Controlled Fusion*, 60(1):014035, 2018.

[105] K. Niemi, D. O'Connell, N. De Oliveira, D. Joyeux, L. Nahon, J. P. Booth, and T. Gans. Absolute atomic oxygen and nitrogen densities in radio-frequency driven atmospheric pressure cold plasmas: Synchrotron vacuum ultra-violet high-resolution Fourier-transform absorption measurements. *Applied Physics Letters*, 103(3):034102, 2013.

[106] P. A. C. Beijer, A. Sobota, E. M. van Veldhuizen, and G. M. W. Kroesen. Multiplying probe for accurate power measurements on an RF Driven Atmospheric Pressure Plasma Jet applied to the COST Reference Microplasma Jet. *in Review Process*, 104001(10):104001, 2016.

[107] E. V. Johnson, S. Pouliquen, P. A. Delattre, and J. P. Booth. Tailored voltage waveform deposition of microcrystalline silicon thin films from hydrogen-diluted silane and silicon tetrafluoride: Optoelectronic properties of films. *Japanese Journal of Applied Physics*, 51(8 PART 2), 2012.

[108] J. Law and R. Rennie. *A Dictionary of Physics*. Oxford quick reference. Oxford University Press, 2009.

[109] M. Dünnbier, M. M. Becker, S. Iseni, R. Bansemer, D. Loffhagen, S. Reuter, and K. D. Weltmann. Stability and excitation dynamics of an argon micro-scaled atmospheric pressure plasma jet. *Plasma Sources Science and Technology*, 24(6), 2015.

[110] S. Hofmann, a. F. H. van Gessel, T. Verreycken, and P. Bruggeman. Power dissipation, gas temperatures and electron densities of cold atmospheric pressure helium and argon RF plasma jets. *Plasma Sources Science and Technology*, 20(6):065010, 2011.

[111] J. Held and F. Riedel. COST-power-monitor. *GitHub*, v0.1, 2017.

[112] F. Riedel. readoutthermalimages. *GitHub*, v0.1, 2019.

[113] P. Bruggeman, D. C. Schram, M. G. Kong, and C. Leys. Is the Rotational Temperature of OH() for Discharges in and in Contact with Liquids a Good Diagnostic for Determining the Gas Temperature? *Plasma Processes and Polymers*, 6(11):751, 2009.

[114] J. W. Birks, P. C. Andersen, C. J. Williford, A. A. Turnipseed, S. E. Strunk, C. A. Ennis, and E. Mattson. Folded tubular photometer for atmospheric measurements of NO2 and NO. *Atmospheric Measurement Techniques*, 11(5):2821, 2018.

[115] R. Atkinson, D. L. Baulch, R. A. Cox, J. N. Crowley, R. F. Hampson, R. G. Hynes, M. E. Jenkin, M. J. Rossi, and J. Troe. Evaluated kinetic and photochemical data for atmospheric chemistry: Volume I - gas phase reactions of O_x, HO_x, NO_x and SO_x species. *Atmospheric Chemistry and Physics*, 4(6):1461, 2004.

[116] S. P. Sander, et al. Chemical kinetics and photochemical data for use in Atmospheric Studies Evaluation Number 15. *Evaluation 15, JPL Publ. 06–2, Jet Propulsion Laboratory*, page 523, 2006.

[117] G. S. Tyndall, R. A. Cox, C. Granier, R. Lesclaux, G. K. Moortgat, M. J. Pilling, A. R. Ravishankara, and T. J. Wallington. Atmospheric chemistry of small organic peroxy radicals. *Journal of Geophysical Research Atmospheres*, 106(D11):12157, 2001.

[118] B. A. Thompson, P. Harteck, and R. R. Reeves. Ultraviolet absorption coefficients of CO_2 , CO, O_2 , H_2O, N_2O, NH_3, NO, SO_2 , and CH_4 between 1850 and 4000 A. *Journal of Geophysical Research*, 68(24):6431, 1963.

[119] P. Bruggeman, G. Cunge, and N. Sadeghi. Absolute OH density measurements by broadband UV absorption in diffuse atmospheric-pressure He–H_2O RF glow discharges. *Plasma Sources Science and Technology*, 21(3):035019, 2012.

[120] J. Birks. UV-Absorbing Interferences in Ozone Monitors. Technical report, 2B Technologies, Inc., 2015.

[121] S. Djurović and N. Konjević. On the use of non-hydrogenic spectral lines for low electron density and high pressure plasma diagnostics. *Plasma Sources Science and Technology*, 18(3):8, 2009.

[122] N. St Hill and G. Turner. Calibration of a Fourier transform infrared spectrometer for hydrogen peroxide vapour measurement. *Analytical Methods*, 3(8):1901, 2011.

[123] A. Schmidt-Bleker, J. Winter, S. Iseni, M. Dünnbier, K.-D. D. Weltmann, and S. Reuter. Reactive species output of a plasma jet with a shielding gas device - Combination of FTIR absorption spectroscopy and gas phase modelling. *Journal of Physics D: Applied Physics*, 47(14):145201, 2014.

[124] M. S. Moss, K. Yanallah, R. W. K. Allen, and F. Pontiga. An investigation of CO_2 splitting using nanosecond pulsed corona discharge: effect of argon addition on CO_2 conversion and energy efficiency. *Plasma Sources Science and Technology*, 26(3):035009, 2017.

[125] F. J. Harris. On the Use of Windows with the Discrete Fourier Transform. *Proceedings of the IEEE*, 66(1):51, 1978.

[126] R. Kochanov, I. Gordon, L. Rothman, P. Wcisło, C. Hill, and J. Wilzewski. HITRAN Application Programming Interface (HAPI): A comprehensive approach to working with spectroscopic data. *Journal of Quantitative Spectroscopy and Radiative Transfer*, 177:15, 2016.

[127] C. H. R. V. K. Y. T. P. F. B. M. B. V. B. A. C. K. V. C. B. J. D. J.-M. F. R. R. G. J. T. H. D. J. V. I. P. A. P. K. P. S. M.-A. S. J. T. G. C. T. H. T. V. G. T. A. B. A. G. C. V. M. D. T. F. I.E. Gordon L.S. Rothman, et al. The HITRAN2016 Molecular Spectroscopic Database. *Journal of Quantitative Spectroscopy and Radiative Transfer*, 203:3, 2017.

[128] E. Es-sebbar, Y. Benilan, A. Jolly, and M.-C. Gazeau. Characterization of an N_2 flowing microwave post-discharge by OES spectroscopy and determination of absolute

ground-state nitrogen atom densities by TALIF. *Journal of Physics D: Applied Physics*, 42(13):135206, 2009.

[129] E. Es-sebbar, M. C-Gazeau, Y. Benilan, A. Jolly, and C. D. Pintassilgo. Absolute ground-state nitrogen atom density in a N_2/CH_4 late afterglow: TALIF experiments and modelling studies. *Journal of Physics D: Applied Physics*, 43(33):335203, 2010.

[130] W. D. Kulatilaka, J. H. Frank, and T. B. Settersten. Interference-free two-photon LIF imaging of atomic hydrogen in flames using picosecond excitation. *Proceedings of the Combustion Institute*, 32(1):955, 2009.

[131] H. F. Döbele, T. Mosbach, K. Niemi, and V. S.-v. D. Gathen. Laser-induced fluorescence measurements of absolute atomic densities: concepts and limitations. *Plasma Sources Science and Technology*, 14(2):S31, 2005.

[132] K. Niemi, V. S.-v. der Gathen, H. F. Döbele, V. Schulz-von der Gathen, and H. F. Döbele. Absolute calibration of atomic density measurements by laser-induced fluorescence spectroscopy with two-photon excitation. *Journal of Physics D: Applied Physics*, 34(15):2330, 2001.

[133] K. D. Bonin and T. J. McIlrath. Two-photon electric-dipole selection rules. *J. Opt. Soc. Am. B*, 1(1):52, 1984.

[134] F. Riedel. picolabreadouphotodiode. *GitHub*, v0.2, 2019.

[135] L. R. Williams and D. R. Crosley. Collisional vibrational energy transfer of OH (A2S+, v'=1). *Journal of Chemical Physics*, 104(17):6507, 1996.

[136] M. Baasandorj, D. K. Papanastasiou, R. K. Talukdar, A. S. Hasson, and J. B. Burkholder. $(CH_3)_3COOH$ (*tert*-butyl hydroperoxide): OH reaction rate coefficients between 206 and 375 K and the OH photolysis quantum yield at 248 nm. *Physical Chemistry Chemical Physics*, 12(38):12101, 2010.

[137] J. Waskoenig, K. Niemi, N. Knake, L. M. Graham, S. Reuter, V. Schulz-von der Gathen, and T. Gans. Diagnostic-based modeling on a micro-scale atmospheric-pressure plasma jet. *Pure and Applied Chemistry*, 82(6):1209, 2010.

[138] D. Ellerweg, J. Benedikt, A. Von Keudell, N. Knake, and V. Schulz-Von Der Gathen. Characterization of the effluent of a He/O_2 microscale atmospheric pressure plasma jet by quantitative molecular beam mass spectrometry. *New Journal of Physics*, 12(1):013021, 2010.

[139] G. Willems, J. Benedikt, and A. Von Keudell. Absolutely calibrated mass spectrometry measurement of reactive and stable plasma chemistry products in the effluent of a

He/H_2O atmospheric plasma. *Journal of Physics D: Applied Physics*, 50(33):335204, 2017.

[140] S. Z. He, Z. M. Chen, X. Zhang, Y. Zhao, D. M. Huang, J. N. Zhao, T. Zhu, M. Hu, and L. M. Zeng. Measurement of atmospheric hydrogen peroxide and organic peroxides in Beijing before and during the 2008 Olympic Games: Chemical and physical factors influencing their concentrations. *Journal of Geophysical Research Atmospheres*, 115(17):D17307, 2010.

[141] S. Schroeter. *Reactive oxygen and hydrogen species generation in radio-frequency atmospheric pressure plasmas - Experimental and numerical investigations*. Ph.D. thesis, The University of York, 2017.

[142] M. M. Turner. Uncertainty and error in complex plasma chemistry models. *Plasma Sources Science and Technology*, 24(3):035027, 2015.

[143] R. Ono, Y. Teramoto, and T. Oda. Measurement of atomic nitrogen in N2 pulsed positive corona discharge using two-photon absorption laser-induced fluorescence. *Japanese Journal of Applied Physics*, 48(12):122302, 2009.

[144] G. P. Smith and D. R. Crosley. A photochemical model of ozone interference effects in laser detection of tropospheric OH. *Journal of Geophysical Research*, 95(D10):16427, 1990.

[145] E. J. Dunlea and A. R. Ravishankara. Measurement of the rate coefficient for the reaction of O(1D) with H_2O and re-evaluation of the atmospheric OH production rate. *Physical Chemistry Chemical Physics*, 6(13):3333, 2004.

[146] M. A. Malik, A. Ghaffar, and S. A. Malik. Water purification by electrical discharges. *Plasma Sources Science and Technology*, 10(1):82, 2001.

[147] M. A. Khadre, A. E. Yousef, and J. G. Kim. Microbiological aspects of ozone applications in food: A review. *Journal of Food Science*, 66(9):1242, 2001.

[148] H. Bahre, M. Aragunde, J. Golda, and V. S.-v. D. Gathen. Ozone formation and destruction mechanisms in an atmospheric pressure plasma jet. In *30th ICPIG*. Belfast, UK, 2011.

[149] B. T. J. Van Ham, S. Hofmann, R. Brandenburg, and P. J. Bruggeman. In situ absolute air, O_3 and NO densities in the effluent of a cold RF argon atmospheric pressure plasma jet obtained by molecular beam mass spectrometry. *Journal of Physics D: Applied Physics*, 47(22):224013, 2014.

[150] A. DeMore, WB and Molina, Mario J and Watson, RT and Golden, DM and Hampson, Robert F and Kurylo, Michael J and Howard, Charleton J and Ravishankara. Chemical kinetics and photochemical data for use in stratospheric modeling. Evaluation number 6. Technical report, NASA, 1983.

[151] S. A. Montzka, M. Krol, E. Dlugokencky, B. Hall, P. Jöckel, and J. Lelieveld. Small interannual variability of global atmospheric hydroxyl. *Science*, 331(6013):67, 2011.

[152] V. Sinha, J. Williams, J. N. Crowley, and J. Lelieveld. The comparative reactivity method - A new tool to measure total OH Reactivity in ambient air. *Atmospheric Chemistry and Physics*, 8(8):2213, 2008.

[153] M. Boselli, V. Colombo, M. Gherardi, R. Laurita, A. Liguori, P. Sanibondi, E. Simoncelli, and A. Stancampiano. Characterization of a Cold Atmospheric Pressure Plasma Jet Device Driven by Nanosecond Voltage Pulses. *IEEE Transactions on Plasma Science*, 43(3):713, 2015.

[154] E. Robert, V. Sarron, T. Darny, D. Riès, S. Dozias, J. Fontane, L. Joly, and J. M. Pouvesle. Rare gas flow structuration in plasma jet experiments. *Plasma Sources Science and Technology*, 23(1), 2014.

[155] A. V. Ivanov, S. Trakhtenberg, A. K. Bertram, Y. M. Gershenzon, and M. J. Molina. OH, HO 2 , and Ozone Gaseous Diffusion Coefficients. *The Journal of Physical Chemistry A*, 111(9):1632, 2007.

[156] M. J. Tang, R. A. Cox, and M. Kalberer. Compilation and evaluation of gas phase diffusion coefficients of reactive trace gases in the atmosphere: volume 1. Inorganic compounds. *Atmospheric Chemistry and Physics*, 14(17):9233, 2014.

[157] E. L. Cussler. *Diffusion: mass transfer in fluid systems*. Cambridge University Press, 2017.

[158] S. Yonemori, Y. Nakagawa, R. Ono, and T. Oda. Measurement of OH density and air–helium mixture ratio in an atmospheric-pressure helium plasma jet. *Journal of Physics D: Applied Physics*, 45(22):225202, 2012.

[159] M. Tamura, P. A. Berg, J. E. Harrington, J. Luque, J. B. Jeffries, G. P. Smith, and D. R. Crosley. Collisional quenching of CH(A), OH(A), and NO(A) in low pressure hydrocarbon flames. *Combustion and Flame*, 114(3-4):502, 1998.

[160] I. J. Wysong, J. B. Jeffries, and D. R. Crosley. Quenching of a $2\Sigma+$ OH at 300 K by several colliders. *The Journal of Chemical Physics*, 92(9):5218, 1990.

[161] J. Thiebaud, A. Aluculesei, and C. Fittschen. Formation of HO_2 radicals from the photodissociation of H_2O_2 at 248 nm. *Journal of Chemical Physics*, 126(18):186101, 2007.

[162] K.-D. Weltmann, E. Kindel, R. Brandenburg, C. Meyer, R. Bussiahn, C. Wilke, and T. von Woedtke. Atmospheric Pressure Plasma Jet for Medical Therapy: Plasma Parameters and Risk Estimation. *Contributions to Plasma Physics*, 49(9):631, 2009.

[163] S. Reuter, J. Winter, A. Schmidt-Bleker, H. Tresp, M. U. Hammer, and K. D. Weltmann. Controlling the ambient air affected reactive species composition in the effluent of an argon plasma jet. *IEEE Transactions on Plasma Science*, 40(11 PART1):2788, 2012.

[164] A. Schmidt-Bleker, S. Reuter, and K.-D. D. Weltmann. Non-dispersive path mapping approximation for the analysis of ambient species diffusion in laminar jets. *Physics of Fluids*, 26(8):083603, 2014.

[165] A. Schmidt-Bleker, J. Winter, A. Bösel, S. Reuter, and K.-D. D. Weltmann. On the plasma chemistry of a cold atmospheric argon plasma jet with shielding gas device. *Plasma Sources Science and Technology*, 25(1):015005, 2015.

[166] S. Iseni, J. Winter, K. Weltmann, and S. Reuter. Gas flow and discharge propagation interaction of a non-thermal , non- equilibrium RF argon atmospheric pressure plasma jet investigated by planar laser induced fluorescence Gas flow and discharge propagation interaction of a non-thermal , non-equilibrium. In *ESCAMPIG XXII*. Greifswald, GER, 2015.

[167] M. Gianella, S. Reuter, S. A. Press, A. Schmidt-Bleker, J.-P. H. van Helden, G. A. Ritchie, J. H. Helden, and G. A. Ritchie. HO_2 reaction kinetics in an atmospheric pressure plasma jet determined by cavity ring-down spectroscopy. *Plasma Sources Science and Technology*, 27(9):095013, 2018.

[168] J. H. Frank and T. B. Settersten. Two-photon LIF imaging of atomic oxygen in flames with picosecond excitation. *Proceedings of the Combustion Institute*, 30(1):1527, 2005.

[169] S. Zhang, A. F. Van Gessel, S. C. Van Grootel, and P. J. Bruggeman. The effect of collisional quenching of the O 3p ^3P_J state on the determination of the spatial distribution of the atomic oxygen density in an APPJ operating in ambient air by TALIF. *Plasma Sources Science and Technology*, 23(2), 2014.

[170] M. S. Mann, R. Tiede, K. Gavenis, G. Daeschlein, R. Bussiahn, K.-D. D. Weltmann, S. Emmert, T. von Woedtke, and R. Ahmed. Introduction to DIN-specification 91315

based on the characterization of the plasma jet kINPen® MED. *Clinical Plasma Medicine*, 4(2):35, 2016.

[171] J. Golda, F. Kogelheide, P. Awakowicz, and V. S.-v. der Gathen. Dissipated electrical power and electron density in an RF atmospheric pressure helium plasma jet. *Plasma Sources Science and Technology*, 28(9):095023, 2019.